3D POROUS HIGH AREAL CAPACITY LITHIUM-ION MICRO-BATTERIES

Chenpeng Huang

A DISSERTATION

in

Chemical and Biomolecular Engineering

Presented to the Faculties of the University of Pennsylvania

in

Partial Fulfillment of the Requirements for the

Degree of Doctor of Philosophy

2020

Supervisor of Dissertation:

Sue Ann Bidstrup Allen, PhD.
Professor of Chemical and Biomolecular Engineering

Co-Supervisor of Dissertation:

Mark G. Allen, PhD.
Alfred Fitler Moore Professor of Electrical and Systems Engineering

Graduate Group Chairperson:

John C. Crocker, PhD.
Professor of Chemical and Biomolecular Engineering

Dissertation Committee:

Eric Detsi, PhD., Stephenson Term Assistant Professor of Materials Science and Engineering
Daeyeon Lee, PhD., Professor of Chemical and Biomolecular Engineering
James Pikul, PhD., Assistant Professor of Mechanical Engineering and Applied Mechanics
John M. Vohs, PhD., Carl V.S. Patterson Professor of Chemical and Biomolecular Engineering

ABSTRACT

3D POROUS HIGH AREAL CAPACITY LITHIUM-ION MICRO-BATTERIES

Chenpeng Huang
Sue Ann Bidstrup Allen
Mark Allen

The reduction in size and the improvement in the capability of microsystems are presently limited by the size and the capacity of their on-board power supplies. A key performance metrics for the power supplies of microsystems is the capacity per footprint area, or areal capacity, in mAh/cm^2, while the commercial 2D thin film micro-batteries possess low areal capacity of less than 0.2 mAh/cm^2. Thus, it's necessary to load battery components onto scalable 3D architectures to enable electrodes with high areal capacity. In this work, novel fabrication techniques are proposed. A facile high current hydrogen-templated electroplating technique is utilized to generate 3D porous microstructures, which serve as the scaffolds, current collectors, or even active materials for battery electrodes. In addition, electrochemical techniques and laser-machined substrate ensure uniform coating and high utilization of battery active materials to allow superior electrochemical performance. On the half-cell level, Si/NiSn composite anode deliver ultrahigh areal capacity over 40 mAh/cm^2; and carbonate-compatible S cathode is developed and possess 4mAh/cm^2 areal capacity with 85% capacity retention after 50 cycles at a high current density of 2.5 mA/cm^2. On the full cell level, the micro-battery delivers an areal capacity of 3 mAh/cm^2 with 2.3 mW/cm^2 power density that meets the demands of many micro-electronic device. In addition, a proof-of-concept monolithic full cell based on polymer electrodeposition

techniques is demonstrated to accelerate the cell manufacturing process. In conclusion, in this study, microelectronics-compatible fabrication of scalable, high surface area, and porous 3D metal network-based Li-ion micro-batteries is devised to enable electrodes with high areal capacity, high power density, manufacturability, low cost, and good safety performance.

TABLE OF CONTENTS

LIST OF FIGURES

LIST OF TABLES

CHAPTER 1: INTRODUCTION

1.1. Background and Motivation

In recent years, there has been continuous development of microscale electronics, such as micro-electromechanical systems, microrobots, implantable medical sensors, radio-frequency identification tags, remote environmental sensors, portable and wearable electronics, and their wireless self-powered micro/nanosystems [1]. Directions towards multifunctionality, high integration and high power drive these micro-electronic devices towards miniaturization [2]. However, the power sources used to supply energy to these devices, which require an unmatchable combination of high energy and power density [3], have not kept pace with the advance of microelectronics and the emergence of microelectromechanical systems (MEMS) [4]. Since conventional forms of batteries such as commercial coin cells are still routinely used in these applications due to the lack of commercial cells of smaller sizes, the reduction in volume and the improvement in the capability of microsystems are presently limited by the size, capacity and power of their on-board power supplies [5], as seen in Table 1.1. Even the smallest coin cell (ML421) is about 5 mm in diameter [5]. Thus, the continued demand for miniaturized energy storage devices with sufficient energy and power densities is projected, as evidenced by the increasing number of devices requiring miniaturized energy storage devices (See Figure 1.1 [6]).

Application	System volume (mm^3)	Battery volume (mm^3)
Micro-Air vehicle	3.0	110
Environmental/ biological sensing	150	350
Biological monitoring	0.0073	326
Microelectronic pill	0.5	1200

Table 1. 1: Survey of battery-powered microelectromechanical systems [4]

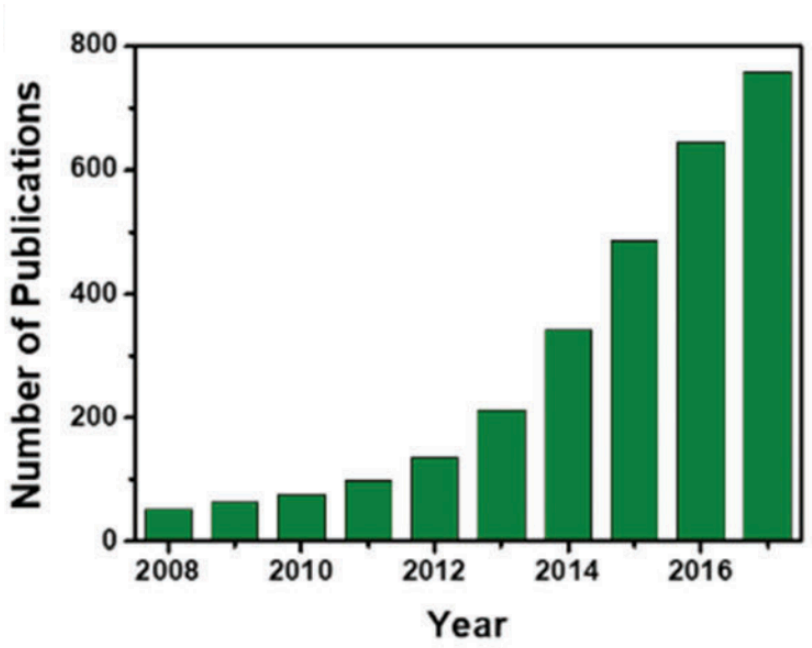

Figure 1. 1: Number of publications related miniaturized energy storage devices vs. year [6]

Currently, micro-batteries and micro-supercapacitors are two representative microscale electrochemical energy storage devices, which can be manufactured on the micro/nanoscale to be directly coupled with microelectronics as stand-alone microscale power sources or as complements to miniaturized energy harvesters [1]. The size of these devices is usually on the millimeter or centimeter scale, with a micron-scale distance

between the two electrodes [6]. The total volume of the device may range up to 0.1cm^3 [7]. Notably, most microelectronics normally can operate with low power, ranging from nanowatts to milliwatts (See Figure 1.2 (a)), while high specific energy (per area or volume) of the corresponding power sources is prioritized for operation for extended periods of time [8-10] without replacement [1]. Thus, as shown in Figure 1.2 (b), micro-batteries have an obvious advantage compared with micro-supercapacitors.

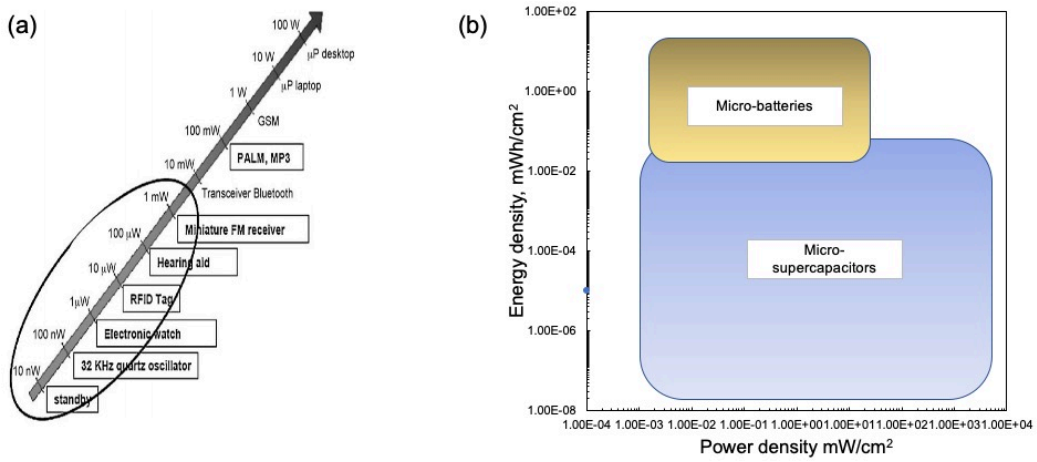

Figure 1. 2: (a): Typical electrical consumption for different mobile devices [11]. (b): Area normalized Ragone plot of energy and power density showing the estimated performance of micro-batteries and micro-supercapacitors [12]

Compared with lead-acid and Ni-MH chemistry, Li-ion batteries possess higher energy density, power density (as shown in Figure 1.3 below), and better cycle life, and thus make up majority of the commercial battery market. Thus, they are considered the primary choice of chemistry for micro-batteries.

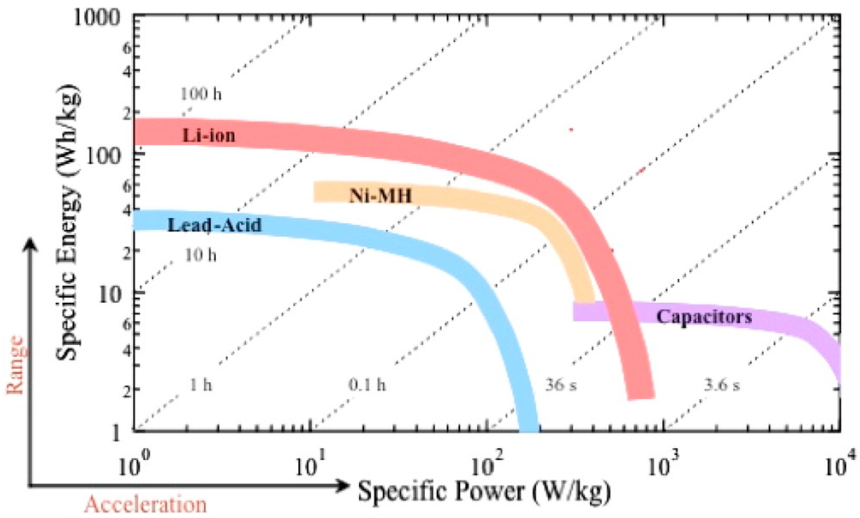

Figure 1. 3: Ragone plot showing energy and power density of different battery and capacitor chemistries [13]

To bridge the gap due to lack of a suitable miniaturized power source, scientists at Pacific Northwest National Laboratory (PNNL) developed micro-sized lithium primary batteries with high energy density for a Juvenile salmon acoustic telemetry system (JSATS) [14]. Panasonic commercialized industry's smallest pin-type batteries with a similar design in 2014 for targeted applications in wearable devices, electronic pens and medical devices [15]. However, these batteries are primary-type, meaning they are not rechargeable. Considering the complexity of replacing batteries for micro-electronic devices, it would be desirable to use rechargeable, or secondary, Li-ion based batteries with good cycle life as power sources to eliminate the need for replacement services. In addition, the long-term goal of micro-battery research will be defined by the demands of the fast growth of microelectromechanical systems (MEMS) technology for even higher power and higher energy on a smaller scale [16].

In conventional rechargeable Li-ion battery (LIB) electrodes (See Figure 1.4 (a)), both the cathode and anode consist of composites of conductive carbon and polymer binder composite slurry pasted on Al and Cu foils respectively. Typically, transition metal oxides such as $LiCoO_2$, LiFePO4, and $LiNi_xCo_yMn_zO_2$ (x + y + z = 1) are used as the cathode active materials, and graphite or graphite silicon composites are used as the anode materials. The cathode and the anode are separated by a layer of polymer soaked with organic liquid electrolyte (See Figure 1.3 (b)). As the size of the battery shrinks, the fabrication process for composite electrodes and the use of liquid electrolyte becomes increasingly incompatible with the required microfabrication process [5]. As a result, micro-batteries should differ greatly from bulk-size LIBs in their architecture design and material choices [5].

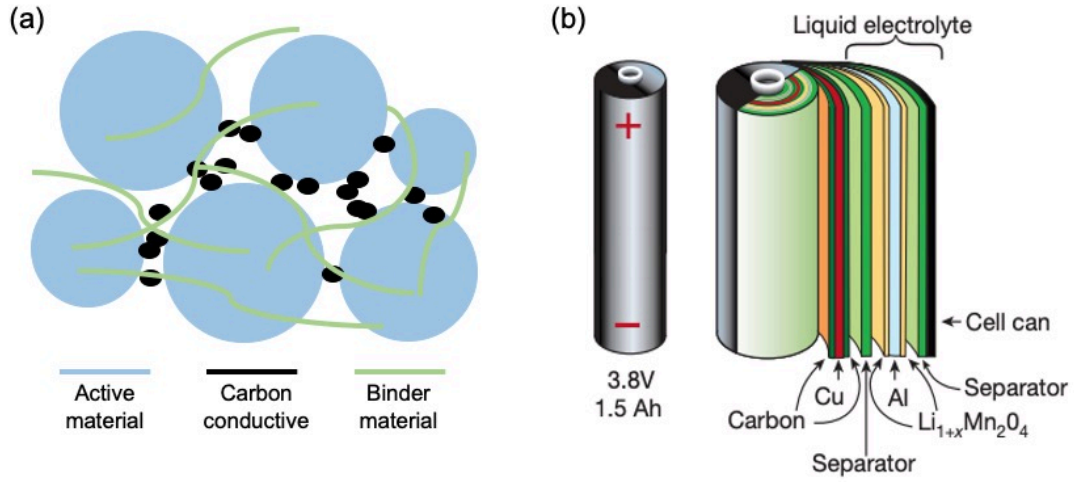

Figure 1. 4**:** (a) a LIB composite electrode (b) Components and assembly of conventional 18650 cylindrical Li-ion battery [3]

Commercially, thin-film batteries adopting two-dimensional (2D) planar design are

commonly used for micro-applications [5]. A thin film battery is similar to a conventional Li-ion battery in its individual components (See Figure 1.5 below), except that the cathode and anode are made of a pure thin film of active material, and a ceramic film is used as the solid electrolyte layer. Electronic and ionic conduction within the electrodes are entirely dependent upon the intrinsic properties of electrode materials. As a result, the thicknesses of the electrodes are limited to a few microns to avoid loss of power and poor electrode utilization [5]. For the electrolyte layer, solid-state inorganic glassy or crystalline materials are typically used because of the dimensional stability and design flexibility [5].

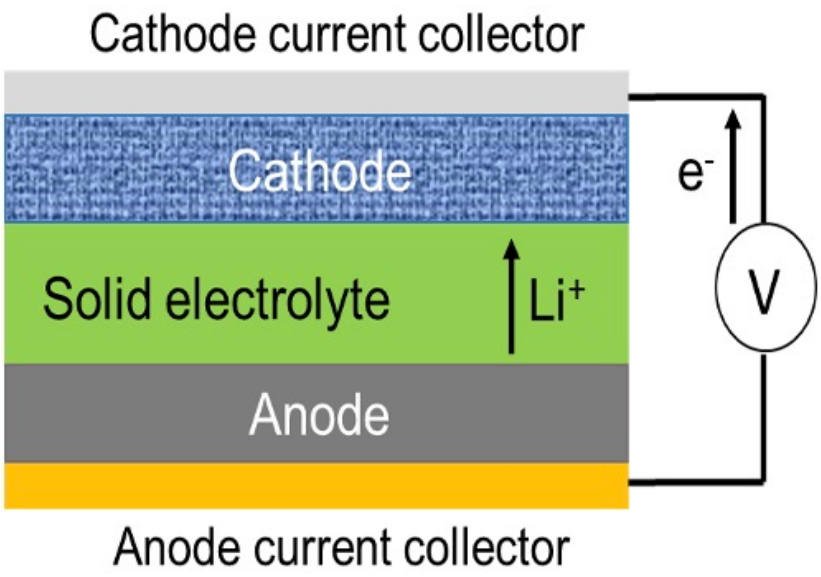

Figure 1. 5**:** Schematic of a thin film Li-ion micro-battery

Due to the stability of the solid-state electrolyte and uniform current distribution across the electrode/electrolyte, thin-film batteries exhibit much better rechargeability than liquid-electrolyte-based lithium-ion batteries [17]. The all-solid-state design is also compatible with the fabrication processes for many devices with which the thin-film batteries are

integrated, such as integrated circuits and solar panels [5]. These favorable traits have led to the successful commercialization of thin-film batteries with targeted application including radio-frequency identification (RFIDs), medical patches, smartcards, and wireless sensors [5]. However, despite the many advantages and commercial success of thin film batteries, their low areal capacity and power prevent them from meeting the increasing energy and power needs of the fast-growing electronic sectors, especially to meet the demands of MEMS applications [5].

A key parameter in the field of micro-electronics and MEMS is the available footprint area, due to compactness of various components on the chip [4]. Thus, in order to evaluate the performance of the power source, the metric of areal capacity and power, in terms of mAh/cm^2, J/cm^2, and mW/cm^2 etc., is more relevant compared to traditional measures such as volumetric energy and power densities. Long et al. have estimated that smart dust has an energy demand of about 30 mWh/cm^2 [18]. Thin-film batteries have a very limited areal energy density of 0.3 mWh/cm^2 [5]. Simply by making the active material films thicker does not solve the problem since this will compromise the power performance. In addition, thick films tend to crack during cycling due to continuous film expansion/contraction [4]. Limited active surface area, high internal resistance due to solid/solid interfaces, and low conductivities of electrolytes determine that thin-film micro-batteries are at best a medium-power system, which would require additional space to possess meaningful capacities and sacrifice performance of the electronic device [5]. Currently, there exists no commercial micro-batteries that combine both small size and high areal energy density [5].

Further enhancement of micro-battery performance requires 3D design of battery components, which exploits the out-of-plane dimension to enlarge the surface area per footprint area and increases amount of active material deposited [5]. As illustrated by Figure 1.6 below [19], for a thick 2D film electrode, only a portion of the active material is used for energy (charge) storage because of the slow Li ion diffusion and electron conduction. By contrast, a 3D electrode architecture contains a conductive scaffold acting as a current collector and a porous network for efficient ion transport [19]. Locally, 3D batteries have a similar geometry as thin-film batteries, i.e., thin layers of cathode, electrolyte, anode and current collectors, ensuring a short diffusion length for Li-ions [5]. This is desirable for more utilization of the electrode materials regardless of the overall structure thickness and for the realization of high rate and high-capacity energy storage [19]. Thus, the task of 3D design is to fold the high active surface area, layered 3D structure onto a 2D footprint while maintaining the short ionic and electronic current paths [5].

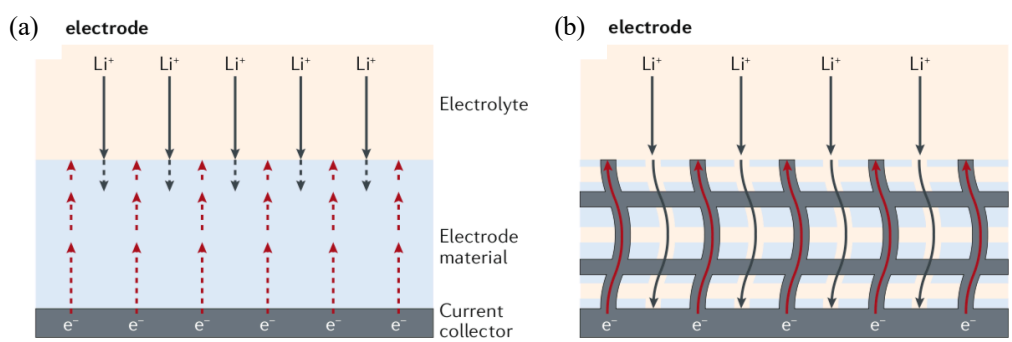

Figure 1. 6**:** Comparison of ion transport path between (a) 2D and (b) 3D electrode [19]

1.2. Design of 3D electrodes

The majority of current research efforts are dedicated to battery materials while the battery configurational design is relatively overlooked [20]. More research is required in the development of innovative fabrication procedures and novel architectures of the electrode for micro-batteries [5]. In order to achieve superior performance, there are a few general design guidelines:

1. High porosity and low tortuosity: High utilization and power capability of battery electrodes can be realized through facile reaction kinetics and effective Li-ion transport. Electrochemical reactions primarily occur at the interface between the electrodes and the electrolyte. In order to accelerate the reaction kinetics, which increases the power density, the electrodes must possess large surface area-to-volume ratios [21]. Having a 3D porous electrode would enable increased effective contact area between electrode and electrolyte, which decreases the overall charge transfer resistance and improves the electrochemical reaction kinetics. Architected porous electrodes can also enable improvements in both power and energy by increasing the transport of reactants and products to and from the reaction sites [21]. Conventional Li-ion battery electrodes are generally not thicker than 100 μm due to the limitations of Li-ion transport through a tortuous pore structure in the liquid phase of close-packing composite electrodes [21]. A further increase in electrode thickness significantly impedes the infiltration of electrolyte and considerably increases the ion transfer distance, as shown in Figure 1.7 (a) below [20]. According to the effective diffusion coefficient D_{eff} expression, defined as D_{eff} =

$\frac{\epsilon}{\tau}D$ (where ϵ is the porosity, τ is the tortuosity, and D is the intrinsic liquid state diffusion coefficient), D_{eff} scales linearly with the electrode porosity and is inversely proportional to the tortuosity of the electrode. Thus, it is important to design a 3D architected electrode with sufficient porosity and low tortuosity to facilitate ion transport through the pores and achieve good power density. In addition, void volumes in the porous electrodes can effectively mitigate the volume issues associated with conversion type battery materials [22], such as sulfur cathode and silicon anode. The deployment of these materials, combined with a porous electrode architecture, can help realize micro-batteries with both high energy density and long cycle life.

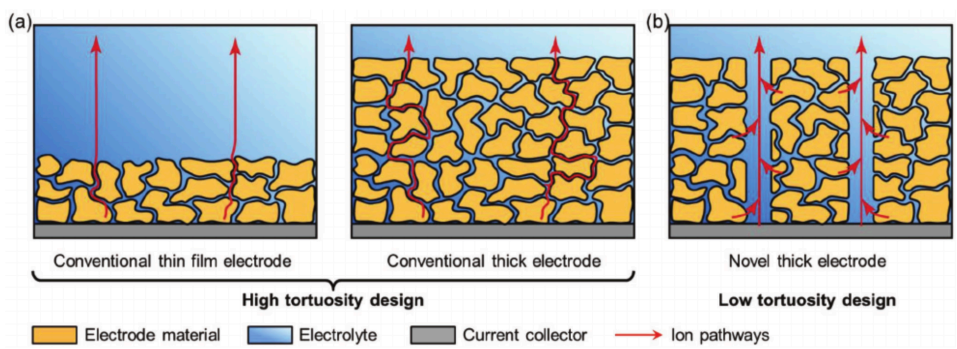

Figure 1. 7**:** Schematics illustrating the ion transfer pathways in diverse electrodes (a) Conventional thin film electrode and thick electrode having high tortuosity and elongated ion diffusion pathway (b) Novel thick electrode with low tortuosity design which facilitates ion transport [20]

2. Scalability: 2D thin film electrodes are limited by low area-to-volume ratio, resulting in low areal capacity. Increases in 2D thin film electrode thickness in order to obtain higher capacity would result in longer diffusion length of Li ions and sacrifice power density. Areal constraints on microelectronics have

transitioned research toward 3D architected materials that could be made thick in the out-of-plane direction [21], while maintaining thin films of active material to be deposited locally. Thus, it is essential for the fabrication method to be scalable to mm scale to increase areal energy sufficient for microelectronics applications and simultaneously maintain good kinetics.

3. Integrated current collector: The current collector is a major component in the electrode. It establishes connection between internal and external circuit, anchors electrode materials, and ensures rapid and stable electron transfer [20]. In a planar electrode, the active layer is generally laminated on a metallic foil current collector. However, for thick electrodes, the high expansion/contraction stress during electrode cycling may cause active layers to delaminate if initial adhesion to the current collector is not strong. In addition, electrode materials, especially cathodes, generally have insufficient electrical conductivity, which may limit performance of thick electrode designs. Having an integrated current collector network can significantly increase the mechanical stability of the electrode, enlarge the contact area between current collector and the active materials, and provide electron conduction backbones throughout the entire electrode [20].

A few common strategies have been proposed to create various designs of 3D electrodes, such as template synthesis [23], formation of high aspect ratio micro-channels [24], and self-assembly of nanoparticles [25]. More details regarding specific works will be discussed in Section 1.4.

1.3. Use of solid electrolyte for 3D micro-batteries:

Due to the relative low energy density and safety concerns from flammable electrolytes, conventional Li-ion batteries have reached a bottleneck period of development [26]. As a result, solid state batteries, i.e. replacing organic liquid electrolyte-soaked separators with (quasi-)solid state Li-ion conductors, were explored as promising candidates, and significant advances have been made in the past few years [26]. Although currently there are still issues with performance and mechanistic understanding of solid electrolytes, they have the potential to outperform liquid electrolytes after optimizations in terms of thermal, chemical, electrochemical, and mechanical stability, while possessing similar ionic conductivities, as illustrated in Figure 1.8 [26]. As a result of the inherent dimensional stability and safer nature of solid electrolyte materials compared to liquid counterparts, fewer safety and packaging measures are required during fabrication and assembly of micro-batteries, thus increasing their energy density.

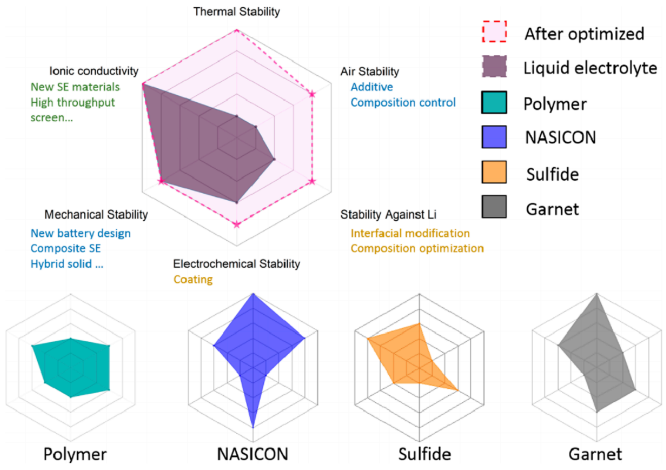

Figure 1. 8**:** Radar maps of the stability issues of different types of electrolytes [26]

Although solid electrolytes typically have much lower ionic conductivities than liquid

electrolytes, large internal resistance can be avoided by fabricating a very thin electrolyte layer (i.e. a few microns) for micro-batteries. In general, solid electrolytes can be categorized into inorganic ceramic electrolytes and polymer electrolytes. Several inorganic lithium ion conductors of a wide range of chemical compositions and crystal structures such as Li_4SiO_4 derivatives, sodium super ionic conductors (NASICON), lithium super ionic conductors (LISICON), perovskite type $Li_{0.35}La_{0.55}TiO_3$ (LLTO), lithium phosphorus oxynitride (LiPON), have been under investigation [5]. LIPON developed by Oak Ridge National Laboratory delivered the best overall performance [17]. The low ionic conductivity of LIPON can be mitigated by its thickness as thin as several microns. More importantly, LiPON has excellent electrochemical stabilities ensuring its reliable operation with metallic lithium, even at elevated temperatures [5].

Polymer electrolytes can be sub-categorized into solid polymer electrolytes and gel polymer electrolytes. There is no liquid component in solid polymer electrolyte. Li-ion transport is coupled with segmental motion of polymer chains, transferring Li-ions from one coordination site to another. For gel polymer electrolytes, polymers are added to a liquid electrolyte to enhance mechanical strength, while the ion transport can occur in either liquid or solid phase [26]. Conventionally, polymer electrolytes are fabricated through solution-casting process. However, it is difficult to utilize this method to coat a 3D structure conformally. Recently, novel techniques have been developed to deposit polymer electrolytes onto 3D structures, such as electrodeposition of nanometer thick polymer films [27-29]. Similar to inorganic electrolytes, an immediate benefit of using

ultrathin solid polymer electrolytes is that polymers with even modest lithium-ion conductivity provide minimal resistance when only tens of nanometers thick [27].

Compared with inorganic solid-state electrolytes, polymer electrolytes demonstrate sufficient interface contact, good electrochemical stability, easy fabrication, and economic availability [26]. In addition, due to lack of available instrumentation to fabricate inorganic solid electrolytes in 3D (e.g. atomic layer deposition (ALD), chemical vapor deposition (CVD)), in the current study we chose to use polymer electrolytes for our 3D micro-battery fabrication, which could be deposited via more accessible routes, as will be illustrated in Chapter 4.

1.4. Review of prior arts

In this section, techniques that are used to fabricate novel, high performance, 3D Li-ion micro-batteries these structures are presented. Performance and limitations of the resulting electrodes will be discussed, as summarized in Table 1.2. Electrode designs are categorized according to whether a liquid or solid electrolyte (including gel electrolyte) is utilized. Note that although this study mainly focuses on solid electrolyte (or gel electrolyte) based systems, previous efforts on liquid state systems may still offer valuable insights.

Cathode/anode	Electrolyte	Potential range, V	Areal capacity, mAh/cm²	Power density, mW/cm²	Cycle life	Reference
PPYDBS/C	1M $LiClO_4$ in 1:1 EC/DMC	0.7 – 3.5	0.01	0.06	12	[24]
Li_xMnO_2/NiSn	1M $LiClO_4$ in 1:1 EC/DMC	2 - 4	0.005	185	15	[30]
$LiFePO_4/Li_4Ti_5O_{12}$	1M $LiClO_4$ in 1:1 EC/DMC	1.5 - 2	1.5	2.7	30	[25]
$LiFePO_4/Li_4Ti_5O_{12}$	1M LiTFSI in PC	1 - 2.5	4.45	0.24	25	[31]
$Li_xMoO_yS_z$/Graphite	PVDF-based hybrid polymer electrolyte with 1M $LiPF_6$ in 1:1 EC/DEC	1.3 - 2.2	1 - 2	0.35 – 1.75	180	[38]
$LiMn_2O_4/Li_4Mn_5O_{12}$	$Li_{0.55}La_{0.35}TiO_3$	0 – 1.5	0.032	0.00625	-	[23]
$LiCoO_2$/Si	LiPON	3 - 4	0.02	0.012	20	[33]
LiV_2O_5/SnN_x	LiPON	0.5 – 3.3	0.003 – 0.02	0.1 - 10	100	[34]
$LiNi_{0.8}Al_{0.1}Co_{0.1}O_2$/Si	SU8 soaked with 1M $LiClO_4$ in PC	2– 3.7	0.55 – 2.8	0.3 – 0.6	100	[35]
MnO_2/RuO_2	Poly(phenylene oxide) (PPO)	-	-	-	-	[27]
V_2O_5/Carbon	Poly(phenylene oxide) (PPO)	1.6 – 3.3	0.5	0.096	10	[28]
S/Carbon	Poly(phenylene oxide) (PPO)	1.5 - 3	1	0.5	10	[29]

Table 1. 2**:** Summary of cell design and performance various 3D micro-batteries

1.4.1. Electrode architectures that utilize liquid electrolyte

Min *et al.* developed a carbon-microelectromechanical systems (C-MEMS) process for fabricating three-dimensional battery architectures [24]. Two sets of interdigitated photoresist pillars were patterned by lithography and subsequently pyrolyzed at high temperatures in an oxygen-free environment. One set of the resulting high aspect ratio carbon arrays were used as the anode for the battery. The positive electrode array was fabricated by electrochemical deposition of dodecylbenzenesulfonate-doped polypyrrole (PPYDBS) on the other set of carbon pillars (See Figure 1.9). Electrochemical measurements showed that the PPYDBS showed improved specific capacity over a 2D film, owning to the larger active area from a 3D electrode. A 3D full cell was tested in liquid electrolyte and exhibited low capacity, likely limited by the poor electrical

conductivity of carbon arrays. In addition, z-direction height, and thus areal capacity of the electrode (0.01mAh/cm^2), is limited by height of the SU-8 photoresist (100 μm maximum).

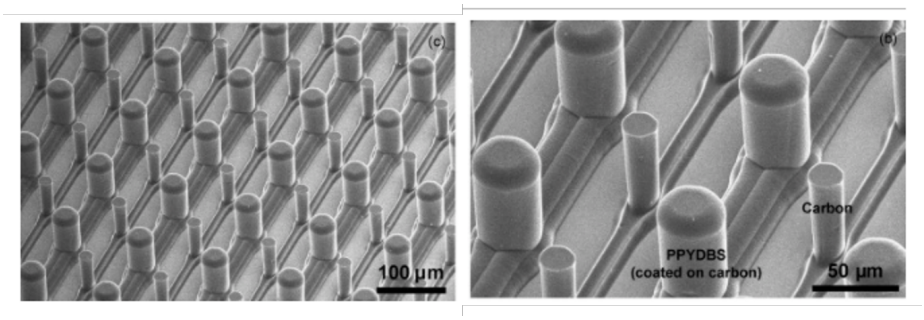

Figure 1. 9: Interdigitated carbon posts fabricated through MEMS techniques as Li-ion battery electrode [24]

Pikul *et al.* reported the fabrication of a 3D bicontinuous microelectrodes (Figure 1.10), using a similar interdigitated design to achieve fast ion transport between cathode and anode [30]. Polystyrene (PS) beads 300 nm in diameter were self-assembled onto a glass slide with interdigitated pattern of gold current collectors, followed by a sintering process to increase the interconnect area. Ni was electrodeposited onto both sets of gold current collectors through vacancies between the PS beads, which were then etched away in toluene, leaving behind a Ni network of interconnecting pores. Thin films of NiSn and $LiMnO_2$ (tens of nm in thickness) were each electrodeposited on one set of Ni to serve as the anode and cathode, respectively. The battery exhibited an ultrahigh power density of 7.4 mW cm^{2}μm^{-1}, owing to reduced charge transfer resistance and facilitated Li-ion diffusion in both liquid and solid phases. In addition, the interconnected Ni backbone

minimized the electrical resistance. However, due to the nature of the self-assembly of polystyrene beads, the z-direction height of the cell was limited to only 15μm and thus the areal capacity of the cell was low, prohibiting large-scale production of this type of cell.

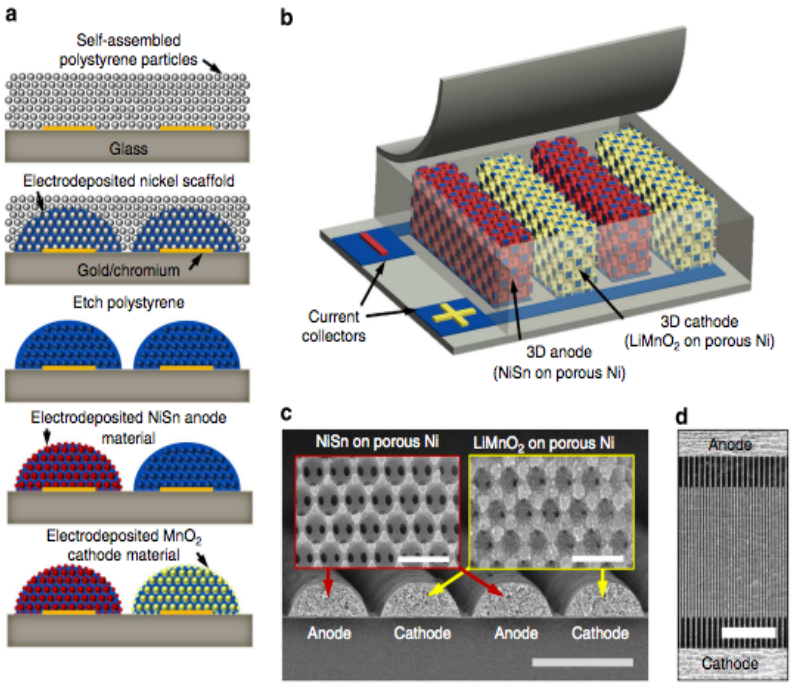

Figure 1. 10**:** Schematic of (a) The fabrication process (b) Micro-battery design (c) SEM cross-section and (d) top-down SEM view of the interdigitated micro-electrodes [30]

In recent years, 3D printing, also known as additive manufacturing, has become a popular micro-fabrication technique. Sun et al. used scalable 3D printing technique to fabricate 3D Li-ion micro-batteries that allowed functional inks to be precisely patterned in filamentary form [25] (See Figure 1.11 (a) and (b)). $LiFePO_4$ (LFO) cathode and $Li_4Ti_5O_{12}$ (LTO) anode powders were mixed with DI water, ethylene glycol, glyceral, and cellulose-based

viscosifiers, and printed onto high aspect ratio interdigitated microarrays on a sub-millimeter scale. The wall thickness of the electrodes was about 60 μm with height between 200 and 400 μm. Although the theoretical capacity of the electrode materials and the desirable full cell areal capacity of 1.5 mAh/cm^2 was achieved at lower C rates, the rate performance and further increase in areal capacity were limited by the poor electrical conductivity of the printing ink. Specifically, due to lack of a proper conductive agent, LFP electrodes printed with eight layers exhibited the same energy density as those with 16 layers. Wei et al improved the process and fabricated Li-ion micro-batteries that exhibit a ten-fold enhancement (15mAh/cm^2 for unpackaged cells and 4.5 mAh/cm^2 for fully packaged cells) in areal capacity compared to the cell in reference [25]. These biphasic electrodes consist of well-dispersed active material particles (LFO or LTO) mixed with attractive conductive carbon particles that form a percolative network within a lithium-based electrolyte solution [31]. In addition, the authors produced packaging and separator inks that can be UV-cured upon direct ink printing. Together, these inks were used to create fully 3D printed LIBs with thick electrodes patterned in arbitrary geometries (See Figure 1.11 (c)). However, these thick electrodes are still limited by electron or ion conduction since the power density is low (0.14 mA/cm^2).

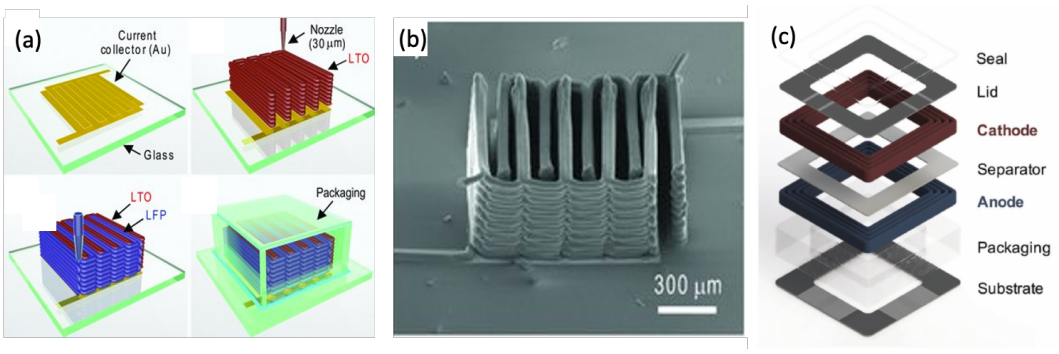

Figure 1. 11**:** (a) Fabrication procedure for 3D printed LFP/LTO interdigitated electrodes [25] (b) SEM image of printed and annealed 16-layer LFP/LTO electrode architecture [25] (c) Schematic representation of fully 3D printed Li-ion square cell battery with outer dimension of 1cm * 1cm * 2.5mm and inner hole dimensions of 6mm * 6mm [31]

1.4.2. Electrode architectures that utilize solid electrolyte or gel electrolyte

Nathan *et al.* demonstrated the first working 3D rechargeable Li-ion micro-battery that is compatible with MEMS requirement using gel electrolyte (See Figure 1.12) [32]. The films were deposited sequentially on the surface of a perforated silicon micro-channel plate 0.5mm thick and 13mm in diameter, with 50 µm diameter hexagonal microchannels separated by 10 µm walls. The 3D micro-battery was comprised of a nickel cathode current collector, which was electrolessly deposited onto the microchannel plate, a MoS_2 cathode electroplated onto the nickel, a hybrid polymer electrolyte and a lithiated graphite anode infiltrated into the microchannel. A graphite anode also served as the anode current collector. The cell exhibited good cycle performance and an areal capacity of 2 mAh/cm^2, approximately 30 times higher than the capacity of a similarly built planar cell with the same footprint area and cathode thickness. The capacity gain corresponded well with the areal gain. However, when increasing the current during testing, a significant overpotential

was observed, likely due to the use of low electrical conductivity graphite anode as the current collector.

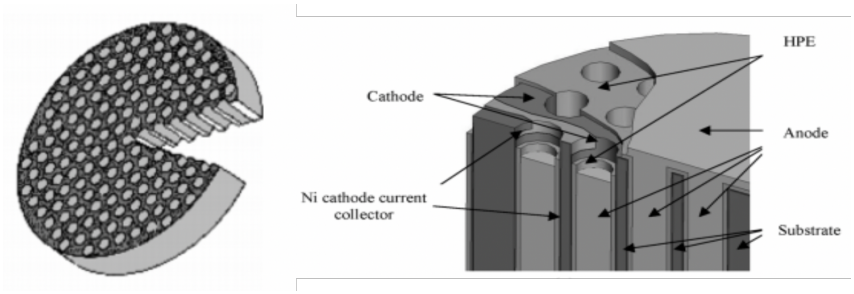

Figure 1. 12**:** Perforated silicon micro-channels as scaffold for Li-ion battery full cell [32]

Kotobuki *et al.* reported the fabrication of an all-solid-state battery using a pre-fabricated $Li_{0.55}La_{0.35}TiO_3$ (LLT) honeycomb scaffold [23], with micro-sized holes on both sides of the membrane. Each hole has a dimension of 180 μm x 180 μm x 180 μm, with 80 μm spacing between holes (See Figure 1.13). The full cell was constructed by impregnating cathode and anode materials on each side, respectively. The full cell capacity (0.032 mAh/cm^2) was likely limited by the long Li ion diffusion distance within the hole and from one hole to another.

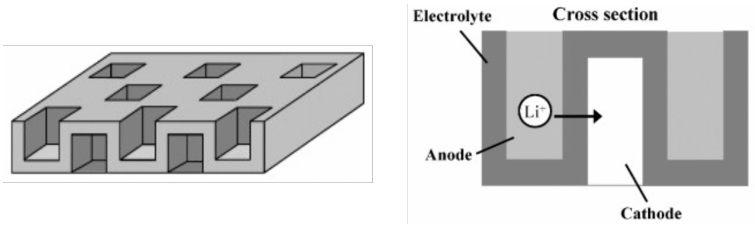

Figure 1. 13**:** Fabrication of an all-solid-state battery using a pre-fabricated $Li_{0.55}La_{0.35}TiO_3$ (LLT) honeycomb scaffold [23]

Physical vapor deposition such as sputtering and pulse laser deposition has been used to

deposit battery active materials for thin film batteries. However, these techniques are limited by their line-of-sight nature when they are applied to deposit materials onto 3D structures. Talin *et al.* described the experimental testing and simulation of 3D solid state Li-ion battery, consisting of 3D Si microcolumns onto which Pt cathode current collector, $LiCoO_2$ cathode, LiPON electrolyte, Si anode, and Cu anode current collector were sequentially deposited through physical vapor deposition (See Figure 1.14) [33]. The areal capacity was 0.02 mAh/cm^2, with poor power performance, which the authors attributed to non-uniform geometry resulting from the physical vapor deposition technique along with the finite conductance of the LiPON solid electrolyte. The authors suggested the existing PVD process appropriate for planar geometry SSLIBs will likely have to be replaced by alternate processes capable of uniformly coating high aspect ratio microstructures.

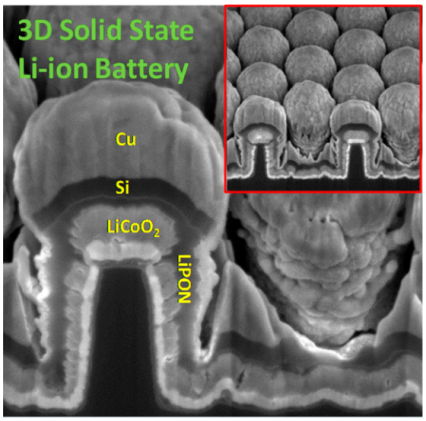

Figure 1. 14**:** 3D solid state Li-ion battery fabricated by PVD onto silicon micro-columns [33]

Compared to physical vapor deposition, a better approach to fabricating full cells with uniform thickness in high aspect ratio 3D structures is to use vapor-phase and self-limiting chemistry methods such as atomic vapor deposition (ALD) [34]. Pearse et al reported the

realization of fully conformal 3D all solid-state thin film battery through ALD [34]. All active battery components – electrodes, solid electrolyte, and current collectors were deposited by ALD onto standard CMOS processable silicon wafers micro-fabricated to form arrays of deep pores with aspect ratio up to 10 (See Figure 1.15). Conformal deposition enabled by ALD onto 3D substrates successfully increased the areal discharge capacity with only 0.02% per-cycle capacity fade. However, the areal capacity was still limited to 0.02-0.03 mAh/cm^2 due to the inability to scale up the ALD process.

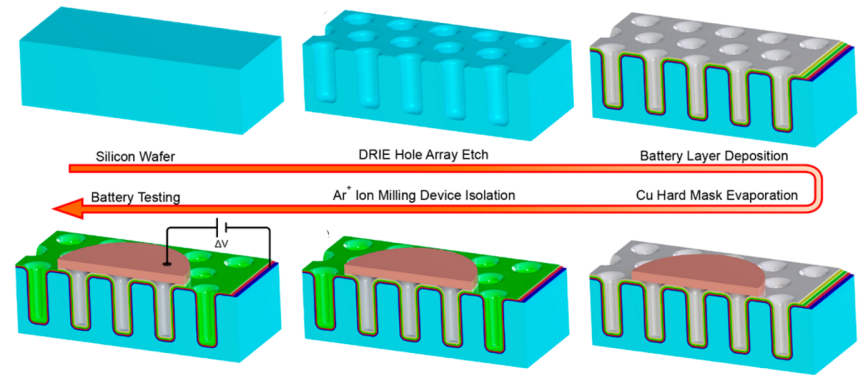

Figure 1. 15**:** Schematic of fabrication of an all-ALD 3D micro-battery [34]

Lithography may also be used to coat conformal layer of electrolyte on 3D surfaces. Hur et al. demonstrated a novel method of fabricating and assembling 3D lithium-ion microbatteries with good areal capacity and high capacity retention [35]. The interdigitated 3D architecture-adapted semiconductor processing method known as deep reactive etching (DRIE) was combined with a photo-patternable polymer electrolyte derived from SU-8 photoresist to obtain a conformally coated cylindrical silicon electrode array. Lithium transition metal oxide cathode was then infiltrated into the trenches of the array, forming a full battery (See Figure 1.16). The full battery delivered discharge capacities up to 1.8

mAh/cm^2, but the cycling was unstable with low Coulombic efficiency. It was able to operate at low discharge current density of 0.22 mAh/cm^2 and survive 100 cycles at 0.5 mAh/cm^2.

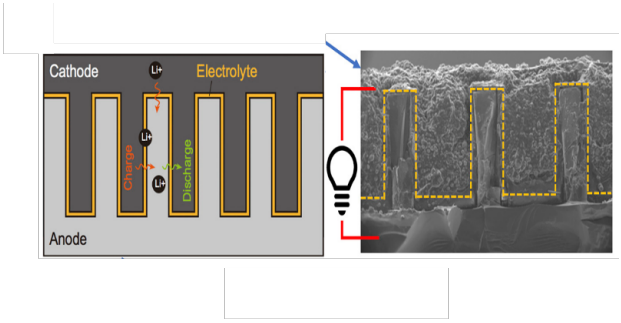

Figure 1. 16**:** High areal capacity 3D micro-battery enabled by lithography techniques [35]

Self-limiting electrodeposition of polymers may also provide a solution for pinhole free and conformal films. The electrodeposition process is self-limited due to insulating nature of the deposited polymer films. As indicated in Figure 1.17 below [36], although growth may happen faster initially at top surfaces of a 3D structure, at later stages growth at the top surfaces will be self-limited and growth at the bottom uncovered part will be become more rapid, resulting in a conformal coverage.

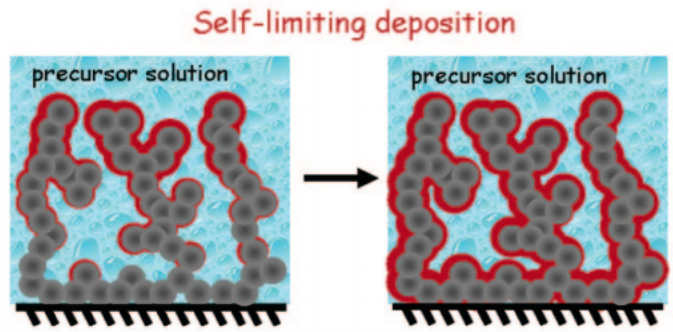

Figure 1. 17**:** Illustration of self-limiting polymer electrodeposition [36]

Poly(phenylene oxide) (PPO) has attracted attention as a potential material for use as solid

electrolyte since it is electrically insulating, conducts Li ions, and can be fabricated through self-limiting electrodeposition onto 3D surfaces. Rhodes *et al.* developed a 3D nanoarchitecture where three critical components of a battery – cathode, polymer electrolyte, and anode – were internally assembled as tricontinuous phases (See Figure 1.18 (b)) [27]. The MnO_2 cathode was covered by an ultrathin, conformal layer of PPO. However, the full cell testing resulted in the shortage of the battery, which the authors attributed to RuO_2 anode that converted the PPO into a mixed electron-ion conductor. In addition, it is anticipated that the capacity of the cell would be negligible due to nanometer scale of the electrodes. Ergang *et al.* used similar technique to deposit PPO onto a microporous carbon anode, followed by infiltration of V_2O_5 ambigel cathode (See Figure 1.19 (a)) [28]. The cell capacity was low at 0.5 mAh/cm^2 and limited by poor electronic conductivity of V_2O_5 cathode.

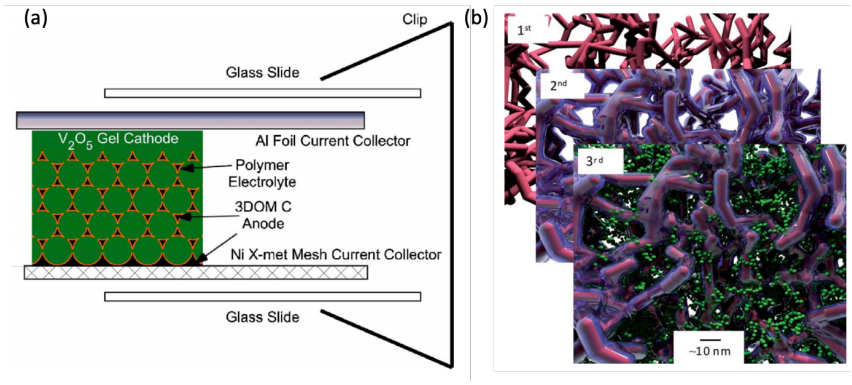

Figure 1. 18**:** (a) Schematic showing cell design in [28] (b) Schematic showing cell design in [27]

Werner *et al.* presented the synthesis of co-continuous nanohydrids with all necessary components rationally integrated in a triblock terpolymer derived core-shell double gyroid

architecture [29]. In this design, 3D periodically ordered, functional anode and cathode nanonetworks were separated by an ultrathin electrodeposited PPO layer (See Figure 1.19). All materials were less than 20nm in their layer dimensions, co-continuous, and interpenetrating in 3D, and extended throughout the monolith [29]. Although the full cell delivered an expected OCV, suggesting that the PPO layer was likely pin-hole free, cycling performance was unsatisfactory with areal capacity less than 1 mAh/cm^2 and 30-40% capacity retention after 10 cycles.

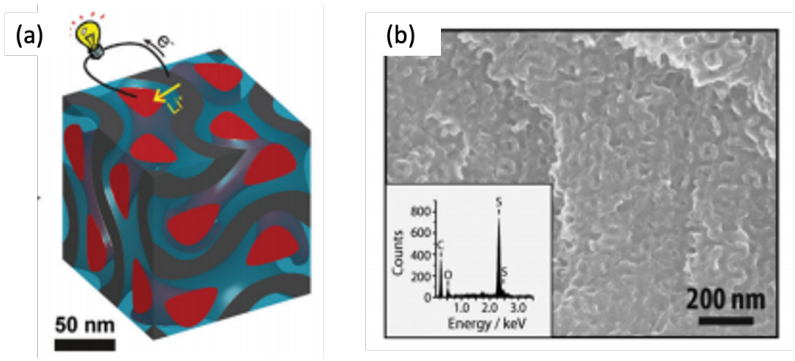

Figure 1. 19: (a) Schematic showing design of the co-continuous nanohybrid battery (b) SEM image of the battery cross-section [29]

1.5. Contributions of this work:

Compared to their 2D counterparts, several of the electrodes reviewed above exhibited higher areal capacity owing to the increased surface area from the 3D architecture. However, these electrodes suffered from issues such as poor electrical conduction [23-25][31-32], non-uniformity in material deposition [33], and inability to scale-up to the energy needs of microelectronic devices (3 – 10 mAh/cm^2) [27-30][34]. It is also not clear whether these electrodes would be capable of exhibiting the same power performance when

scaled up to sizes suitable for microelectronic applications [37].

The study reported herein involves design and fabrication of scalable, high surface area, and porous 3D metal network-based Li-ion micro-batteries that will meet the demands of commercial microelectronics. A facile high current hydrogen-templated electroplating technique is utilized to generate 3D porous microstructures, which serve as the scaffolds, current collectors, or even active materials for battery electrodes. In addition, a solid polymer electrolyte or gel electrolyte is utilized to increase stability and safety of the energy storage device. This approach resolves the poor electrical connection issues for scaled-up micro-batteries encountered in previous studies, as an interconnected porous metal network is used as the backbone to facilitate electron conduction. Combined with unimpeded transport of Li-ions in the porous electrode designed with low tortuosity, the power density is also at the upper end of the scope for microelectronics devices (Figure 1.2 (a)). Coupled with MEMS technologies, electrochemical techniques such as controlled electroplating and stripping have enabled uniform deposition of active material onto a 3D structure millimeter scale in height, which ensures uniform current distribution during battery operations. Areal capacity high as 40 mAh/cm^2 has been demonstrated on the half-cell level, which can be attributed to the scalability, high surface area, facile ion transport, and good electrical conduction from the porous electrodes. On the full cell level, areal capacity of 3 mAh/cm^2 has been attained with 2.3 mWh/cm^2 areal power density. This performance is within the upper range of the micro-batteries developed so far. Details about the fabrication and performance of these structures are available in the forthcoming chapters of this study.

1.6. Thesis outline

The body of this thesis is divided into six chapters. Chapter 1 is the introductory section starting with the motivation behind the study reported. After indicating the devices of interest for high areal capacity energy storage applications, a discussion on conventional 2D thin film micro-batteries and how it can be improved by design of 3D porous electrodes is presented. In addition, advantages of solid-state electrolyte over traditional organic liquid electrolyte are examined. A detailed review of high areal capacity 3D electrode designs thus far is then presented, followed by contributions of this work by introducing a facile and scalable approach to produce high areal capacity full cell with superior power density.

Chapter 2 demonstrates the one-step hydrogen-templated high current electroplating method to deposit scalable and highly porous Cu, NiSn, Au scaffold in a facile fashion. This chapter examines the effect of different deposition conditions using porous NiSn as an example.

Chapter 3 presents one approach of porous Li-ion micro-battery fabrication. Porous copper is used as the scaffold as described in Chapter 2. A secondary metal coating is deposited on the porous copper to increase the mechanical rigidity without sacrificing surface area and porosity of the electrode. NiSn and Sulfur are chosen as the anode and cathode materials and electrodeposited onto the rigid porous current collectors, respectively. A gel polymer electrolyte is formed in-situ by heat-initiated polymerization. Electrode

characterizations and electrochemical testings are described. In addition, capacity loss mechanisms in full cells and potential methods to resolve the issue are discussed.

Chapter 4 demonstrates a second approach to fabricate a monolithic piece of micro-battery. A porous composite of NiSn/Si is deposited by a modified method of hydrogen-templated electroplating. The electrode exhibits an ultrahigh capacity of 40 mAh/cm^2. With the incorporation of binder materials, change of deposition conditions, and electrode substrate design, superior energy performance and long cycle life are achieved. Poly(phenylene oxide) (PPO) polymer electrolyte is then anodically deposited onto the anode scaffold surface. Subsequently, cathode slurry is infiltrated into the electrolyte/anode composite, with silver epoxy on top as electrical contact. Cell testing results are discussed, including an investigation on possible issues and failure mechanisms of polymer electrolyte plating.

In Chapter 5, a proof-of-concept multilayer $Ni(OH)_2$ electrode is used to show how electrochemical principles may be used to optimize design of 3D batteries using a mathematical model. In addition, various advanced electrochemical techniques such as cyclic voltammetry (CV), galvanostatic intermittent titration (GITT), and electrochemical impedance spectroscopy (EIS) are used to measure physical parameters, which are essential to accuracy of the model. With similar electrochemical principles, such a model may be extended to porous electrodes as well.

Chapter 6 is devoted to the concluding summary of the whole study. The overall contributions of this study are presented. Also, some recommendations pertaining to future

research such as other applications for porous structures, optimization of active material deposition conditions, and different routes for monolithic battery fabrication, are given.

1.7. References

1. Zheng, S., Shi, X., Das, P., Wu, Z. S., & Bao, X. (2019). The Road Towards Planar Microbatteries and Micro-Supercapacitors: From 2D to 3D Device Geometries. *Advanced Materials*, *31*(50), 1900583.
2. Mack, C. A. (2011). Fifty years of Moore's law. *IEEE Transactions on semiconductor manufacturing*, *24*(2), 202-207.
3. Tarascon, J. M., & Armand, M. (2010). Issues and challenges facing rechargeable lithium batteries. *Materials for sustainable energy, 401*,171-179.
4. Arthur, T. S., Bates, D. J., Cirigliano, N., Johnson, D. C., Malati, P., Mosby, J. M., ... & Dunn, B. (2011). Three-dimensional electrodes and battery architectures. *Mrs Bulletin*, *36*(7), 523.
5. Wang, Y., Liu, B., Li, Q., Cartmell, S., Ferrara, S., Deng, Z. D., & Xiao, J. (2015). Lithium and lithium ion batteries for applications in microelectronic devices: A review. *Journal of Power Sources*, *286*, 330-345.
6. Zhang, P., Wang, F., Yu, M., Zhuang, X., & Feng, X. (2018). Two-dimensional materials for miniaturized energy storage devices: from individual devices to smart integrated systems. *Chemical Society Reviews*, *47*(19), 7426-7451.
7. Ferrari, S., Loveridge, M., Beattie, S. D., Jahn, M., Dashwood, R. J., & Bhagat, R. (2015). Latest advances in the manufacturing of 3D rechargeable lithium microbatteries. *Journal of Power Sources*, *286*, 25-46.
8. Chmiola, J., Largeot, C., Taberna, P. L., Simon, P., & Gogotsi, Y. (2010). Monolithic carbide-derived carbon films for micro-supercapacitors. *science*, *328*(5977), 480-483.
9. Zheng, S., Ma, J., Wu, Z. S., Zhou, F., He, Y. B., Kang, F., ... & Bao, X. (2018). All-solid-state flexible planar lithium ion micro-capacitors. *Energy & Environmental Science*, *11*(8), 2001-2009.
10. Wu, Z. S., Feng, X., & Cheng, H. M. (2014). Recent advances in graphene-based planar micro-supercapacitors for on-chip energy storage. *National Science Review*, *1*(2), 277-292.

11. Salot, R., Martin, S., Oukassi, S., Bedjaoui, M., & Ubrig, J. (2009). Microbattery technology overview and associated multilayer encapsulation process. *Applied surface science*, *256*(3), S54-S57.
12. Liu, L., Zhao, H., & Lei, Y. (2019). Advances on three-dimensional electrodes for micro-supercapacitors: a mini-review. *InfoMat*, *1*(1), 74-84.
13. McCloskey, B. D. (2015). Expanding the Ragone plot: Pushing the limits of energy storage. *Journal of Physical Chemistry Letters, 6*(18), 3592–3593.
14. Chen, H., Cartmell, S., Wang, Q., Lozano, T., Deng, Z. D., Li, H., ... & Xiao, J. (2014). Micro-battery development for juvenile salmon acoustic telemetry system applications. *Scientific reports*, *4*, 3790.
15. News.panasonic.com. (2014). *Panasonic Commercializes the Industry's Smallest*1 Pin Shaped Lithium Ion Battery*. Retrieved from https://news.panasonic.com/global/press/data /2014/10/ en141003-2/en141003-2.html
16. Cook-Chennault, K. A., Thambi, N., & Sastry, A. M. (2008). Powering MEMS portable devices—a review of non-regenerative and regenerative power supply systems with special emphasis on piezoelectric energy harvesting systems. *Smart materials and structures*, *17*(4), 043001.
17. Bates, J. B., Dudney, N. J., Neudecker, B., Ueda, A., & Evans, C. D. (2000). Thin-film lithium and lithium-ion batteries. *Solid state ionics*, *135*(1-4), 33-45.
18. Long, J. W., Dunn, B., Rolison, D. R., & White, H. S. (2004). Three-dimensional battery architectures. *Chemical Reviews*, *104*(10), 4463-4492.
19. Sun, H., Zhu, J., Baumann, D., Peng, L., Xu, Y., Shakir, I., ... & Duan, X. (2019). Hierarchical 3D electrodes for electrochemical energy storage. *Nature Reviews Materials*, *4*(1), 45-60.
20. Kuang, Y., Chen, C., Kirsch, D., & Hu, L. (2019). Thick electrode batteries: principles, opportunities, and challenges. *Advanced Energy Materials*, *9*(33), 1901457.
21. Pikul, J. H., & Long, J. W. (2019). Architected materials for advanced electrochemical systems. *MRS Bulletin*, *44*(10), 789-795.

22. Jung, D. S., Hwang, T. H., Park, S. B., & Choi, J. W. (2013). Spray drying method for large-scale and high-performance silicon negative electrodes in Li-ion batteries. *Nano letters*, *13*(5), 2092-2097.
23. Kotobuki, M., Suzuki, Y., Munakata, H., Kanamura, K., Sato, Y., Yamamoto, K., & Yoshida, T. (2011). Effect of sol composition on solid electrode/solid electrolyte interface for all-solid-state lithium ion battery. *Electrochimica Acta*, *56*(3), 1023-1029.
24. Min, H. S., Park, B. Y., Taherabadi, L., Wang, C., Yeh, Y., Zaouk, R., ... & Dunn, B. (2008). Fabrication and properties of a carbon/polypyrrole three-dimensional microbattery. *Journal of Power Sources*, *178*(2), 795-800.
25. Sun, K., Wei, T. S., Ahn, B. Y., Seo, J. Y., Dillon, S. J., & Lewis, J. A. (2013). 3D printing of interdigitated Li-Ion microbattery architectures. *Advanced materials*, *25*(33), 4539-4543.
26. Chen, R., Li, Q., Yu, X., Chen, L., & Li, H. (2019). Approaching practically accessible solid-state batteries: stability issues related to solid electrolytes and interfaces. *Chemical Reviews, 120*(40), 6820-6877.
27. Rhodes, C. P., Long, J. W., Pettigrew, K. A., Stroud, R. M., & Rolison, D. R. (2011). Architectural integration of the components necessary for electrical energy storage on the nanoscale and in 3D. *Nanoscale*, *3*(4), 1731-1740.
28. Ergang, N. S., Fierke, M. A., Wang, Z., Smyrl, W. H., & Stein, A. (2007). Fabrication of a fully infiltrated three-dimensional solid-state interpenetrating electrochemical cell. *Journal of the Electrochemical Society*, *154*(12), 1135-1139.
29. Werner, J. G., Rodríguez-Calero, G. G., Abruña, H. D., & Wiesner, U. (2018). Block copolymer derived 3-D interpenetrating multifunctional gyroidal nanohybrids for electrical energy storage. *Energy & Environmental Science*, *11*(5), 1261-1270.
30. Pikul, J. H., Zhang, H. G., Cho, J., Braun, P. V., & King, W. P. (2013). High-power lithium ion microbatteries from interdigitated three-dimensional bicontinuous nanoporous electrodes. *Nature communications*, *4*(1), 1-5.
31. Wei, T. S., Ahn, B. Y., Grotto, J., & Lewis, J. A. (2018). 3D printing of customized li-ion batteries with thick electrodes. *Advanced Materials*, *30*(16), 1703027.

32. Nathan, M., Golodnitsky, D., Yufit, V., Strauss, E., Ripenbein, T., Shechtman, I., ... & Peled, E. (2005). Three-dimensional thin-film Li-ion microbatteries for autonomous MEMS. *Journal of microelectromechanical systems*, *14*(5), 879-885.
33. Talin, A. A., Ruzmetov, D., Kolmakov, A., McKelvey, K., Ware, N., El Gabaly, F., ... & White, H. S. (2016). Fabrication, testing, and simulation of all-solid-state three-dimensional Li-ion batteries. *ACS applied materials & interfaces*, *8*(47), 32385-32391.
34. Pearse, A., Schmitt, T., Sahadeo, E., Stewart, D. M., Kozen, A., Gerasopoulos, K., ... & Gregorczyk, K. E. (2018). Three-dimensional solid-state lithium-ion batteries fabricated by conformal vapor-phase chemistry. *ACS nano*, *12*(5), 4286-4294.
35. Hur, J. I., Smith, L. C., & Dunn, B. (2018). High areal energy density 3D lithium-ion microbatteries. *Joule*, *2*(6), 1187-1201.
36. Long, J.W. and Rolison, D.R. (2007) Architectural Design, Interior Decoration, and Three-Dimensional Plumbing en Route to Multifunctional Nanoarchitectures. Accounts of Chemical Research, 40(9), 854-862
37. Armutlulu, A. (2014). Deterministically engineered, high power density energy storage devices enabled by MEMS technologies (Doctoral dissertation, Georgia Institute of Technology).
38. Nathan, M., Golodnitsky, D., Yufit, V., Strauss, E., Ripenbein, T., Shechtman, I., ... & Peled, E. (2005). Three-dimensional thin-film Li-ion microbatteries for autonomous MEMS. *Journal of microelectromechanical systems*, *14*(5), 879-885.

CHAPTER 2: FABRICATION OF POROUS METAL ELECTRODES USING HYDROGEN-TEMPLATED ELECTRODEPOSITION

In previous studies, novel designs for high surface area electrode architectures, including carbon posts enabled by MEMS techniques [1], inverse-opal nanoporous Ni [2], perforated silicon micro-channel plate [3][4], and honeycomb-shaped ceramic electrolyte [5] have been developed. However, these structures often lack scalability in their fabrication methods, resulting in an overall low areal capacity. In addition, the fabrication for these structures often involve complicated and expensive processes, such as lithography, self-assembly, and atomic layer deposition. Thus, more scalable and economically viable methods for generating battery scaffolds are required. Furthermore, among various 3D architectures, the 3D porous structure is highly desirable for constructing high-performance electrodes [18]. Porous electrodes possess high surface area to facilitate fast reaction kinetics. Also, high porosity electrodes are instrumental in improving ion transport and enabling volume expansion of conversion-type electrode materials such as Si, NiSn, and S. Herein, a facile and scalable electrochemical process is developed for the fabrication of a porous metal network with high surface area and low tortuosity, which may either be used as a current collector or the battery anode.

For the hydrogen-templated porous metal electrodeposition, a metal substrate (usually Cu) is used as the cathode and an inert metal (e.g. Pt) as the anode [6][7]. The electrodeposition bath is comprised of metal salts, depending on the target metal network and an acid as the proton source e.g. sulfuric acid. A large current density ranging from 3 – 5 A/cm^2 is applied.

As shown in Figure 2.1, under this high cathodic current density, hydrogen bubbles evolve from the metal substrate surface from reduction of H^+ (according to equation 1 below). Specifically, three steps are involved in this bubble generation process: nucleation, growth, and detachment. The bubble grows while in contact with the electrode during its residence time on the surface, with a decreasing contact angle, until detachment [14]. Concurrently, metal cations also are deposited (Equation 2 below) using the hydrogen bubbles as dynamic templates, thus forming a porous metal network. In the regions with bubbles, no metal deposition will occur since there are no metal ions available [7]. It has been reported that the nature of the initial hydrogen evolution from the surface in terms of bubble coalescence and residence time affect the porous metal morphology throughout the deposition process [17]. Note that the surface pore size increases with the deposition time, since the bubbles coalesce as they rise. This creates a favorable porosity profile to facilitate electrolyte penetration into the bulk structure for battery applications [8].

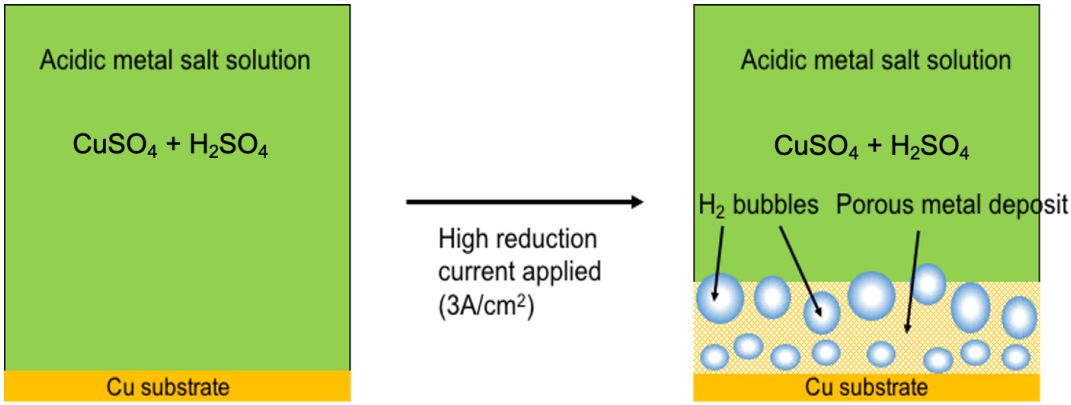

Figure 2. 1: Graphical illustration of hydrogen-templated electrodeposition process

$$2H^+ + 2e^- \rightarrow H_2 \quad (1)$$

$$M^{2+} + 2e^- \rightarrow M \quad (2)$$

In this work, the hydrogen-templated electrodeposition method is utilized to fabricate two types high surface area porous metal, namely Cu and NiSn alloy. Specifically, porous Cu can be used as a current collector scaffold, on which subsequent thin films of active material can be deposited. Porous NiSn may itself serve as both the anode current collector and the anode active material, eliminating the complexity of active material deposition onto 3D structures. However, as will be discussed in Chapter 3, due to lack of a proper binder material, these types of structure can suffer from cyclability issues.

2.1. Porous copper as current collector

For porous copper deposition, a baseline bath containing 0.4 M $CuSO_4$ as the metal salt and 1.5M H_2SO_4 as the proton source is utilized. A two-electrode configuration may be used, where Pt mesh is used as the counter electrode (anode) and 0.125mm thick Cu foil as the working electrode (cathode). The two electrodes are spaced approximately 3 cm apart. There is no need to immerse the Cu substrate in acid solution to remove the native oxide layer prior to deposition since the deposition bath is highly acidic. Current density varies from 3 to 5 A/cm^2. Deposition duration vary from 10s to 960s, resulting in different sample thicknesses. Figure 2.2 shows the SEM image resulting from 20s of deposition, at different levels of magnifications (left to right: low to high). As shown, highly porous structures were formed due to the templating effect of the hydrogen bubbles. In addition, vigorous hydrogen evolution originated not only on the substrate but also at the deposited copper walls, forming pores on the μm scale and thus further enlarging the surface area.

The dendritic feature of the deposits is caused diffusion-limited growth of copper under highly cathodic conditions, leading to ramifications and fractal patterns [11]. Popov et al summarized the condition for such dendritic growth in the equation below [12]:

$$\eta > \eta_i = \frac{RT}{nF}\frac{j_L}{j_0} \tag{3}$$

where η is the metal deposition over-potential, j_L and j_0 are the limiting and exchange current densities of metal ion reduction, R is the gas constant, T is the temperature, n is the number of electrons involved in the electrochemical reaction, and F is the Faraday's constant. Additionally, owing to the rigorous gas evolution on growing copper tips in this work, a local turbulence of electrolyte might be created around the copper tips, disrupting continuous growth of the copper tips and promoting the formation of new nuclei with random orientation on the tips [7].

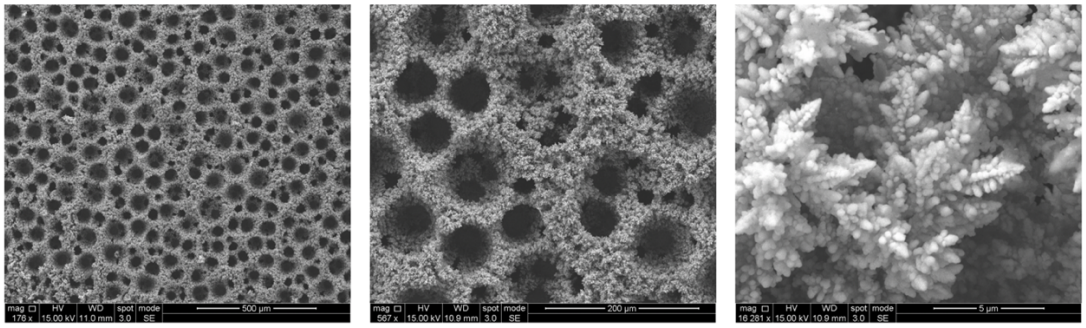

Figure 2. 2**:** SEM image of porous copper deposited using hydrogen-templated electrodeposition at different magnifications

The hydrogen-templated electrodeposition method is highly scalable, as we can see from Figure 2.3 below. Structures ranging from 100 μm to mm scale in z direction height can be created simply by changing the deposition duration.

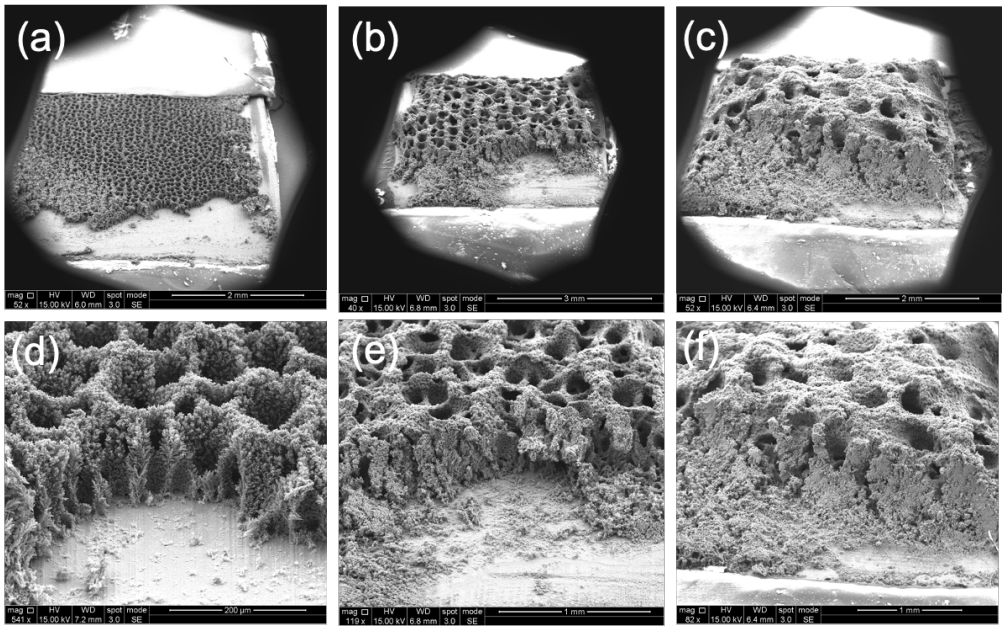

Figure 2. 3**:** Cross-sectional SEM image of porous copper with different durations at 3A/cm^2 (a)(d): 20s (130 μm tall) (b)(e): 60s (500 μm tall) (c)(f): 180s (850 μm tall)

Figure 2.4 shows the microscope images of porous copper depositions with increasing deposition times. The pore size at the surface increases with deposition time or height of the electrode. This is due to coalescence of bubbles as they rise, which in turn is hypothesized to be driven by the long-range hydrophobic force of bubbles being sufficient to overcome the hydrodynamic repulsive force between the bubbles [13].

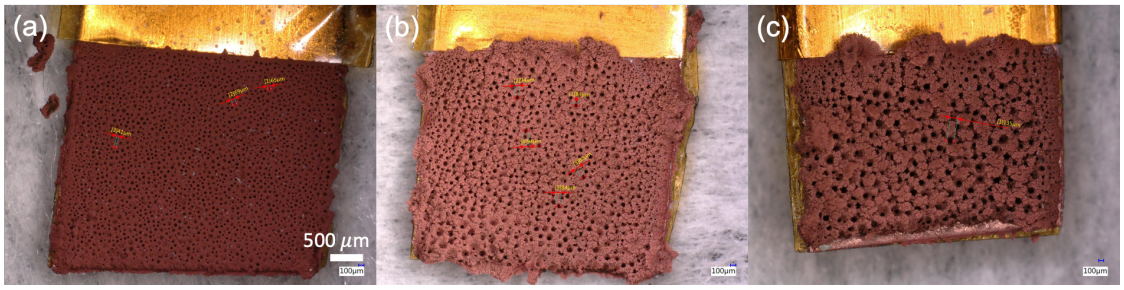

Figure 2. 4**:** Microscope image of porous copper with different deposition times at 5A/cm^2 (a) 20s (b) 320s (c) 720s

The use of additives may be used to tailor the morphology, such as pore size, of the deposits. Since the bubble coalescence is driven by hydrophobic force, decreasing the hydrophobic force suppresses bubble coalescence and thus results in a reduction of pore size and a higher surface area. Acetic acid is commonly used as a bubble stabilizer and is suitable for the current application since no additional metal ions are involved [13]. As we can see from Figure 2.5, with the addition of acetic acid, the surface pore size is reduced significantly. However, for battery applications, although an increase in the surface area may reduce the overall impedance and improve the reaction kinetics, the tortuosity of the electrode may increase, which reduces the effective diffusion coefficient of Li ions in the electrolyte phase during battery operation and sacrifices power density. In addition, it was observed that addition of acetic acid retards the growth rate of the porous metal, which has also been reported in literature [8].

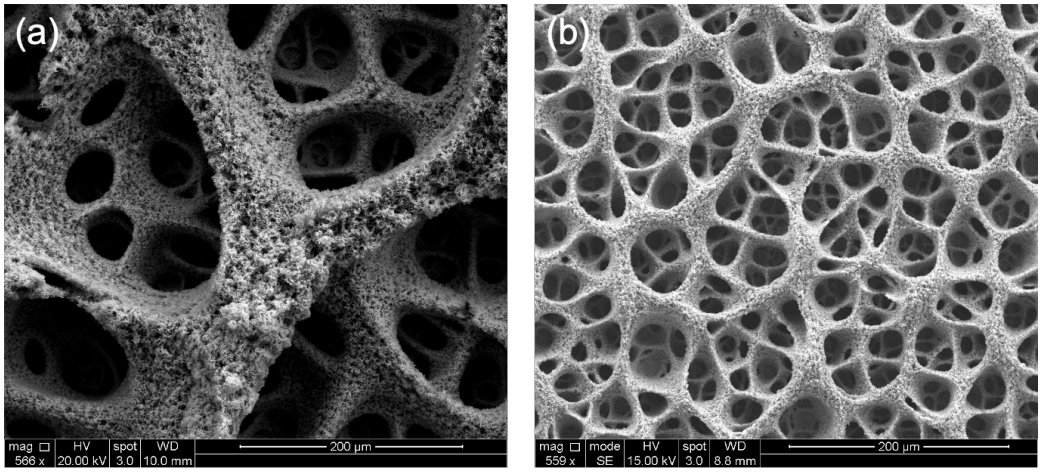

Figure 2. 5**:** SEM images of porous Cu deposited with (a) 0.4M $CuSO_4$ + H_2SO_4 (b) 0.4M $CuSO_4$ + H_2SO_4 + 0.2M acetic acid

In order to facilitate subsequent metal depositions (e.g. additional layers of Cu/Ni and active material, as will be discussed in Chapter 4) and to decrease the electrode tortuosity, a green laser was used to drill holes into the Cu foil substrate, on which porous copper was subsequently deposited. As shown in Figure 2.6, porous copper grew around the holes in vertical direction, forming well-structured cylindrical tunnels throughout thickness of the sample. During further active material deposition, the electrolyte ions may access the bottom part of the 3D structure from the backside (substrate side) and avoid the longer path from the front side, thus alleviating potential mass transfer issues and resulting in a more uniform deposition in the z-direction. In addition, during battery operations, these cylindrical tunnels will lower tortuosity of the electrode, reducing the effective ion diffusion coefficient and facilitating ion transport.

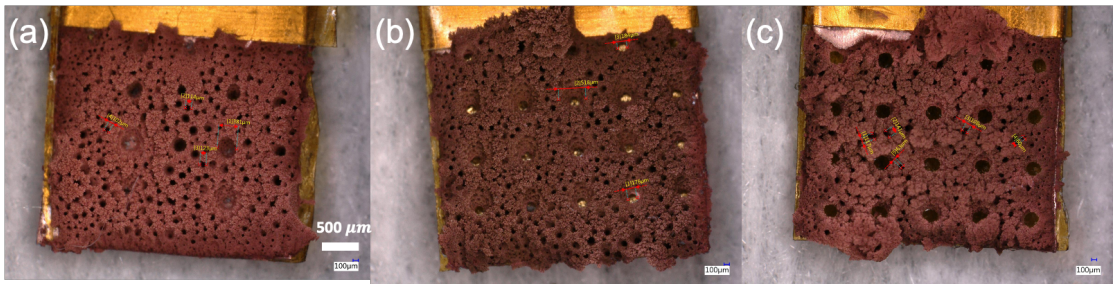

Figure 2. 6**:** Microscope top view images of porous copper deposit on Cu substrates prefabricated with laser-machined holes (a) 100 μm diameter (b) 200 μm diameter (c) 400 μm diameter

2.2. Porous Nickel Tin (NiSn) alloy as anode material

Similar to deposition of porous copper, NiSn, a high energy density anode material, can be deposited using hydrogen-templated electrodeposition. Tin has been widely studied as Li-ion battery anode material because of its much higher theoretical capacity (991 mAh/g; 7200 mAh/mL) than graphite (372 mAh/g; 837 mAh/mL) [14]. In addition, tin or its alloy can be electrodeposited and thus is compatible with micro-fabrication processes. However, similar to silicon, tin experiences severe volumetric expansion/contraction (up to 360%) during cycling, which makes it impractical to use pure tin metal as electrode for rechargeable batteries [15]. One way to alleviate this issue is to utilize tin-based intermetallic compounds such as NiSn, where Ni acts as an inactive backbone to buffer the volumetric expansion of Sn. During cell cycling, the electrochemical reaction at NiSn anode side proceeds as follows:

$$4.4Li + NiSn \leftrightarrow Li_{4.4}Sn + Ni \tag{4}$$

In this study, the effect of various process conditions such as bath composition, current

density, and pulse plating on the deposited electrode using hydrogen-templated electrodeposition was investigated and the control of the morphology and composition of the electrode to achieve desired battery performance was demonstrated.

A bath containing nickel chloride ($NiCl_2$), tin chloride ($SnCl_2$), and sulfuric acid (H_2SO_4) was used for the hydrogen-templated electrodeposition of porous NiSn. Pt was used as the counter electrode. A three-electrode set-up with Ag/AgCl in 3M KCl as the reference is used for precise control of overpotential. Table 2.1 below lists different bath compositions used for the investigation and Table 2.2 lists the experimental conditions and some measurement results including deposited mass, pore size, wall thickness, and Sn ratio. All depositions either were performed for 30s continuously, or had a summation of non-zero current for 30s for experiments with pulse plating.

	$NiCl_2$ conc., M	$SnCl_2$ conc., M	H_2SO_4 conc., M
Bath 1 (baseline bath)	0.2	0.02	1
Bath 2	0.2	0.02	0.2
Bath 3	0.4	0.04	1
Bath 4	0.2	0.02	0.1
Bath 5	0.2	0.04	0.2
Bath 6	0.2	0.015	1

Table 2. 1**:** Bath composition for porous NiSn deposition

	Bath	Applied current, A/cm^2	Pulse plating?	Mass of deposit, mg	Sn atomic ratio	Average pore diameter, μm	Average wall thickness, μm
Dep1	1	2	No	0.44	0.68	30	10
Dep2	2	2	No	1.22	0.31	30	20-30
Dep3	4	2	No	0.09	0.25	NA	NA
Dep4	1	2	On/Off = 1s:1s	0.3	0.41	13	8
Dep5	1	2	On/Off = 1s:3s	0.4	0.42	10-20	7
Dep6	1	2	On/Off = 1s:10s	0.24	0.40	6	5
Dep7	2	2	No	1.23	0.40	22	23
Dep8	5	2	No	1.25	0.68	32	35
Dep9	6	2	No	0.28	0.57	11	7
Dep10	3	2	No	0.68	0.53	30	10-20
Dep11	2	1	No	1.01	0.45	30	29

Table 2. 2**:** Bath composition for porous NiSn deposition

2.2.1. Effect of acid concentration

As the acid concentration decreases (see Dep1 vs Dep2 in Table 2.2), there is a significant increase in deposited mass due to decreased amount of charge used for hydrogen gas generation. For the same magnitude of current and deposition duration, the amount of charge used for metal plating increases correspondingly, resulting in increased deposited mass. The average wall thickness also increases significantly due to the increased metal deposition. The Sn content of Dep1 is much higher than Dep2. When the acid concentration decreases, the reaction overpotential increases (Figure 2.7), which favors the Ni deposition over the Sn deposition since the reduction potential of Ni (-0.26V vs. SHE) is lower than that of Sn (-0.13V vs. SHE). With a decreased Sn content, the cycle life of the electrode may be improved at the sacrifice of the energy density, as the Ni is electrochemically inactive but serves as a buffering component to alleviate volumetric expansion issues from Sn.

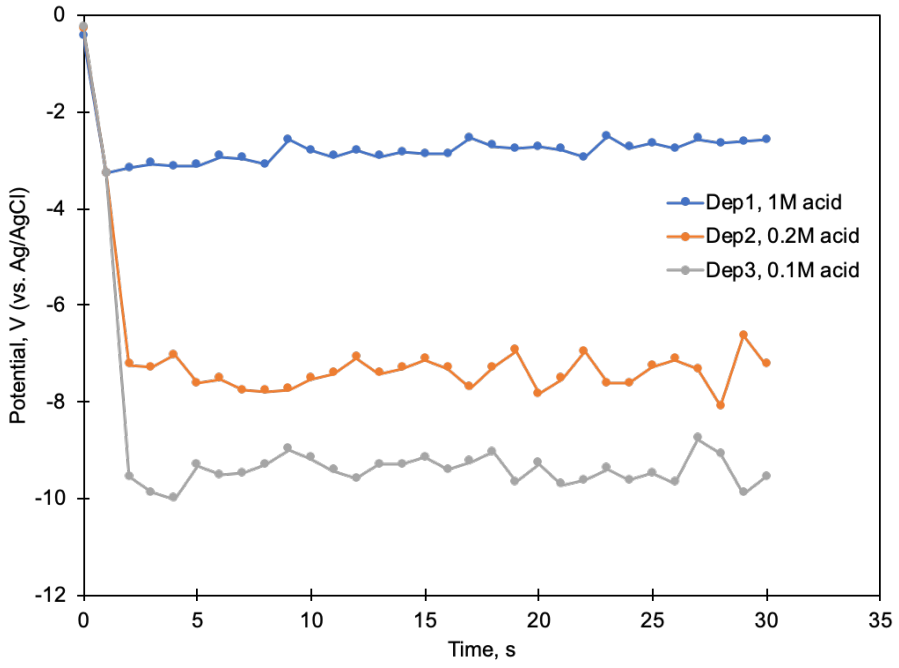

Figure 2. 7: Potential profile for porous NiSn plating with different acid concentration

Figure 2.8 shows the SEM images of porous NiSn deposited with different acid concentration baths. In comparison with Dep1, large protrusions similar to dendrites with heights over 100 μm can be observed in Dep2, which has a reduced amount (i.e. 0.2M) of H_2SO_4 in bath. Dendrite growth has been a persistent issue for metal plating, and it is rooted in the mass transport of the metal cations [16]. As shown in Figure 2.9 (a), when the solution ionic conductivity is low, as is in the case of Dep2, the metal cation concentration will be depleted in the vicinity of the electrode surface since slow ion diffusion cannot replenish the cations after being consumed. Hence, a strong concentration gradient is formed, and the metal dendrites propagate into bulk electrolyte where more cations are available. The metal protrusions also experience higher current densities, which self-accelerates the dendrite growth [16]. Moreover, the relatively irregular, uneven

porous electrode surface would make the uneven electrical field distribution even worse, leading to even more dendrite formation. Thus, when the ion concentration is high, as in the case of Dep1 (Figure 2.8 (a)) and Dep10 (Figure 2.8 (d)), there is no protrusion/dendrite formation.

A smaller current density also helps to alleviate the dendrite formation issue. When a high current is applied, the diffusion rate of metal ions in the electrolyte becomes relatively slow compared to their rate of consumption [16]. Strong concentration gradients are easily established, which leads to dendrite formation. As can be seen in the SEM image for Dep11 (Figure 2.8 (e)), even with the presence of 0.2M H_2SO_4, when the current density is decreased to 1A/cm^2, no obvious dendrite formation is observed.

At even lower acid concentration such as 0.1M H_2SO_4, a well-defined 3D-foam structure was no longer created as a result of insufficient amount of H_2 bubbles. Thus, this reduced acid concentration is undesirable for 3D porous electrode formation.

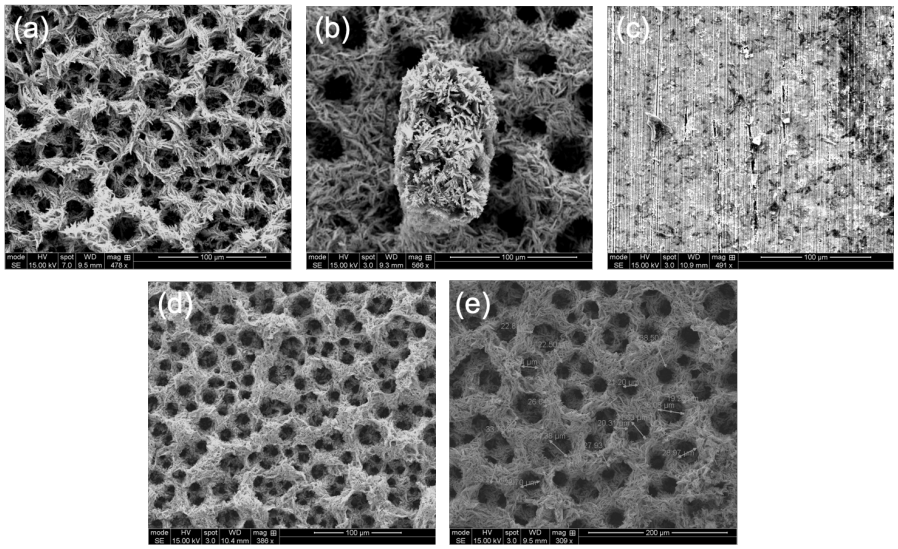

Figure 2. 8**:** SEM images of (a) Dep 1 (b) Dep 2 (c) Dep 3 (d) Dep 10 (e) Dep 11

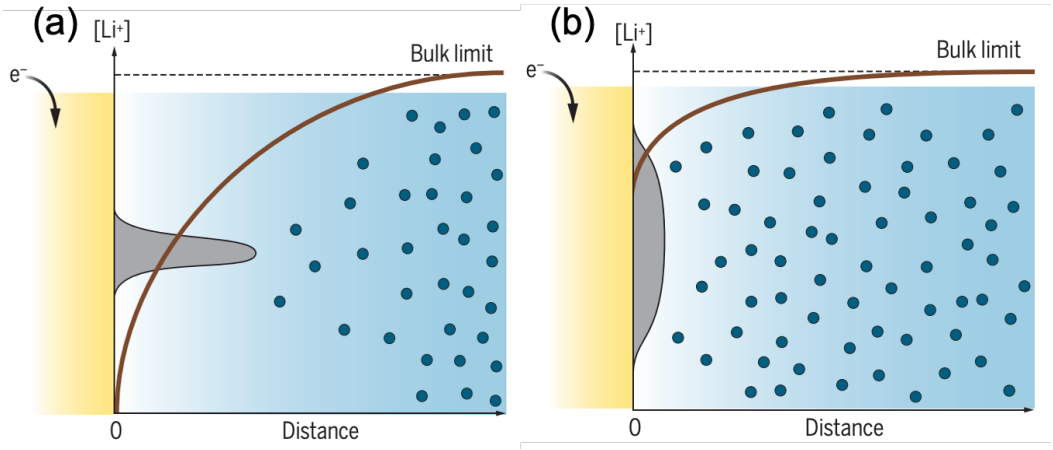

Figure 2. 9**:** Graphical illustrations of metal deposition and dendrite growth under (a) strong concentration gradient (b) mild concentration gradient [16]

2.2.2. Effect of pulse plating

Pulse plating involves the alternation of the potential or current between two different values, resulting in a series of pulses of equal amplitude, duration and polarity, separated

by zero current [17]. By changing the on/off ratio of the current, the composition and morphology of the deposit may be tuned. In addition, pulse plating allows ions to diffuse to the electrode surface during open circuit period, thus alleviating the mass transfer issues during high current electrodeposition. In this section, the effect of pulse ratio on the electrode deposition was explored.

Figure 2.10 shows the potential profile for plating using different pulse ratios. For pulse plating, the potential was consistently more cathodic compared to that for the continuous case (i.e. no pulse). A possible explanation is that the open circuit period always keeps the next current application period in the nucleation stage for both metal and bubble growth, which usually requires a larger overpotential and only lasts for 1s in our case. As a result of this larger overpotential compared to the continuous case (Dep1), Dep 4-6 had lower Sn ratios.

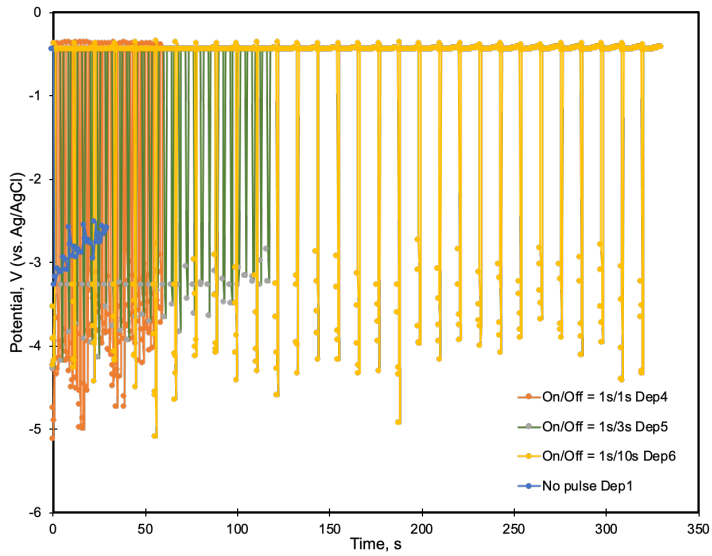

Figure 2. 10**:** Potential profile for porous NiSn plating with different pulse ratio at 2A/cm^2

Regarding the electrode morphology, since the growth mainly stayed within nucleation stage, it became increasingly diffult to form a well-ordered porous 3D structure as open circuit potential duration increased (Figure 2.11). Table 2.2 also confirmed the decreasing trend for both pore size and wall thickness.

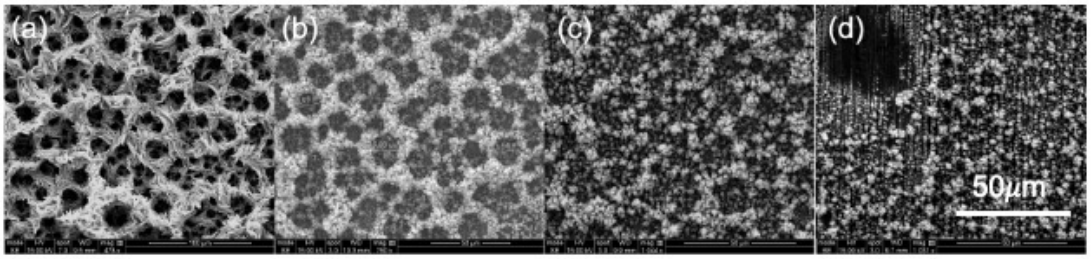

Figure 2. 11**:** SEM images of porous NiSn morphology (a) Dep1 (No pulse) (b) Dep4 (On/off = 1s:1s) (c) Dep5 (On/off = 1s:3s) (d) Dep6 (On/off = 1s:10s)

2.2.3. Effect of salt concentration

Control of the electrode composition may be achieved by changing the bath composition. Comparing Dep1 and Dep9, when the Sn salt concentration is reduced from 0.02M to 0.015M, a drop in Sn atomic ratio in the electrode is observed from 0.68 to 0.57. In comparison, when the Sn salt concentration is increased from 0.02M to 0.04M (Dep7 and Dep8), a corresponding increase in Sn atomic ratio from 0.4 to 0.68 is observed. Note that these two groups, namely Dep7/8 and Dep1/9, have different acid concentration.

In addition, a salt increase in the bath will also result in higher deposit mass, as seen from comparison between Dep1 and Dep10. This is again because the deposition process involves the competition between hydrogen gas evolution and metal deposition. Therefore,

as the salt concentration increases, the share of charge for metal deposition will become larger for the same total applied charge.

2.3. Porous gold

In addition to battery applications, hydrogen-templated electrodeposition method may also be utilized to prepare porous noble metal such as Au or Pt for sensing or electrocatalysis applications [18]. However, previous work demonstrated that the electrodeposition of such noble metal foams was difficult, due to the high activity of hydrogen evolution on the deposited material [18]. An alternative method to prepare a porous noble metal foam is through galvanic replacement, which involves the immersion of a low electrochemical potential porous metal, e.g. Cu or NiSn, into an aqueous bath that contains the target metallic salt with high electrochemical potential, e.g. Au. The process is driven by the potential difference between the redox species, with oxidation of the template/sacrificial metal (e.g. Cu or NiSn) as one half reaction and reduction (deposition) of the noble metal (e.g. Au) as the other half reaction.

In this study, we performed a proof-of-concept study on the generation of highly scalable porous Au on the mm scale. First, porous NiSn was fabricated using Bath 3 in Table 2.1 (0.4M $NiCl_2$, 0.04M $SnCl_2$, and 1M H_2SO_4), which has been shown to yield uniform porous deposit without any dendrite formation, and a 3A/cm^2 cathodic current was applied for 10 min for creation of mm level structure. The created porous electrode was then immersed in a commercial Au plating bath for approximately 12 hours. The galvanic replacement reaction proceeds as follows:

$$3Ni + 2Au^{3+} \leftrightarrow 3Ni^{2+} + 2Au \quad (5)$$

$$3Sn + 2Au^{3+} \leftrightarrow 3Sn^{2+} + 2Au \quad (6)$$

$$3Cu + 2Au^{3+} \leftrightarrow 3Cu^{2+} + 2Au \quad (7)$$

Figure 2.12 shows the clear contrast before and after the immersion, where the yellow color in 2.12 (b) indicates the conversion of NiSn to Au. Note that part of the sample in 2.12 (b) was scraped off to check efficiency of the conversion at bottom part of the sample. Although there was still some dark color indicating presence of NiSn residuals, most of the original deposit was converted, as confirmed by EDX results in Table 2.3. SEM images in Figure 2.13 shows a hierarchically porous structure, with nanometer scale fine features on the deposited walls, which is ideal for sensing and catalysis applications.

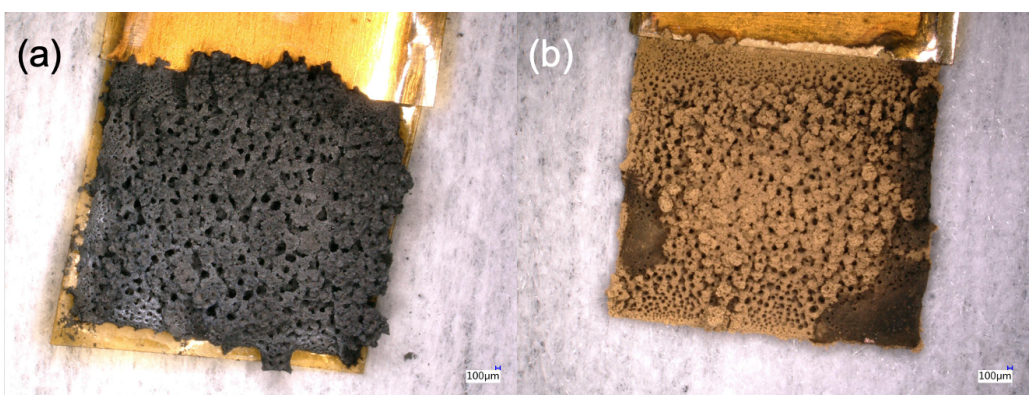

Figure 2. 12**:** Microscope image of porous NiSn (a) before and (b) after immersion in commercial gold plating bath

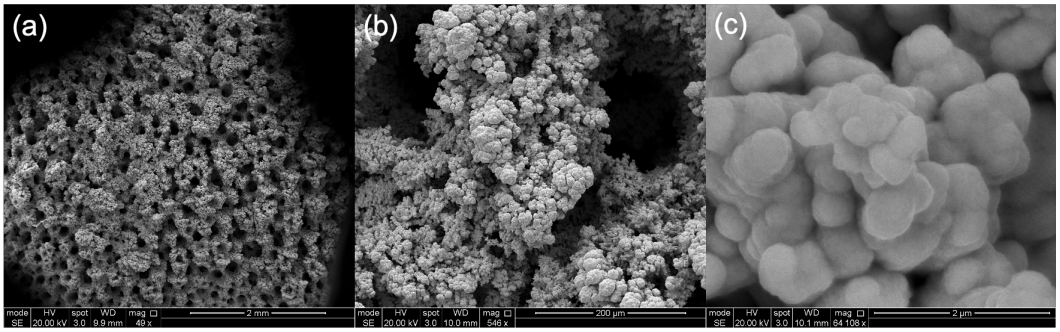

Figure 2. 13**:** SEM image of porous NiSn after immersion in gold plating bath at different magnifications

Element	Weight %	Atomic %
Ni	0.85	2.74
Cu	0.74	2.21
Au	98.42	95.05

Table 2. 3**:** EDX composition analysis of porous NiSn after immersion in gold plating bath

2.4. Conclusions

In this chapter, a hydrogen-templated electrodeposition method for scalable fabrication of porous, high surface area Cu, NiSn, and Au was demonstrated. This method is low cost, facile, and efficient, allowing access to porous morphologies without the use of an additional organic or inorganic template. In these porous structures, the pore size increases along the z-direction due to coalescence of the hydrogen bubbles, which forms a favorable porosity profile for battery applications. The tallest structures that were fabricated ranged from 100 μm to over 1 mm. Wall structures exhibit nanometer scale features that enlarged the surface area. In addition, the use of laser-machined holes reduced structural tortuosity and may facilitate future processes. The effect of various deposition conditions, such as bath concentration, current density, and pulse plating, was investigated, demonstrated the compositional and structural features of the porous NiSn can be tuned electrochemically.

Finally, the creation of scalable porous Au through galvanic replacement was demonstrated, representing an improvement over a direct plating process.

Future studies may examine the effect of substrate choice. For example, Najdovski and O'Mullane [10] showed that smaller pores for porous copper were produced on Au substrates compared with Cu, owing to the higher hydrogen evolution activity on the evaporated Au film, while depositions on Pd and glassy carbon did not form the same well-ordered structures. Although we briefly touched on use of acetic acid as an additive for pore size control, a range of other shape directing agents have also been reported to successfully adjust the nanostructured and/or microporous morphology of samples prepared by the hydrogen-templated electrodeposition [9].

Applications of these structures including battery current collectors or direct usage as battery electrode will be discussed in Chapter 3 and 4.

2.5. Reference

1. Min, H. S., Park, B. Y., Taherabadi, L., Wang, C., Yeh, Y., Zaouk, R., ... & Dunn, B. (2008). Fabrication and properties of a carbon/polypyrrole three-dimensional microbattery. *Journal of Power Sources*, *178*(2), 795-800.
2. Pikul, J. H., Zhang, H. G., Cho, J., Braun, P. V., & King, W. P. (2013). High-power lithium ion microbatteries from interdigitated three-dimensional bicontinuous nanoporous electrodes. *Nature communications*, *4*(1), 1-5.
3. Nathan, M., Golodnitsky, D., Yufit, V., Strauss, E., Ripenbein, T., Shechtman, I., ... & Peled, E. (2005). Three-dimensional thin-film Li-ion microbatteries for autonomous MEMS. *Journal of microelectromechanical systems*, *14*(5), 879-885.
4. Pearse, A., Schmitt, T., Sahadeo, E., Stewart, D. M., Kozen, A., Gerasopoulos, K., ... & Gregorczyk, K. E. (2018). Three-dimensional solid-state lithium-ion batteries fabricated by conformal vapor-phase chemistry. *ACS nano*, *12*(5), 4286-4294.
5. Kotobuki, M., Suzuki, Y., Munakata, H., Kanamura, K., Sato, Y., Yamamoto, K., & Yoshida, T. (2011). Effect of sol composition on solid electrode/solid electrolyte interface for all-solid-state lithium ion battery. *Electrochimica Acta*, *56*(3), 1023-1029.
6. Li, W., Liu, J., & Zhao, D. (2016). Mesoporous materials for energy conversion and storage devices. *Nature Reviews Materials*, *1*(6), 1-17.
7. Shin, H. C., Dong, J., & Liu, M. (2003). Nanoporous structures prepared by an electrochemical deposition process. *Advanced Materials*, *15*(19), 1610-1614.
8. Shin, H. C., & Liu, M. (2004). Copper foam structures with highly porous nanostructured walls. *Chemistry of materials*, *16*(25), 5460-5464.
9. Plowman, B. J., Jones, L. A., & Bhargava, S. K. (2015). Building with bubbles: the formation of high surface area honeycomb-like films via hydrogen bubble templated electrodeposition. *Chemical Communications*, *51*(21), 4331-4346.
10. Najdovski, I., & O'Mullane, A. P. (2014). The effect of electrode material on the electrochemical formation of porous copper surfaces using hydrogen bubble templating. *Journal of Electroanalytical Chemistry*, *722*, 95-101.

11. Fleury, V. (1997). Branched fractal patterns in non-equilibrium electrochemical deposition from oscillatory nucleation and growth. *Nature*, *390*(6656), 145-148.
12. Fundamental Aspects of metallurgy Szekely, J. (1989). The fundamental aspects of injection metallurgy. In *Ladle Metallurgy* (pp. 27-72). Springer, New York, NY.
13. Craig, V. S., Ninham, B. W., & Pashley, R. M. (1993). The effect of electrolytes on bubble coalescence in water. *The Journal of Physical Chemistry*, *97*(39), 10192-10197.
14. Shin, H. C., & Liu, M. (2005). Three-dimensional porous copper–tin alloy electrodes for rechargeable lithium batteries. *Advanced Functional Materials*, *15*(4), 582-586.
15. Courtney, I. A., & Dahn, J. R. (1997). Electrochemical and in situ X-ray diffraction studies of the reaction of lithium with tin oxide composites. *Journal of the Electrochemical Society*, *144*(6), 2045.
16. Xiao, J. (2019). How lithium dendrites form in liquid batteries. *Science*, *366*(6464), 426-427.
17. Wikipedia. (2020). *Electroplating*. Retrieved from: https://en.wikipedia.org/wiki/Electroplating#Pulse_electroplating_or_pulse_electrodeposition_(PED)
18. Li, Y., Song, Y. Y., Yang, C., & Xia, X. H. (2007). Hydrogen bubble dynamic template synthesis of porous gold for nonenzymatic electrochemical detection of glucose. *Electrochemistry Communications*, *9*(5), 981-988.

CHAPTER 3: FABRICATION OF LI-ION MICRO-BATTERIES USING POROUS COPPER AS SCAFFOLDS

In the previous chapter, facile and scalable fabrication of porous metal structures is described. In this chapter, the fabrication procedure for high areal capacity Li-ion micro-batteries using porous copper electrodes as scaffolds will be elaborated. A secondary metal coating is deposited on the porous copper to increase the mechanical rigidity without sacrificing surface area and porosity of the electrode. Then active materials are deposited electrochemically. Owing to sufficient porosity, low tortuosity, and scalability of the electrodes, high areal capacity can be achieved. In addition, a gel electrolyte is used to increase electrolyte retention compared to traditional polymer separators. The fabrication scheme is shown in Figure 3.1 below:

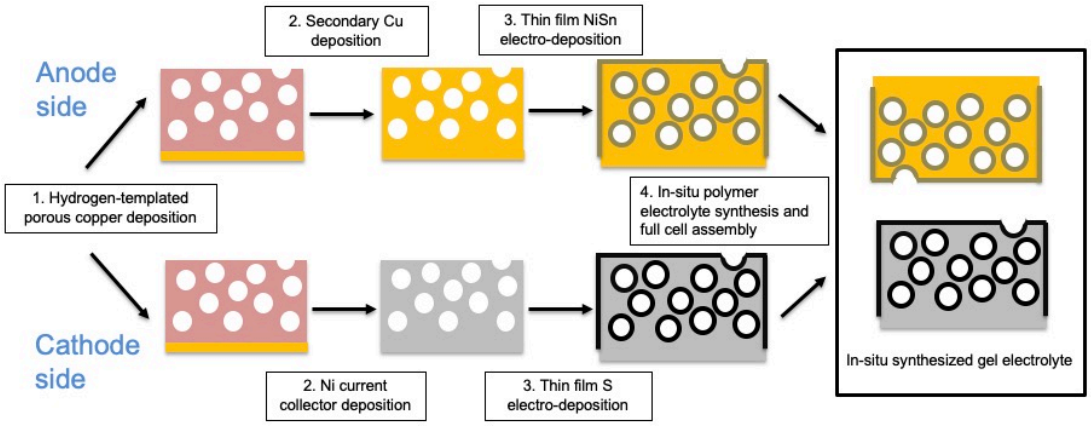

Figure 3. 1**:** Fabrication sequence of Li-ion micro-batteries using porous copper as scaffold

In this fabrication scheme, two porous copper electrodes are first prepared via hydrogen-templated electrodeposition as described in Chapter 2 as current collectors for cathode and

anode sides respectively. Specifically, Cu substrates are immersed in the electrochemical plating bath composed of 0.4M $CuSO_4$ and 1.5M H_2SO_4. A 5A/cm^2 cathodic current is applied to the Cu substrates for 15 minutes, using a Pt counter electrode. Then, a secondary layer of metal deposition was performed, with Ni deposited on the cathode side and Cu on the anode side. This secondary metal layer not only enhances the mechanical rigidity of the previous fragile porous structure, but further strengthens the connection between loose dendritic contacts as well. Thin films of NiSn and sulfur are then subsequently electrodeposited onto the anode and cathode current collectors, respectively. Limiting the thickness of the deposition enables stable cycling of these high-volume expansion materials. Subsequently, a liquid electrolyte precursor containing conventional carbonate electrolyte, acrylate monomer, and heat initiator azobisisobutyronitrile (AIBN), is injected into a package that contains both the cathode and the anode, followed by heat-initiated polymerization. In opposition to the conventional approach of infiltrating viscous gel into a porous structure, the gel polymer electrolyte is synthesized in-situ to ensure good electrode/electrolyte contact. The fabrication steps and electrochemical testing results will be discussed in detail in this chapter.

3.1. Secondary metal deposition

Hydrogen-templated electrodeposition has been utilized to create porous electrodes for various applications such as energy storage [1], catalysis [2], and sensing [3]. However, one major disadvantage associated with the electrodes prepared by this technique is that they are mechanically fragile due to weak electrode adhesion to the substrate [4-5]. Additionally, as shown in Figure 3.2, there is insufficient connections among dendritic

micro/nano-features, which may impair both mechanical strength and electrical conduction. Insufficient mechanical rigidity of the electrodes makes packaging inconvenient and breaking of the structure may lead to internal shorting [4]. Thus, it is important to strengthen the electrode structure mechanically. To achieve this goal, an additional layer of metal is electroplated onto the existing porous Cu, with Ni deposited on the cathode side porous copper and Cu on the anode side.

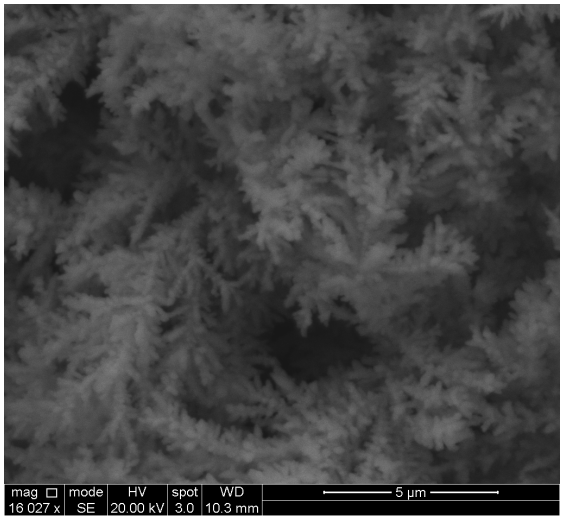

Figure 3. 2**:** Dendritic porous copper walls from hydrogen-templated electrodeposition

3.1.1. Secondary copper plating

The goal of the secondary copper plating is to enhance the overall mechanical rigidity and the electrical connection among the dendrites. However, if too much secondary copper is plated, the pores will be blocked, and there will be insufficient porosity for electrolyte penetration during subsequent active material deposition and battery testing. In addition, a rough surface, in comparison with a completely smooth one by over-plating of secondary

copper, has an increased surface area and reduced interfacial resistance for electrochemical reactions. Thus, the conditions of secondary Cu plating need to be optimized for both mechanical rigidity and electrochemical performance. In a secondary copper plating process, porous copper is first dipped in isopropyl alcohol (IPA) and then immersed in 1:4 hydrochloric acid (HCl) solution for an hour to etch away any surface oxides. Then the sample is cleaned in DI water and placed in a stirring copper plating bath (See Table 3.1 for composition of the copper plating bath). Figure 3.3 (b) shows the sample after 3 hours of continuous potentiostatic plating at -0.2V versus a Cu foil counter electrode. As shown, after the copper plating, pores at top of the sample are significantly narrowed in size due to over-plating. This over-plating on the surface restricts flow of electrolyte and results in under-plating of copper at bottom part of the electrode, which in turn causes insufficient contact between the porous copper and the underlying copper substrate, sacrificing overall mechanical rigidity. In addition, this geometry is undesirable for battery performance in terms of ion transport. Thus, new processes need to be devised for the secondary copper plating.

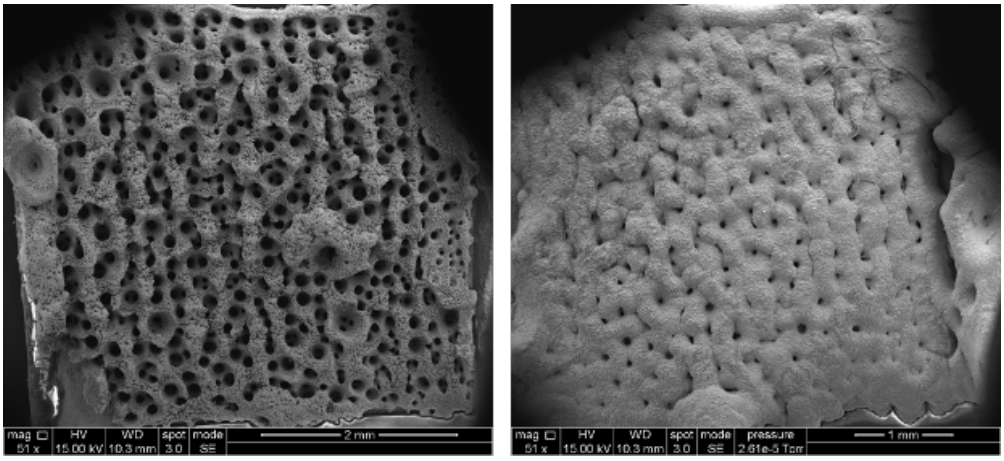

Figure 3. 3**:** (a) Before (b) After secondary copper plating for 3hrs at -0.2V vs. Cu counter electrode

Compounds	Mass/Volume
$CuSO_4.5H_2O$	200g
H_2SO_4 (95 – 98%)	25mL
DI water	1L

Table 3. 1**:** Bath composition for secondary Cu plating bath (Note: total bath volume equals 1L)

Conformal electrochemical deposition onto high aspect ratio three-dimensional structures has been challenging [6]. Specifically, for 3D porous media, mass transfer resistance along the electrode thickness direction results in potential drops in the liquid electrolyte phase and causes the deposition of materials to occur preferentially at the electrode top near the bulk electrolyte. In addition, similar to the time delay in transmission lines, it takes a longer time for the bottom portion of the electrode to reach the steady state reaction rate than the top, further increasing the deposition rate discrepancy across the thickness of the electrode, resulting in non-conformal depositions [7]. Although pulse plating may allow metal salt ions to diffuse and be replenished at the bottom of the electrode, as seen in Figure 3.4, it may still be insufficient to provide a uniform coating since the driving force for plating is inherently higher near the top of the electrode due to the liquid potential drop. For the sample in Figure 3.4, pulse plating was applied with 80 mA/cm2 current density with 1s/4s on/off ratio for 1200 cycles.. However, as we can see from the image, morphologies at top and bottom parts of the electrode are very different due to inhomogeneous plating rates.

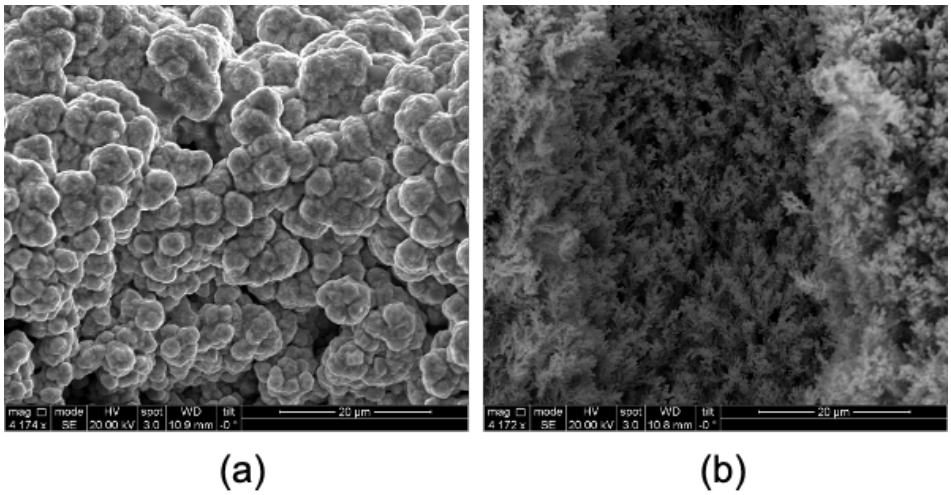

Figure 3. 4**:** SEM cross-section after the secondary copper plating: (a) Top part of the electrode (near bulk electrolyte) (b) Bottom part of the electrode (close to the substrate, away from the bulk electrolyte)

Thus, in this work, to achieve conformal plating, the porous copper was cycled between additive electrodeposition and subtractive stripping, as demonstrated by Pikul *et al* for deposition of MnO_2 [6]. Current and voltage profile is shown below for a typical cycle:

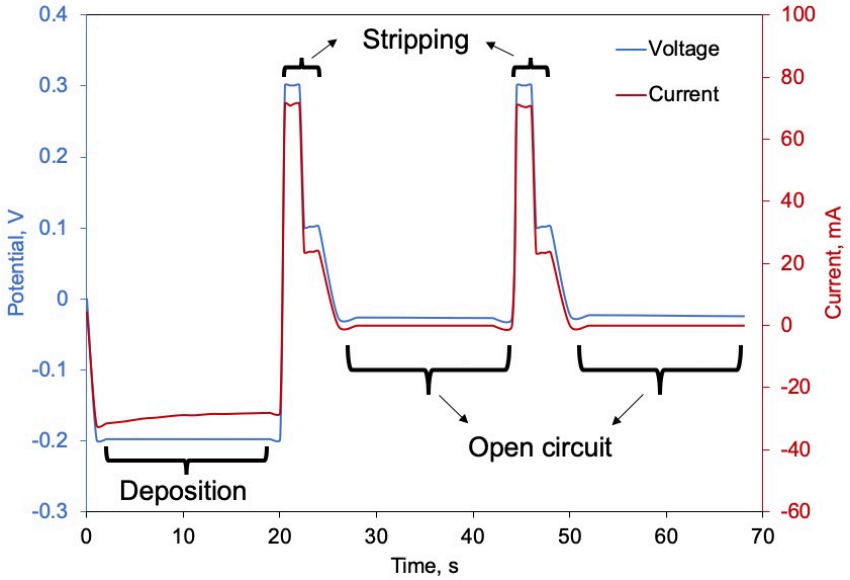

Figure 3. 5**:** One cycle of current and voltage profile for secondary copper plating

In this cycle, 20s of constant potential (-0.2V) is applied versus a Cu counter electrode to deposit the secondary copper. Then, 2 seconds of 0.3V reverse potential is applied to etch away over-deposits at the electrode surface. Due to the potential drop in the electrolyte phase, similar to deposition, stripping of materials also preferentially occurs at the electrode surface close to the bulk electrolyte. Specifically, 0.3V etch strips a large amount of deposits near the top electrode surface and reducing the etch voltage to 0.1V for the last 2 seconds reduces the amount of stripping in the electrode bulk and bottom layers. Here, two short stripping periods are separated by an open circuit period for two reasons: 1. To allow sufficient mass transfer of ions into the electrode bottom for the next deposition period; 2. To reset the liquid electrolyte potential to prevent over-etching in the middle and bottom of the electrode.

With such deposition/stripping protocols, the morphology of the electrode is much improved for electrolyte transport. As shown in Figure 3.6, sample (b) is continuously deposited for 3 hours and the surface pores are pinched close, whereas sample (a) is cycled between deposition and stripping cycles and has a cumulative deposition time of 3.5 hours in addition to stripping cycles as introduced earlier. With the stripping potentials applied, the surface pores are kept open and would facilitate electrolyte transport in future processes.

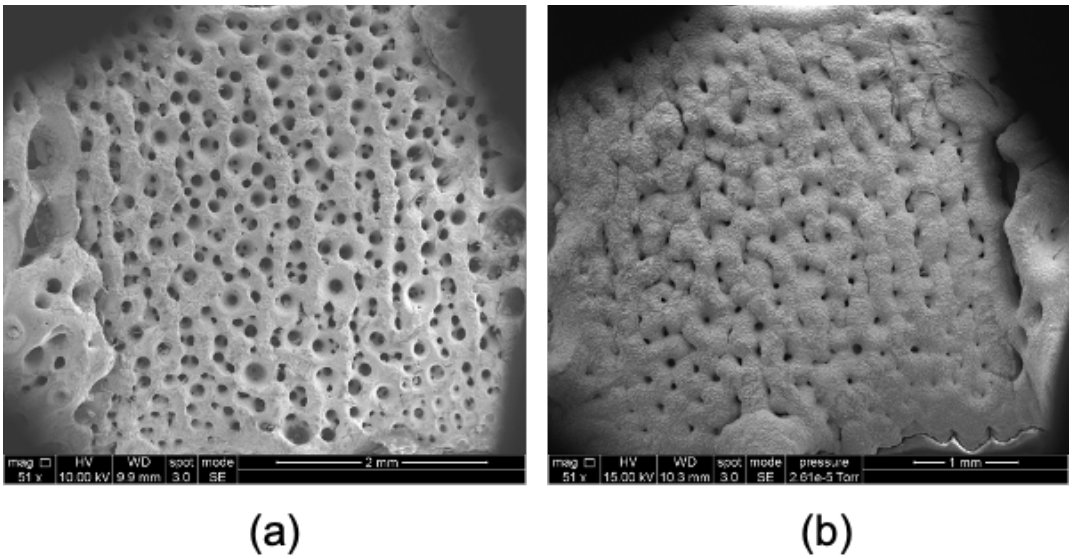

Figure 3. 6**:** Surface of porous copper after secondary copper plating (a) With deposition/stripping protocols (b) With continuous plating

In addition to maintaining sufficient porosity for transport, the deposition throughout the thickness direction of the electrode is also more conformal with the deposition and stripping cycles to maintain the structural rigidity. As shown in Figure 3.7, compared with Figure 3.4, there is more uniformity in the morphology between top (a) and bottom (b) part of the electrode, without over-deposition at the top.

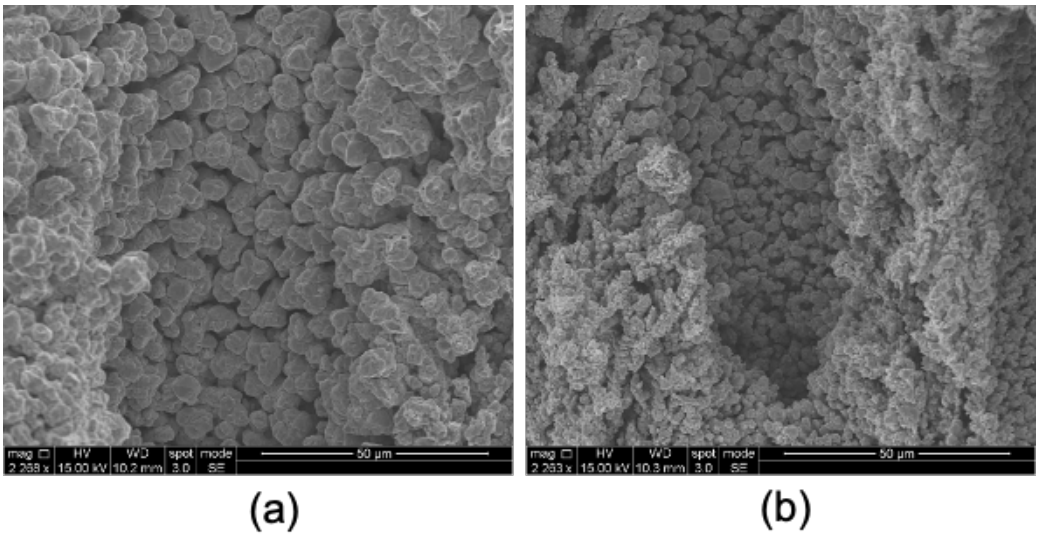

Figure 3. 7**:** Cross-section of porous copper after 2nd copper plating with deposition/stripping protocols (a) Top part of the electrode (b) Bottom part of the electrode

In order to further improve uniformity, a green laser is applied to drill holes on the copper substrate before the hydrogen-templated copper deposition (see chapter 2) such that the electrolyte can access the electrode surface from backside of the Cu substrate. This approach decreases by half the ion diffusion distance and reduces the overall charge and mass transport resistance. Figure 3.8 shows microscope images of the laser-machined copper substrates with different designs. For all three substrate samples in the microscope image, the hole area occupies 13% of the 0.5cm by 0.4cm active deposition area, and from left to right, samples have diameters of 400 μm, 200 μm, and 100 μm, respectively. Note that, when the diameter is decreased by half, the total number of holes quadruples to keep the total hole area the same.

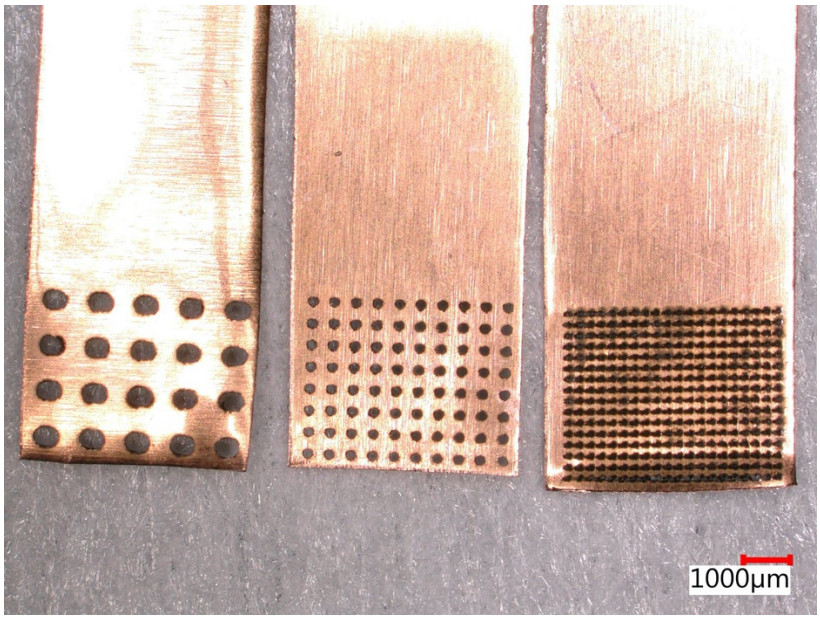

Figure 3. 8**:** Microscope image of copper substrate with varying pore diameter of 400 μm, 200 μm, and 100 μm

Figure 3.9 shows a sample after 200 deposition/stripping cycles using the protocol shown in Figure 3.5, using a copper substrate with 400 μm diameter laser-machined holes arranged in a 5 by 4 array on a 0.5 cm by 0.4 cm area. Compared with Figure 3.4 and 3.7, Cu morphology at the top and bottom of the electrode appears to be very similar, indicating conformal deposition.

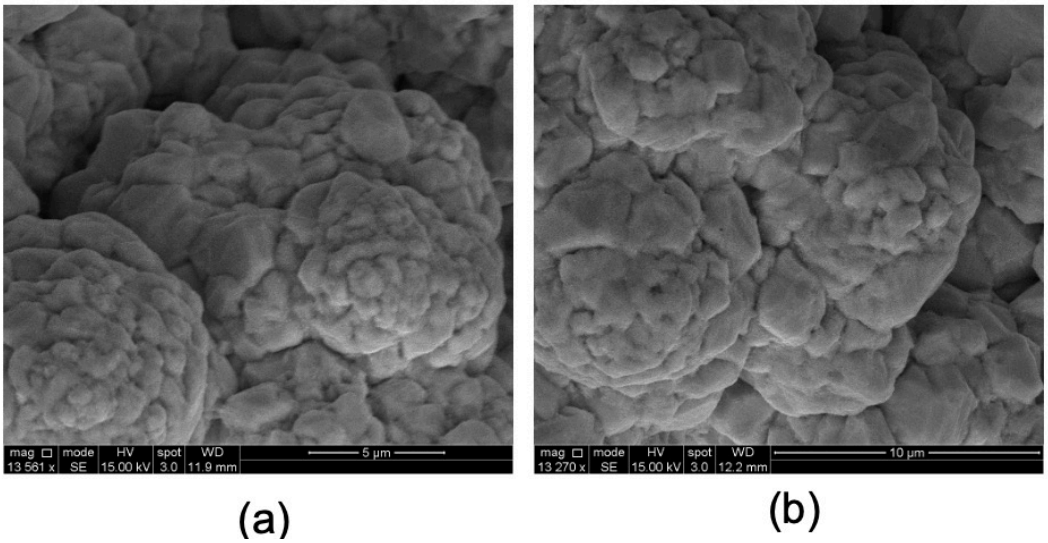

Figure 3. 9**:** Porous copper on a Cu substrate with 5 by 4 400 μm diameter holes after 2nd copper plating with deposition/stripping protocols (a) Top part of the electrode (b) Bottom part of the electrode

3.1.2. Nickel plating

Due to copper corrosion at 3V versus lithium metal, which is usually within the cathode operation window, aluminum or nickel is usually utilized as the cathode side current collector. In this study, nickel is chosen as the cathode side current collector since the plating protocol for nickel has been well established. Nickel plating is similar in principle to the secondary copper plating. In a typical deposition, porous copper is first dipped in IPA and then immersed in 1:4 hydrochloric acid (HCl) solution for about an hour to etch away any surface oxides. Then the sample is rinsed in DI water and placed in a stirring nickel plating bath (See Table 3.2 for composition of the nickel plating bath).

Compounds	Mass/Volume
$NiSO_4.6H_2O$	400g
H_3BO_3	40g
Saccharin	3g
DI water	1L

Table 3. 2**:** Bath composition for 2nd Ni plating bath (Note: total bath volume equals 1L)

Similar to the secondary copper plating, a combination of deposition/stripping sequences is utilized to ensure conformal coating. The deposition protocol for Ni plating is given below:

- -2.6V deposition vs. nickel counter electrode for 20s
- 1.3V stripping vs. nickel counter electrode for 2s
- 0.9V stripping vs. nickel counter electrode for 2s
- 20s open circuit voltage (OCV)
- 1.3V stripping vs. nickel counter electrode for 2s
- 0.9V stripping vs. nickel counter electrode for 2s
- 20s open circuit voltage (OCV)

Figure 3.10 shows the porous electrode before and after nickel plating. After nickel plating, the dendritic copper is covered with globular nickel, suggesting better mechanical rigidity after the deposition. In addition, the high surface area features are retained and micron-size pores remain open to allow electrolyte transport. Figure 3.11 shows a sample after 250 deposition/stripping cycles using the protocol described above, on a copper substrate

with 5 by 4 400 μm diameter laser-machined holes. The Ni morphology at the top and bottom surfaces of the electrode appeared to be very similar, indicating conformal deposition.

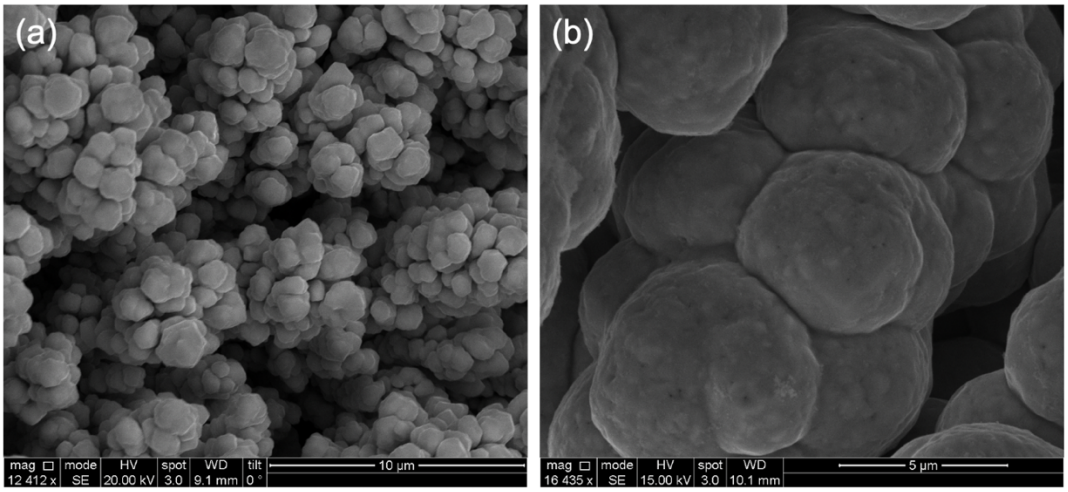

Figure 3. 10**:** (a) Porous copper before Ni plating (b) Porous copper after Ni plating

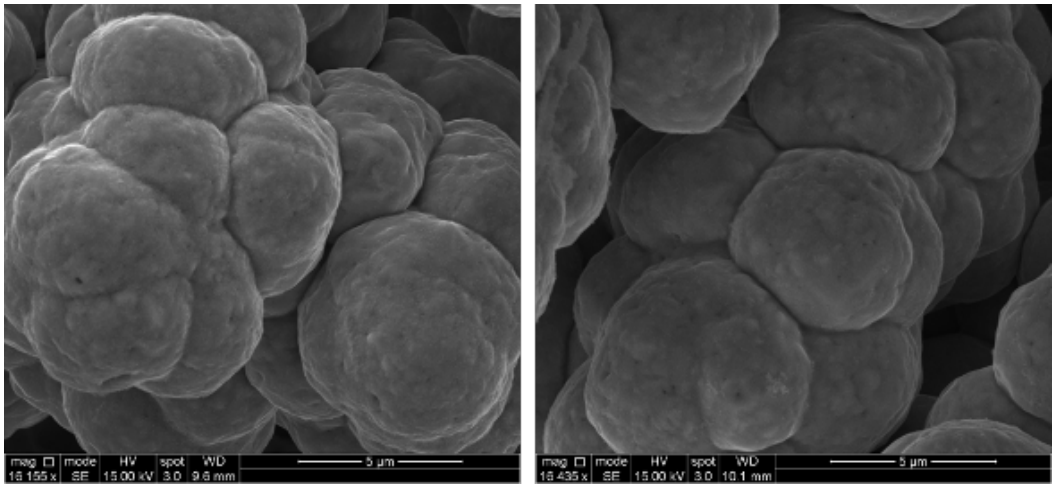

Figure 3. 11**:** Porous copper on a Cu substrate with 5 by 4 400 μm diameter holes after Ni plating with deposition/stripping protocols (a) Top part of the electrode (b) Bottom part of the electrode

3.2. Active material deposition

Following the secondary metal plating, active materials are electrochemically deposited, following a process that is compatible with microelectronic fabrication processes. Details of the deposition process are given below.

3.2.1. NiSn anode electrodeposition

NiSn is electroplated as the anode material. Tin has a high (990mAh/g); however, it suffers from severe capacity fading resulting mainly from its large volume expansion/contractions during lithiation/delithiation and subsequent pulverization and delamination from current collectors [8]. Alloying tin with inactive elements, such as nickel, can suppress the volume change during electrochemical cycling effectively without appreciable irreversible capacity loss [9]. Figure 3.12 shows the cycling performance comparison of NiSn and Sn thin film materials. It is evident that NiSn retains much more fraction of its initial capacity compared with Sn after 50 cycles of charge and discharge.

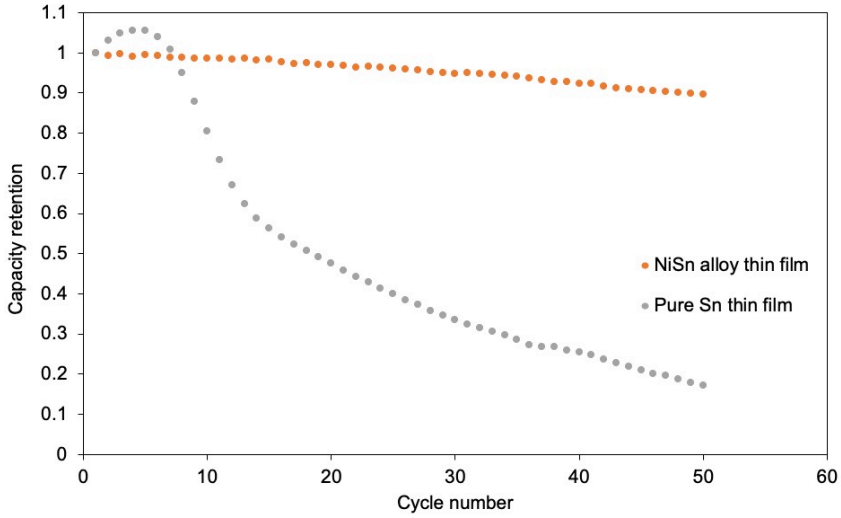

Figure 3. 12**:** Cycling performance comparison of NiSn and Sn thin films

In a typical NiSn deposition, the porous copper electrode with the seconday Cu deposition is briefly rinsed in IPA followed by one hour immersion in 1:4 HCl to remove surface oxides. Then the electrode is rinsed in DI water, dipped in IPA, and placed in the plating bath with a nickel counter electrode (See Table 3.3 below for the bath composition). Note that, due to differences in deposition potential between Ni^{2+} (-0.25V vs. SHE) and Sn^{2+} (-0.14V vs. SHE), additives like potassium pyrophosphate ($K_4P_2O_7$) and glycine ($C_2H_5NO_2$) are added to shift the deposition potentials of each metal to more negative direction [10]. Since such a potential shift in nickel is larger than that in tin, the deposition potentials of the corresponding metal become closer to each other.

Compounds	Mass/Volume
$NiCl_2.6H_2O$	9g
$SnCl_2.2H_2O$	19g
$K_4P_2O_7$	82g
$C_2H_5NO_2$	4.7g
Saturated NH_4OH	2.5 mL
DI water	500mL

Table 3. 3**:** Bath composition for NiSn alloy anode plating bath (Note: total bath volume equals 500mL)

The deposition protocol used for NiSn anode material is similar to those for Cu and Ni plating. A combination of deposition and stripping sequences, in addition to laser-machined holes on the Cu substrate, are utilized to ensure conformal plating on the 3D electrode.

- -1.2V deposition vs. nickel counter electrode for 40s
- 5 sub-cycles, within each:
    - 0.9V stripping vs. nickel counter electrode for 2.5s
    - 0.7V stripping vs. nickel counter electrode for 2.5s
    - 64s OCV

As shown in Figure 3.13, the similar NiSn morphology at top surface, bulk, and bottom surface of the electrode indicates uniform plating.

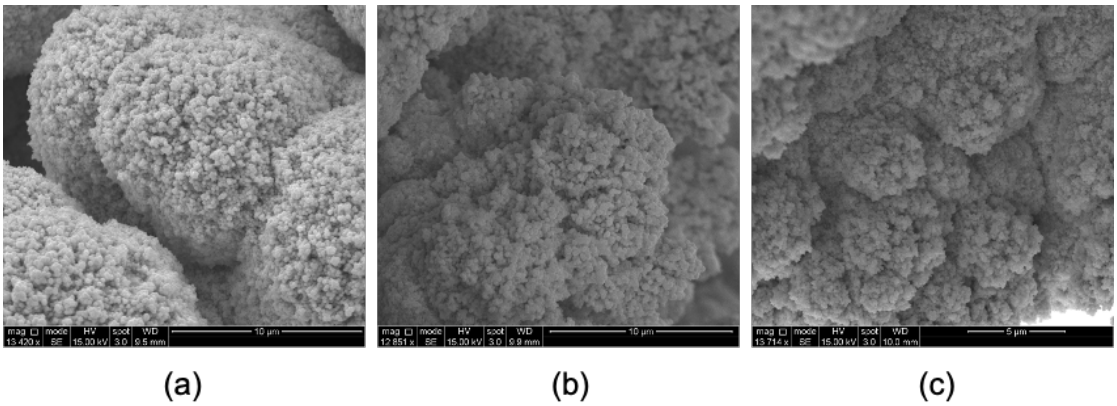

Figure 3. 13**:** Morphology of the electrode after NiSn deposition (with holes on the substrate) (a) Top part of the electrode (b) Middle part of the electrode (c) Bottom part of the electrode

3.2.2. Sulfur cathode electrodeposition

Due to high specific energy, low cost, and environmental friendliness, sulfur cathodes hold great promise to meet the increasing demand for advanced energy storage. As a light weight element, sulfur has a gravimetric capacity of 1672 $mAh.g^{-1}$, which is much higher than that of the commonly used insertion-type electrodes such as $LiCoO_2$ (142 $mAh.g^{-1}$),

$LiNi_{1/3}Co_{1/3}Mn_{1/3}O_2$ (195 mAh.g^{-1}), $LiFePO_4$ (178 mAh.g^{-1}) [11]. However, the electrochemical inertness of bulk sulfur, due to its poor electronic conductivity, sluggish kinetics, and incomplete electrochemical conversion, is one of the major problems yet to be resolved [12]. Conventionally, sulfur is melted, impregnated into nano-porous carbon materials, and mixed with conductive and binder materials [13]. This approach could enhance the electrode electronic conductivity and trap the polysulfides formed within nano-porous carbon during charge/discharge processes to improve cycle life of the electrode. In this study, a method developed by Zhao et al. [12] is adopted to electrodeposit S onto porous Ni or Cu current collector. This avoids the processing complexity involved with conventional cathode electrode preparation. Moreover, electrodeposition is also compatible with microfabrication processes.

The S cathode is prepared using potentiostatic deposition. Note that electrodes after either the secondary Cu or Ni deposition may be used as a cathode current collector substrate, and the electrochemical cycling performance of the two electrodes after S plating are compared in section 3.4.2. In a typical deposition process, the porous electrode after the secondary Cu or Ni deposition is dipped in IPA, followed by immersion in 1:4 HCl solution to remove any surface oxides. Then, the electrode is rinsed with DI water and immersed in the plating bath with a 0.1M sodium sulfide (Na_2S) aqueous solution. An anodic potential of 0.7V is applied on the electrode versus a 100 PPI, 80 μm thick nickel foam counter electrode. Electrons from S^{2-} ions are stripped, and sulfur is subsequently deposited onto the porous Ni electrode. The detailed half-cell reactions are described below:

Ni mesh cathode: $2H_2O + 2e^- \rightarrow H_2\uparrow + 2OH^-$

Porous Ni anode: $S^{2-} - 2e^- \rightarrow S$

Note that, although a constant potential or current is applied, a deposition/stripping protocol may also be devised for sulfur plating and result in more uniform deposition.

Figure 3.14 shows the SEM images for the porous Ni electrode before and after sulfur deposition, demonstrating that needle-shaped sulfur is deposited onto the porous nickel electrodes.

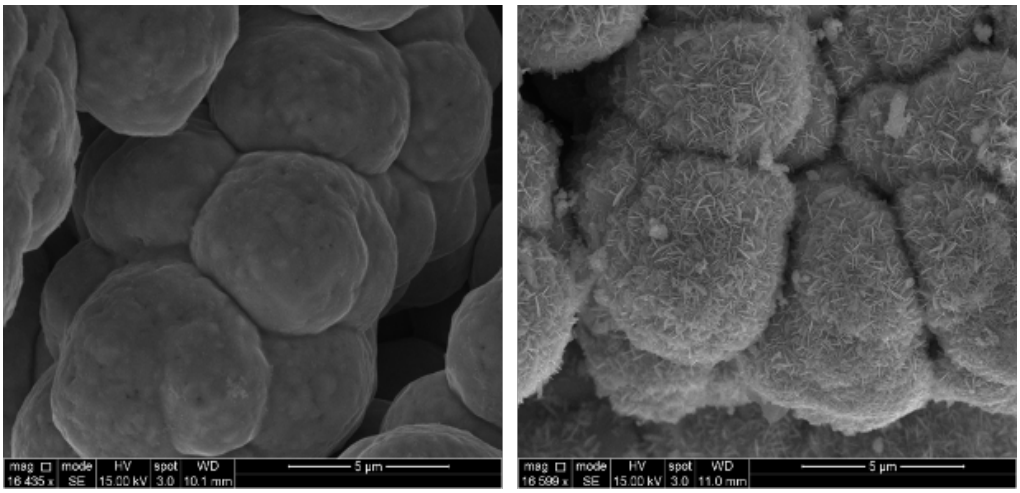

Figure 3. 14**:** Porous Ni electrode (a) before and (b) after sulfur plating

3.3. Gel electrolyte preparation

After both half-cell electrodes are prepared, the full cell is assembled using gel electrolyte. To date, the safety of Li-ion batteries has been a primary issue concerning their widespread use [14]. Combustible liquid electrolytes are the major cause of poor safety as they may leak from the battery and cause fire or explosion [15]. In sharp contrast, gel-polymer electrolyte are semi-solid organic compounds with good fire-resistant properties, poor

liquidity, and relatively good mechanical strength [16-17]. In addition, it has been reported that the three-dimensional framework of gel polymer electrolyte promotes the formation of a very tight protective film on the surface of the electrodes during cycling, therefore inhibiting the cyclable Li consumption due to side reaction with the electrolyte and retaining the structural integrity of the electrodes during battery cycling [16].

It is vital that the gel electrolyte has good contact with the electrode surface to fully utilize the capacity of the electrode. Conventionally, a viscous gel electrolyte is prefabricated and infiltrated into the porous electrode [18]. In most cases, the gel electrolyte can only infill part of the volume of the electrode. As a result, the capacity of such gel electrolyte-based electrodes does not scale with electrode thickness, usually saturating while the electrode is quite thin [18]. In order to circumvent this issue, a method to polymerize a precursor solution in situ via heat-initiated gelation is adopted [19]. The precursor solution is composed of 1.5 wt.% PETEA monomer (pentaerythritol tetraacrylate) and 0.1 wt.% azodiisobutyronitrile (AIBN) initiator dissolved in a liquid electrolyte. Depending on cell chemistry, the electrolyte can either be ether-based, e.g. 1M LiTFSI in dioxolane (DOL)/dimethoxymethane (DME) (1:1 by volume) with 1% $LiNO_3$ additive, or carbonate-based, e.g. 1M $LiPF_6$ in 1:1 ethylene carbonate (EC)/diethyl carbonate (DEC) (1:1 by volume). Upon heating at 70 ℃ for half an hour, a translucent gel is formed due to thermal decomposition of AIBN and the subsequent chain growth reaction of PETEA monomers (See Figure 3.15).

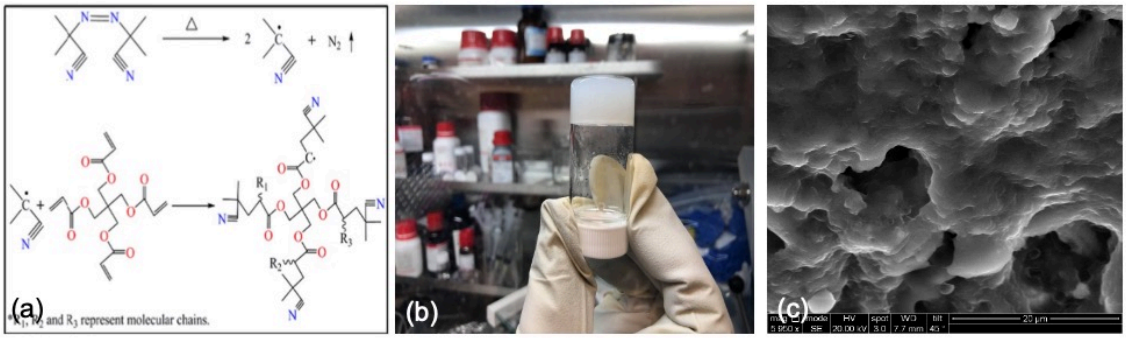

Figure 3. 15**:** (a) Polymerization mechanism of the PETEA monomers [19] (b) Gel polymer electrolyte after the gelation process (c) SEM image for gel electrolyte covering a porous NiSn electrode

3.4. Electrochemical performance testing – Half cells

The individual electrodes are characterized by charging and discharging to find out their capacity per footprint area in mAh/cm^2, power capability, and cycle life performance. Usually, the electrodes are cycled within a specified potential window to avoid undesirable side reactions on the electrodes. For example, the lower cut-off potential of NiSn anode is set to be no lower than 0.01V vs. Li to avoid the lithium plating reaction. A two-electrode or three-electrode configuration is utilized for these tests. In a two-electrode configuration, a Li foil is used as a counter electrode and acts as a source or sink for Li ions when the porous electrode is being lithiated or delithiated. A major drawback for two electrode tests is that Li has a very high interfacial charge transfer resistance. Thus, under high current densities, the Li side of the cell will have very large overpotential according to Butler-Volmer's equation. This causes the cell to reach the cut-off potential before the full capacity of the electrode is utilized. In order to circumvent this issue, a three electrode tests can be used. In a three-electrode test, a second piece of lithium is used as a reference, and the potential of the high areal capacity electrode is measured against it. Since the

current only passes through the working and the counter electrode, and not through the reference electrode, the cell voltage only records the overpotential from the working electrode and does not include that from the Li counter electrode, allowing the working electrode to fully utilize its capacity.

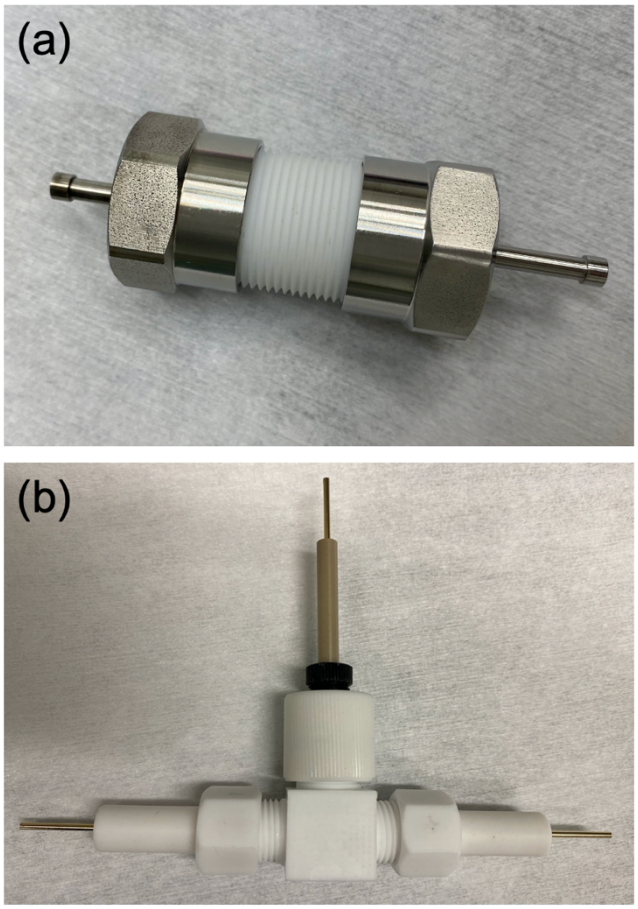

Figure 3. 16**:** Testing cell configurations (a) Swagelok for two-electrode testing (b) Three electrode set-up

For terminology purposes, for all half-cell tests (including two electrode and three electrode tests), the cell defined as charged when the cell potential increases and the cell is discharged when the cell potential decreases.

3.4.1. NiSn anode

The electrochemical process for NiSn intermetallic lithiation is expected to evolve by a first activation step:

$$NiSn + 4.4Li^{+} + 4.4e^{-} \rightarrow Li_{4.4}Sn + Ni$$

followed by the main, reversible electrochemical process [20]:

$$Sn + 4.4Li^{+} + 4.4e^{-} \leftrightarrow Li_{4.4}Sn$$

The capacity retention of the NiSn intermetallic electrode, although improved with respect to that of plain Sn electrodes as shown in Figure 3.12, is not totally satisfactory due to the significant volume expansion/contraction during the cycling process [20] that has two detrimental effects. First, the active materials pulverize upon stress and detach from the conductive network, resulting in capacity loss. Second, the Sn particles crack causes increased interfacial contact area between fresh Sn surface and the electrolyte. This results in continuous electrolyte decomposition and the formation of the solid electrolyte interphase (SEI) that consumes Li-ions [21]. This is the major capacity loss mechanism for a system with a limited inventory of Li-ions. The use of chemical additives is hailed as the most effective, economic and scalable approach to realize alloy-type anodes such as Si and Sn [22]. It has been reported that additives such as fluoroethylene carbonate (FEC) and vinylene carbonate improve the performance of Sn-based electrodes [21-26] due to the formation of more stable SEI that sufficiently limits the emergence of large cracks,

preserves the original morphology [25], and inhibites further electrolyte decomposition, in comparison with the pure EC-based electrolyte [21].

Electrochemical cycling of thin film NiSn in a two-electrode configuration using Li metal foil as the Li source is performed as a model system to study the effect of the FEC electrolyte additive. Thin film NiSn is prepared by applying a 5mA/cm^2 cathodic current to a copper substrate with the bath described in Table 3.3. The baseline electrolyte used for electrochemical cycling is 1M $LiPF_6$ in 1:1 EC/DEC (v/v) purchased from Gotion, Inc, and 5% FEC is added for comparison. Figure 3.17 (a) shows an improved capacity retention for the sample cycled with 5% FEC electrolyte. In addition, the sample with a 5% FEC exhibited superior Coulombic efficiency (Figure 3.17 (b)), which is the ratio between delithiation and lithiation capacities. Since parasitic reactions between the electrode and electrolyte occur during lithiation, this indicates the SEI formed with 5% FEC electrolyte more effectively passivated the electrode surface. Energy dispersive x-ray spectroscopy (EDX) indicates a four atomic percent of fluoride content on the electrode surface cycled with 5% FEC, while no fluoride signal is observed for the baseline electrolyte. This is consistent with results reported previously in literature showing that inorganic LiF forms in the SEI layers when the electrodes are cycled with FEC-based electrolytes, which more effectively inhibit further electrolyte decomposition reactions at the interface [21][26].

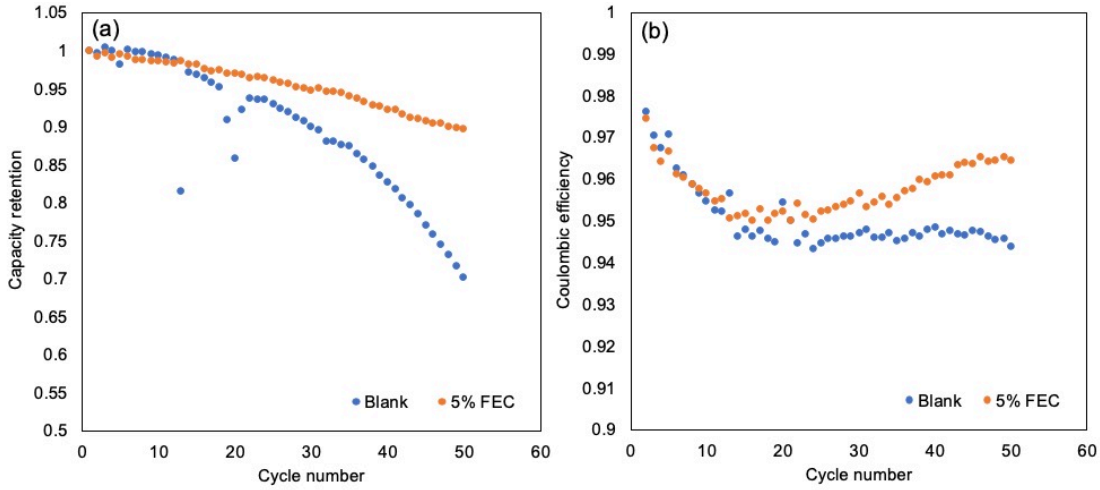

Figure 3. 17**:** Thin film NiSn cycling experiment with and without 5% FEC additive (a) Capacity retention (b) Coulombic efficiency

In order to further demonstrate the efficacy of additives in inhibiting the electrolyte decomposition reactions, symmetric cell tests of NiSn thin films are conducted. Symmetric cells are assembled using two identical electrodes, one previously lithiated and the other delithiated [27]. This arrangement allows a limited supply of lithium to be transferred between the two electrodes during cycling. Without the presence of excess lithium, such as the lithium foil in a half cell, any parasitic reactions that consume lithium result in capacity loss during cycling similar to a full cell [27]. In the test, per symmetric cell, two thin film NiSn electrodes are prepared to lithiated/delithiated states respectively in a half-cell configuration. Then individual electrodes are harvested from the half cells, assembled into a symmetric cell, and cycled with three different electrolytes, as illustrated in Figure 3.18 below. Note that the baseline electrolyte is 1M $LiPF_6$ in 1:1 EC/DEC (v/v). The sample cycled using 10% FEC + 1%VC electrolyte results in the best capacity retention performance.

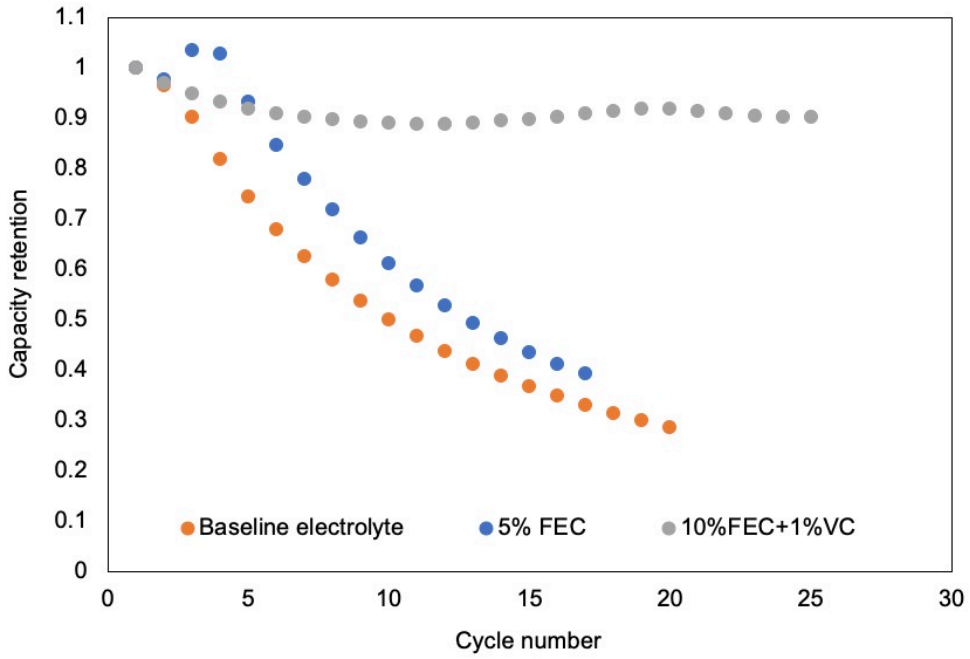

Figure 3. 18**:** Thin film NiSn symmetric cell cycling in different electrolytes

After the electrolyte composition is optimized, the capacity performance of NiSn deposited on 3D porous Cu and on a Cu substrate is compared in Figure 3.19 to demonstrate the advantage of utilizing a 3D electrode. Note that both samples are deposited under identical conditions as shown in section 3.2.1 for 60 cycles. NiSn deposited on porous Cu exhibited capacity 9 - 10 times higher than that on a planar Cu. The higher capacity is attributed to the high surface area and the z-direction scalability of the porous Cu that allows more NiSn active material to be deposited.

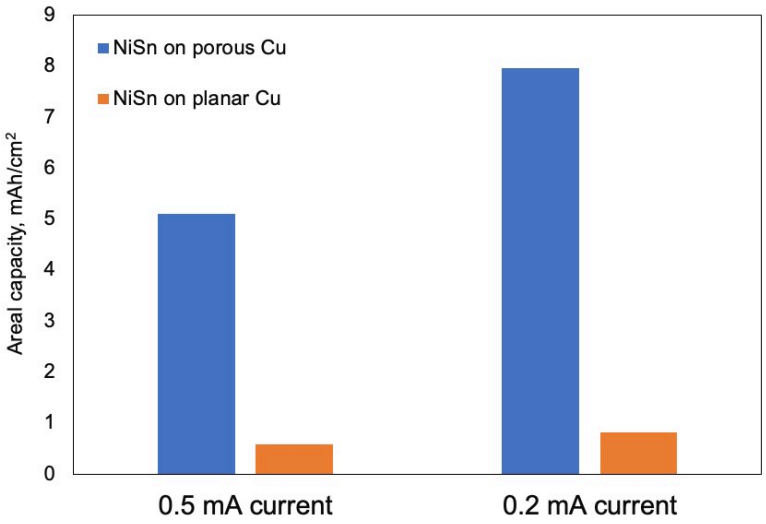

Figure 3. 19**:** Areal capacity performance comparison of NiSn deposited on porous Cu and planar Cu

Although the areal capacity of porous structures is much higher compared to that on a planar substrate, it is still hard to utilize most of the electrode capacity. Due to the ohmic drop in the liquid electrolyte phase, the driving force for electrochemical reactions decreases with distance from the bulk electrolyte for electrodes at the scale in this study (close to 1 mm in thickness) [28]. Li-ion depletion due to mass transfer limitations also contributes to underutilization of the electrode [29]. Thus, substrates with different sizes of laser-machined holes are utilized in this study to improve capacity utilization of the thick electrodes. For example, Figure 3.20 shows the top-down view of the electrode and illustrates the effect of decreasing the hole radius, while maintaining the area occupied by the electrode. By decreasing the radius by a factor of 2, the number of holes quadruples while the total hole area remains the same. Meanwhile, total circumference of the holes doubles, which results more contact area with the bulk electrolyte. This would effectively reduce the mass and charge transport resistance and results in greater utilization of the porous electrode.

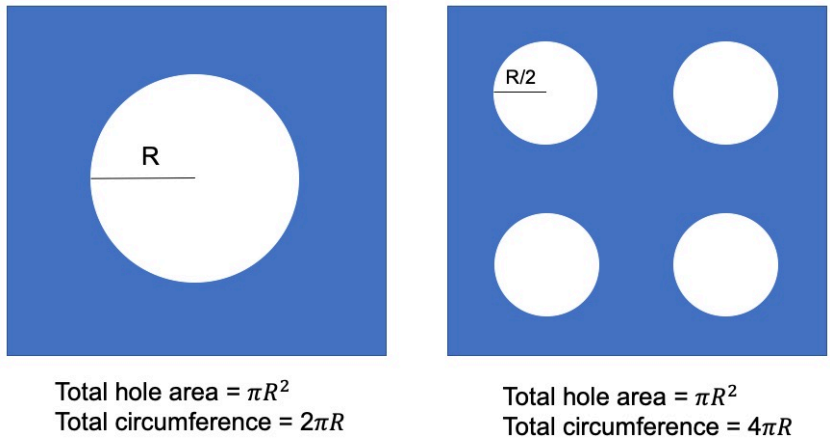

Figure 3. 20**:** Effect of decreasing hole radius on circumference of the holes, while maintaining the total hole area

Figure 3.21 below exhibits the areal capacity comparison for porous NiSn deposited on Cu substrates with different hole sizes. Note, the total area occupied by empty holes remains the same. For example, in order to decrease the hole diameter from 400 μm to 200 μm, the total number of holes quadruples. It is evident that the areal capacity monotonically increases with decreasing hole size, for the reasons explained above.

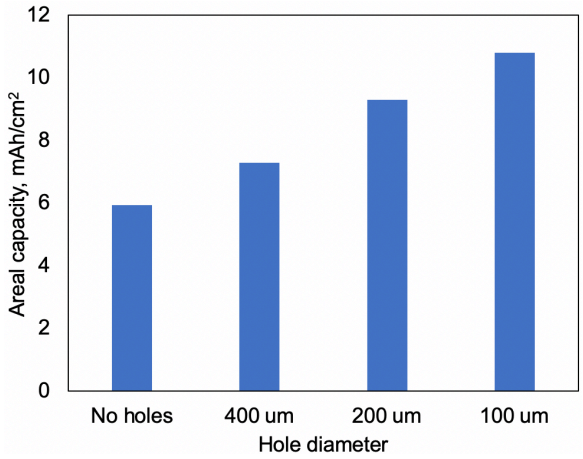

Figure 3. 21**:** Capacity comparison for porous NiSn deposited on Cu substrates with different hole sizes

Figure 3.22 shows the cycling performance of porous NiSn with limited voltage window between 0.05V and 0.9V. More than 75% of the capacity is retained after 90 cycles. This is attributed to the local thin film configuration of the deposited NiSn, which minimizes the stress during cycling process.

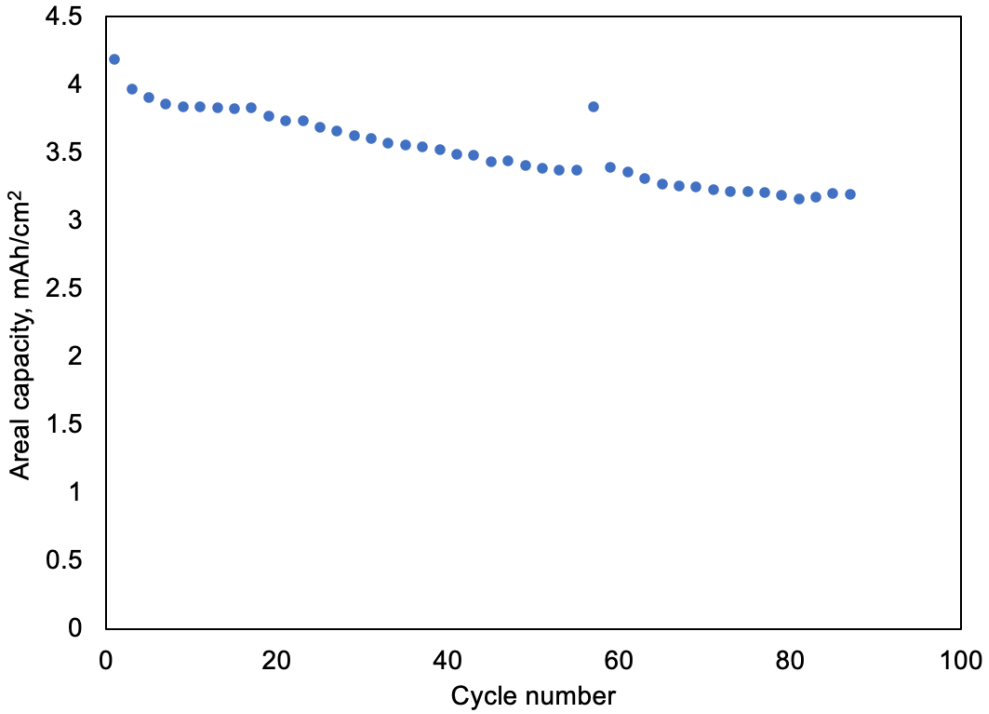

Figure 3. 22**:** Porous NiSn cycling performance

3.4.2. S cathode

The overall redox reaction for the lithiation/delithiation of conventional sulfur cathodes, although is given as $S_8 + 16Li^+ + 16e^- \rightarrow Li_2S$. However, the detailed mechanism involves intermediate steps generating lithium polysulfide species (Li_2S_m, $1 \leq m \leq 8$) with different chain length [30]. In contrast to the NiSn anodes, the S cathodes are normally tested in ether-based electrolyte due to irreversible side reactions between polysulfides and

carbonate-based electrolytes [31]. However, the ether-based electrolyte also faces a series of issues hindering their practical use. First, polysulfide species are highly soluble in ether-based solvents and can easily transport from the cathode to the anode, which results in loss of active sulfur [32]. Moreover, ether-based solvents are highly volatile and have low flash points, posing a significant risk at elevated temperatures [33]. Both issues can be circumvented by the use of carbonate-based electrolyte, if the compatibility issue can be resolved.

Electrochemical testing of sulfur cathode is investigated in both carbonate and ether-based electrolytes. In addition, both liquid-based and gel-based electrolytes are used. Figure 3.23 compares the cycling of a S cathode in carbonate-based liquid electrolyte and carbonate-based gel electrolyte. The liquid electrolyte (or liquid electrolyte precursor for the gel electrolyte system) is 1M $LiPF_6$ in 1:1 EC/DEC (v/v). As illustrated in the figure, in carbonate-based liquid electrolyte, the electrode capacity fades over cycles, whereas in the carbonated-based gel electrolyte for a similar number of cycles, the capacity of the electrode remains stable. Thus, it can be concluded that sulfur deposited on the porous nickel can be compatible with the carbonate electrolyte, as there's no capacity fade in the carbonate-based gel electrolyte system. The capacity loss in the case of pure liquid electrolyte may be due to the sulfur volume expansion during electrochemical cycling and its subsequent detachment from the porous Ni electrode, instead of any chemical side reactions. The gel polymer electrolyte functions as a high-strength matrix that maintains the integrity of the sulfur against its volumetric expansion [19], therefore improving the capacity retention during cycling.

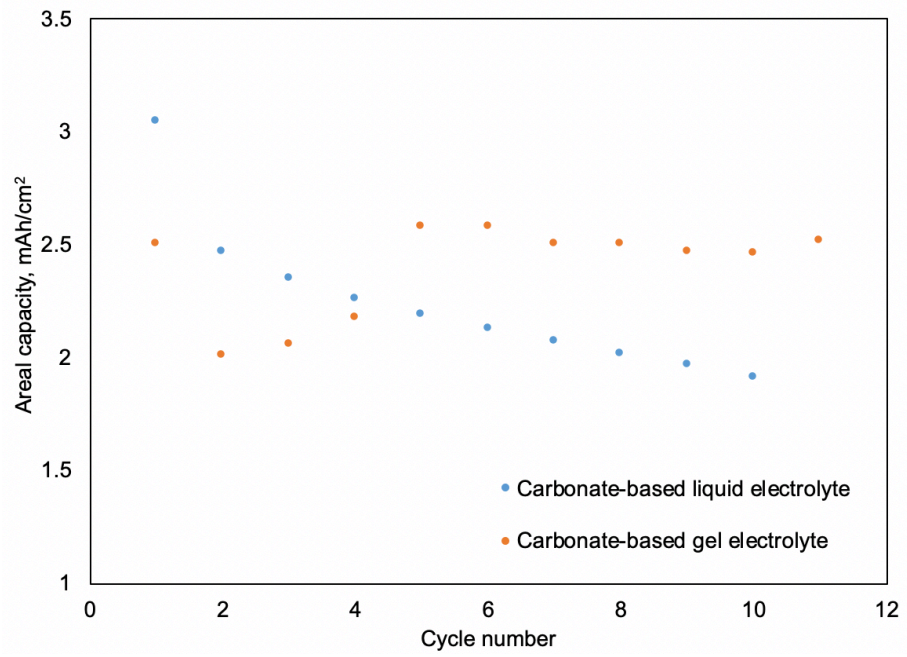

Figure 3. 23**:** Electrochemical cycling of S deposited on porous nickel in 1M $LiPF_6$ in 1:1 EC/DEC (v/v)

In order to further understand why stability of the S electrode is maintained in carbonate electrolytes, electrodes are also cycled in ether-based electrolytes and compared with the performance of conventional S composite electrodes. Comparing Figure 3.24 (b) and (c), the charge and discharge curves of S deposited on porous nickel exhibit similar voltage plateaus in ether-based and carbonate-based systems, at 1.3V during discharge and 2V during charge. This indicates that similar mechanisms occur for both electrolyte systems. A conventional slurry-based S composite cathode, that is composed of 50% Li_2S, 30% carbon conductive material (carbon nanofibers/Super P/graphene nanoplatelets), and 20% PVDF binder, is also tested. As illustrated in Figure 3.24 (a), a conventional S composite electrodes exhibit voltage plateaus that are normally seen in S-based electrode literatures [34-35], in which it is believed that the 2.3 – 2.4V discharge plateau stems from the reduction of cyclo-S_8 molecule to longer-chain polysulfides, followed by 2 – 2.1V

discharge plateau to shorter chain polysulfides. Different potential plateaus suggest different reaction mechanisms for conventional S composite electrodes and S electrodeposited on porous nickel. It is possible that for the latter case, S is converted to Li_2S via a direct solid-phase transformation [34]. Thus, the intermediate liquid phase transformation to polysulfide steps are avoided, and there is no side reaction between the S species and the electrolyte. Consequently, the cycling stability of the electrodeposited S is much improved compared to conventional S composite electrodes, as suggested in Figure 3.24 (d).

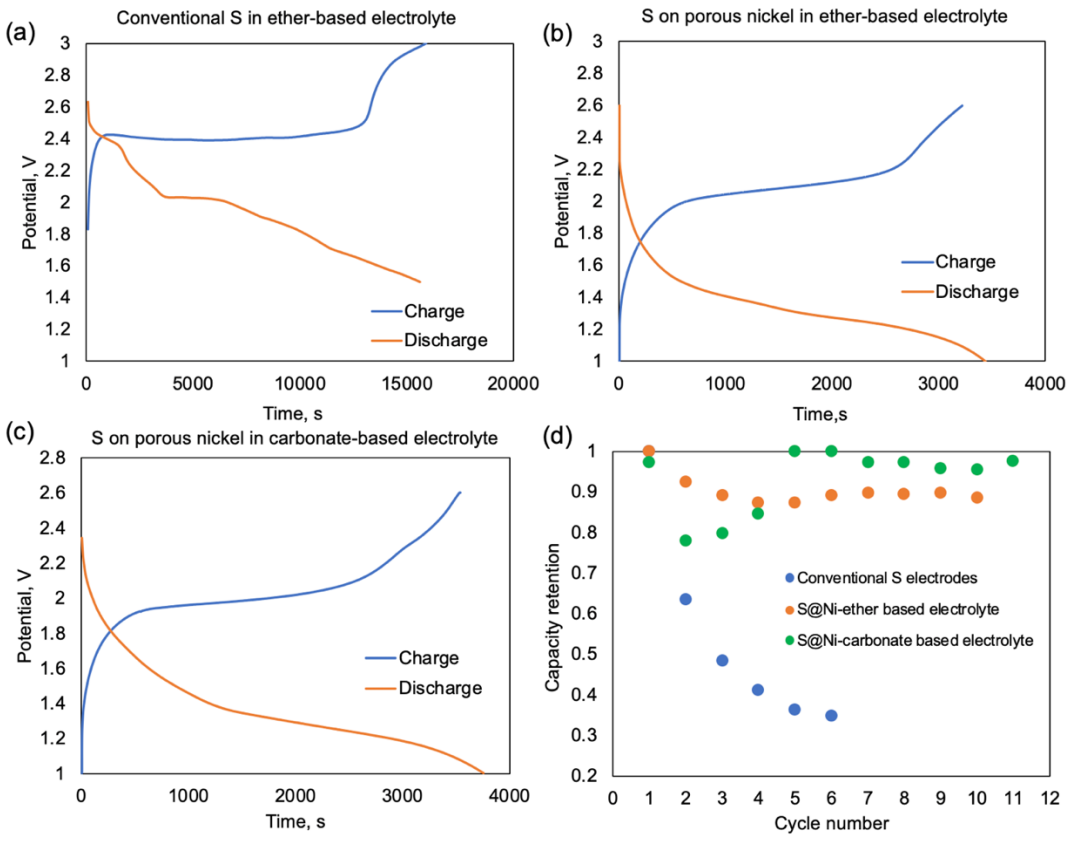

Figure 3. 24 (a) Charge/discharge curves of conventional S cathodes in ether-based electrolyte (1M LiTFSI in 1:1 DME/DOL, 1 wt% $LiNO_3$) (b) Charge/discharge curves of S deposited on porous Ni in ether-based

electrolyte (1M LiTFSI in 1:1 DME/DOL, 1 wt% $LiNO_3$) (c) Charge/discharge curves of S deposited on porous Ni in carbonate-based electrolyte (1M $LiPF_6$ in 1:1 EC/DEC) (d) Cycling performance comparison of three different systems

Figure 3.25 indicates the color of the separators after S electrodes cycling. The yellow color from the conventional S composite electrodes indicates the presence of intermediate species, whereas the separator from the electrodeposited S is colorless, suggesting there is no intermediate conversion to polysulfides and thus no loss of active material.

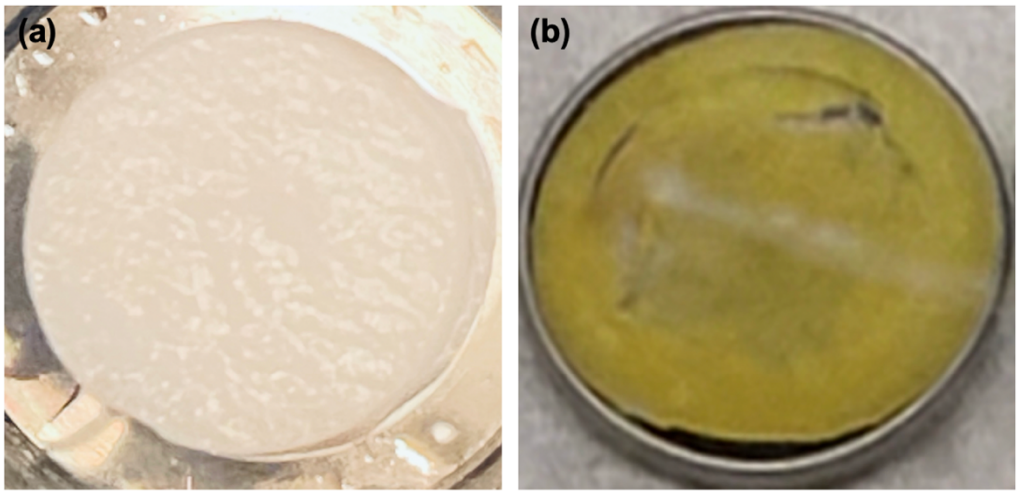

Figure 3. 25**:** Separator color after electrochemical cycling (a) conventional S electrodes (b) Electrodeposited S electrodes

Further performance improvements in the S electrodes can be achieved by the incorporation of additives in the electrolyte, as in the case of NiSn anode. It has been reported in multiple studies that common additives like fluoroethylene carbonate (FEC) and vinylene carbonate (VC) can improve the performance of S-based electrodes [34][36-37]. The improvement is generally attributed to the formation of more effective

protective surface films, the reduction of desolvation energy of Li-ions, and the facilitation of lithium diffusion [36-37]. In this study, 10% FEC and 1%VC are added to compare with the performance using baseline liquid carbonate-based electrolyte. In Figure 3.26, the electrode using the additives exhibit higher capacity and significantly more stable cycling performance compared to the one without any additives.

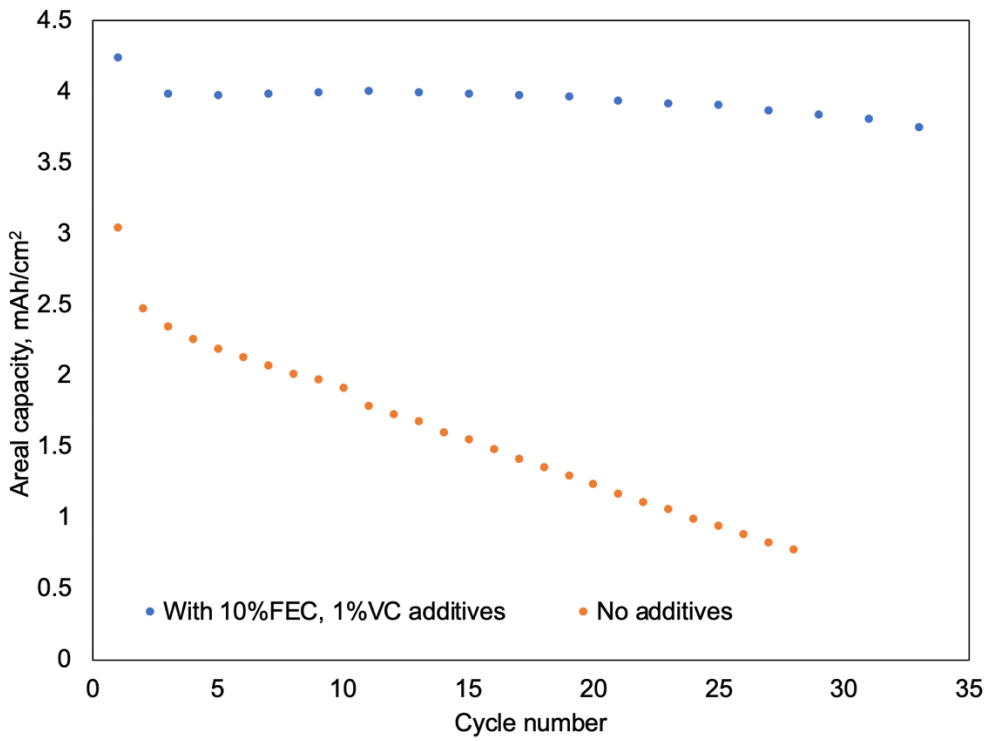

Figure 3. 26**:** Performance comparison of S cathodes with and without additives; Baseline electrolyte: 1M $LiPF_6$ in 1:1 EC/DEC (v/v)

With 10% FEC and 1% VC electrolyte additive, the S electrode deposited using the protocol in section 3.2.2 for 6 hours retains more than 80% of its first cycle capacity after 50 cycles as shown in Figure 3.27. In addition, the areal capacity delivered is as high as

4 mAh/cm^2 at a high current density of 2.5 mA/cm^2.

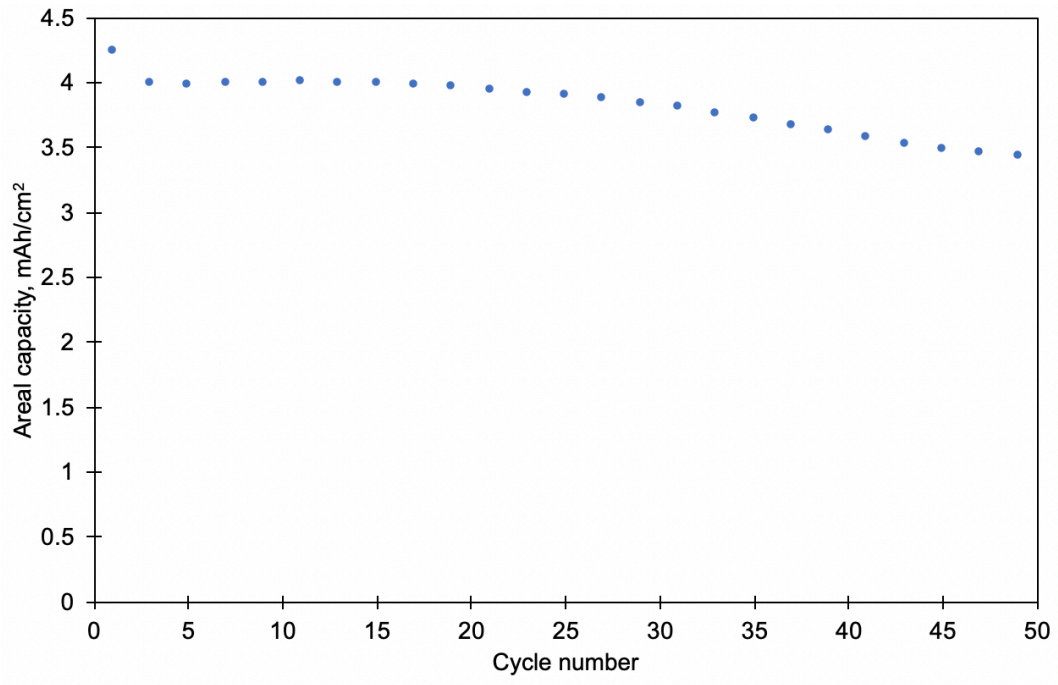

Figure 3. 27**:** Half-cell cycling performance of porous S electrode at 2.5 mA/cm2 current density; electrolyte used is 1M LiPF6 in 1:1 EC/DEC (v/v) + 10% FEC + 1%VC

3.5. Electrochemical performance testing – Full cells

Full cell tests are conducted by assembling the cathode and the anode into a single cell to perform electrochemical cycling. Before full cell cycling, both electrodes are cycled at relatively low rates to form stable SEI (solid electrolyte interface) and CEI (cathode electrolyte interface) films on the surface of the anode and the cathode respectively [38]. This process helps to passivate the electrode surface and prevent further side reactions at the electrode/electrolyte interface, which consumes the limited Li supply in a full cell. Note that in this study, since both electrodes are delithiated as fabricated, the S cathode is lithiated before full cell cycling to act as a source for lithium ions, while the NiSn anode is

fully delithiated. Figure 3.28 shows tests performed in gel electrolyte with and without additives. The baseline electrolyte is 1M $LiPF_6$ in 1:1 EC/DEC (v/v), and the additives are 10 wt% FEC and 1 wt% VC. However, in both cases, a significant capacity drop is observed even in the initial cycles.

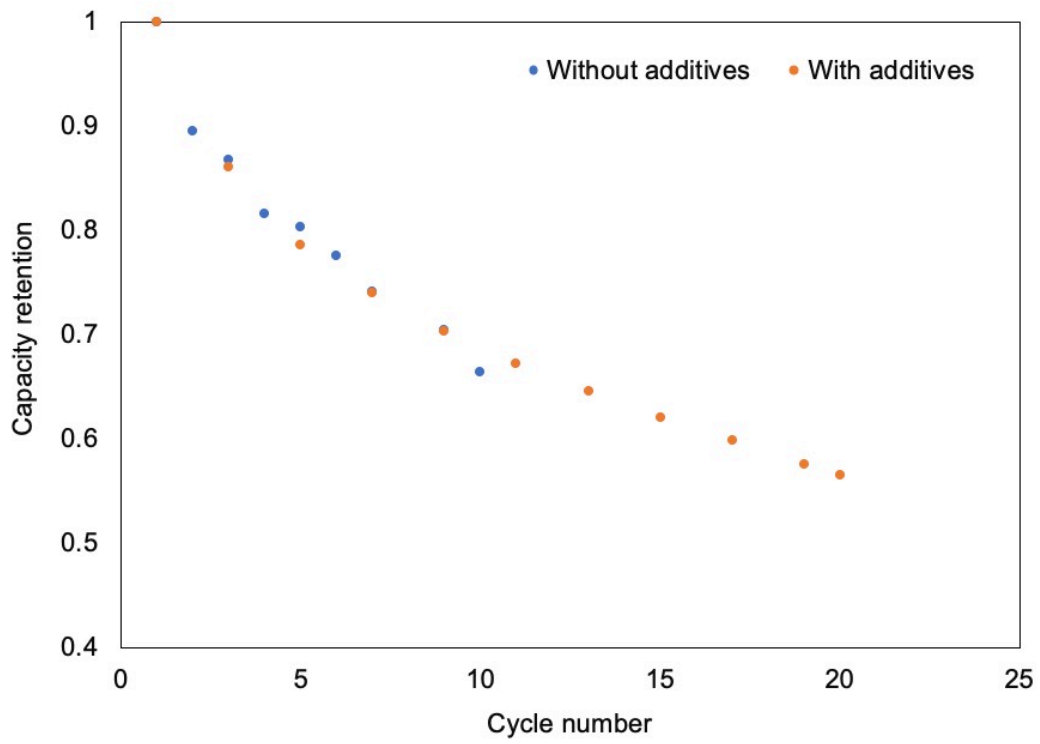

Figure 3. 28**:** Full cell cycling of porous S cathode and NiSn anode in gel electrolyte with and without additives

This capacity decay is not observed in half cell cycling experiments as presented in section 3.4.1 and 3.4.2. An investigation is conducted to find out the reason behind this capacity loss. In lithium-ion batteries, the capacity loss mechanism can be categorized into three major groups below:

1. Loss of lithium inventory (LLI): lithium ions are consumed by parasitic reactions, such as continuous surface film formation (e.g. SEI and CEI growth), decomposition reactions, and lithium plating, and are no longer available for cycling between the positive and negative electrode [39].

2. Loss of active material (LAM): the active mass of the cathode or anode material is no longer available for the insertion of lithium due to particle cracking, detachment from the porous current collector substrate, and/or blocking of active sites [39].

3. Impedance increase: surface reactions kinetics change during cycling process due to the degradation of the electrode/electrolyte interface, as often indicated by a rising cell potential [40]

The degradation mechanism for the battery in this study is likely one or a combination of the above three mechanisms. The effects of the different mechanisms need to be deconvoluted so that it can be determined which one dominates. LLI is the consumption of the limited Li ions due to parasitic reactions. Thus, we can compare the electrode capacity in half cell tests, where the electrode is cycled against a Li metal substrate with effectively an infinite supply of Li ions, before and after full cell tests. If the half-cell capacity is similar before and after the full cell test, then the loss mechanism is most likely due to LLI. If the half-cell capacity of either or both electrodes is drastically different, then the degradation could be attributed to LAM or/and interfacial impedance increase. To further deconvolute these two, the electrode can be cycled at slow rates in half cell tests

before and after full cell tests. If the cycling rate is sufficiently small, then the effect of impedance growth can be neglected, and the half-cell capacity would be similar before and after. Otherwise, the loss is likely due to LAM. Alternatively, the difference between charge and discharge potentials is a good indication of electrode impedance.

Figure 3.29 shows the results from loss mechanism experiment described above. The cathodes and anodes are formed separately in half cell configuration and their capacity is measured at 0.3 mA prior to full cell cycling. Then the full cell was assembled using a gel electrolyte and cycled between 0.6V – 2V at 0.3mA and 0.5mA for a total of 16 cycles. The full cell capacity at 16th cycle shows a significant 80% drop compared to that at the 1st cycle. Then the cathode and the anode are harvested from the full cell and separately assembled into two half cells to check their capacity after full cell cycling. During the capacity checks, the half-cell capacity does not show such significant decay. The cathode capacity is the same as that before full cell cycling, and the anode capacity is even higher, probably due to more infiltration of electrolyte into the porous electrodes during the full cell cycling process.

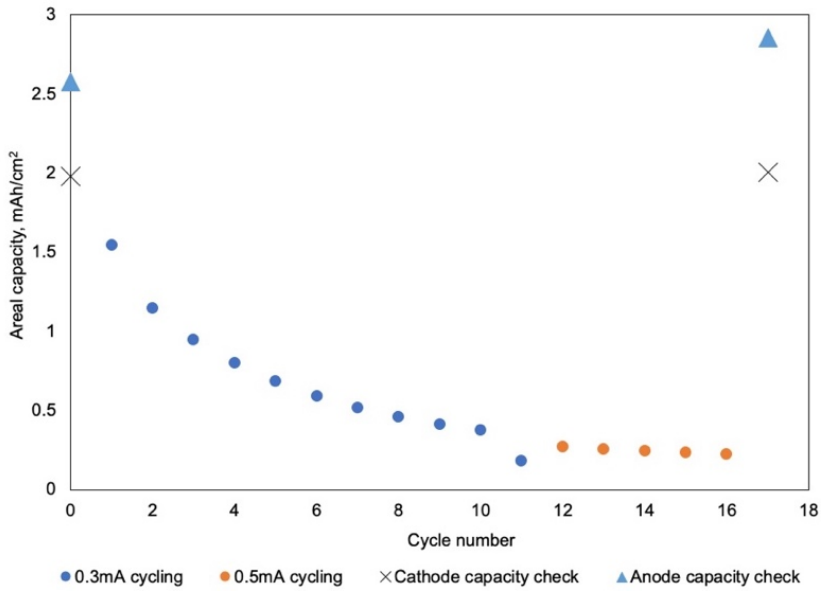

Figure 3. 29**:** Full cell cycling and half-cell capacity check in 1M $LiPF_6$ in 1:1 EC/DEC (v/v) with 10% FEC,1 %VC additive

Thus, there is very little loss of active materials (LAM) during the full cell cycling process. The effect of the kinetic impedance growth is also quantified by the difference between average charge potential and discharge potential before and after the full cell cycling process. During the battery cycling, the application of a current through an electrode is a non-equilibrium condition that causes the electrode potential to deviate from the open circuit potential due to the electrode impedance. The difference in average charge and discharge potential ΔV is calculated to reflect this deviation and the magnitude of impedance, as shown in the two equations below.

$$V_{avg} = \int V.dq \,/ \int dq$$

$$\Delta V = V_{avg,charge} - V_{avg,discharge}$$

Figure 3.30 shows that the impedance growth is very small after the full cell cycling for both cathode and anode. Combined with Figure 3.29, this suggests that the loss of lithium inventory (LLI) is the major loss mechanism.

Cathode impedance growth

	Lithiation average potential, V	Delithiation average potential, V	Average ΔV, V
Before cycling	1.37	1.98	0.61
After cycling	1.32	1.98	0.66

Anode impedance growth

	Lithiation average potential, V	Delithiation average potential, V	Average ΔV, V
Before cycling	0.28	0.8	0.52
After cycling	0.28	0.82	0.54

Figure 3. 30**:** Electrode impedance growth before and after full cell cycling

The LLI mechanism from porous NiSn anode is verified with dV/dQ test. dV/dQ vs. Q plots can be generated by plotting the derivative of voltage with respect to capacity versus capacity of the electrode. The peaks in the dV/dQ represent the phase transitions between phase equilibria represented by voltage plateaus [41]. If the capacity under a voltage plateau decreases, as represented by shortening of inter-peak distances in the dV/dQ plot, then this indicates that there is LAM. If the peaks shift simultaneously without changing the inter-peak distance, there is no LAM and LLI is the major loss mechanism. A three-electrode experiment is designed where the cathode is a commercial $LiFePO_4$ electrode and the anode is a porous NiSn electrode. A separate piece of Li metal foil is used as the reference electrode. Both the full cell potential and the NiSn/Li potential are monitored. Figure 3.31 shows the capacity retention of this cell set-up, with the cell capacity dropped

below 80% after 10 cycles. The commercial $LiFePO_4$ electrode is known to be stable and does not lose capacity in a full cell configuration. This is verified from a previous set-up using a commercial graphite electrode as the anode. Thus, the capacity loss must come from the porous NiSn anode.

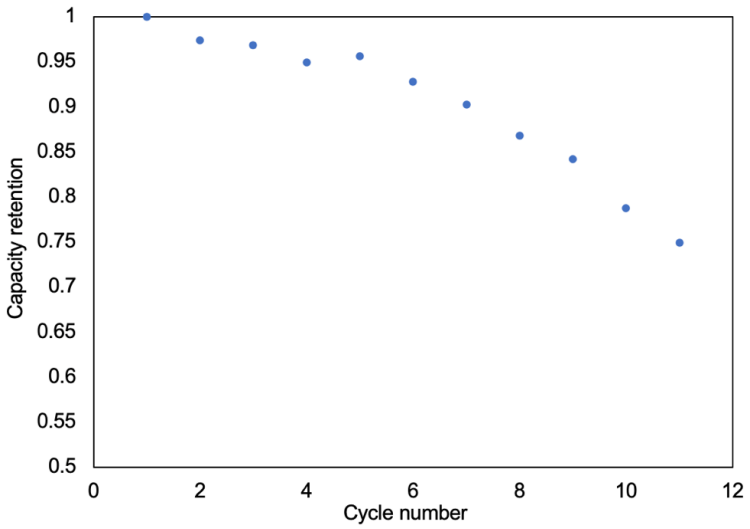

Figure 3. 31**:** Capacity retention vs. cycle number for commercial $LiFePO_4$ vs. porous NiSn cell set-up

Figure 3.32 (a) shows the potential profiles during full cell discharge together with the porous NiSn anode delithiation potential profiles, which are monitored through the Li reference electrode. dV/dQ plots of the NiSn electrode are generated by taking the derivative of potential with respect to areal capacity, which is shown in Figure 3.32 (b). Three peaks are identified corresponding to different stages of phase transitions. The inter-peak distances are calculated in Figure 3.32 (c). It can be seen that there is virtually no change in the inter-peak distance values, indicating no LAM. Thus, the dV/dQ results can further demonstrate that the major loss mechanism is the loss of lithium inventory.

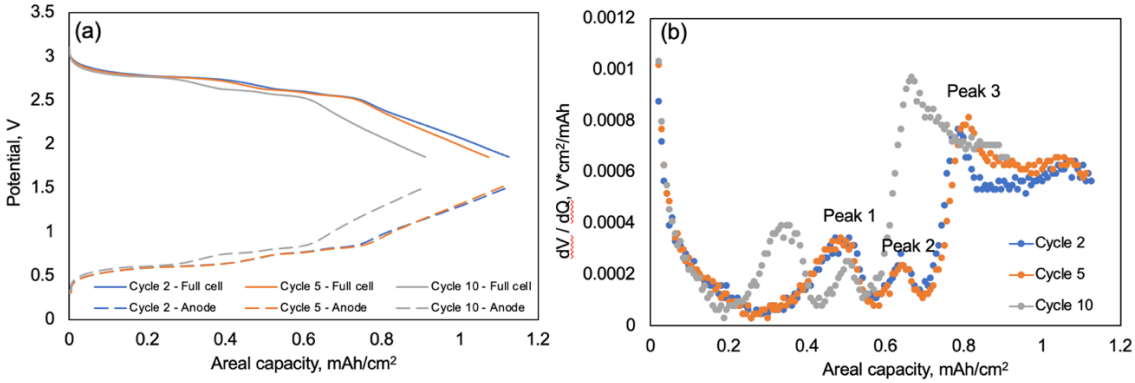

(c)	$Q_{peak\ 1}$, mAh/cm^2	$Q_{peak\ 2}$, mAh/cm^2	$Q_{peak\ 3}$, mAh/cm^2	$Q_{peak\ 2\text{-}1}$, mAh/cm^2	$Q_{peak\ 3\text{-}2}$, mAh/cm^2
Cycle 2	0.493	0.638	0.791	0.145	0.153
Cycle 5	0.486	0.645	0.819	0.159	0.174
Cycle 10	0.347	0.507	0.68	0.16	0.173

Figure 3. 32**:** (a) Full cell discharge and NiSn anode delithiation potential profiles (b) dV/dQ curves for NiSn anode delithiation (c)Inter-peak distance for anode dV/dQ curves

Lithium can be lost either chemically or electrochemically [42]. In Figure 3.33, a porous S vs. porous NiSn full cell was analyzed. The cell was continuously cycled 20 times. Then it was let sit for 24 hours before cycle 21 such that all the loss during this OCV period can be attributed to chemical loss. The capacity loss rate between cycle 1 – 20 is 0.0024% per second, while the loss rate between cycle 20 and 21 is 0.00012%, which is 20 times smaller. This demonstrates that the lithium ions are mainly lost during electrochemical cycling.

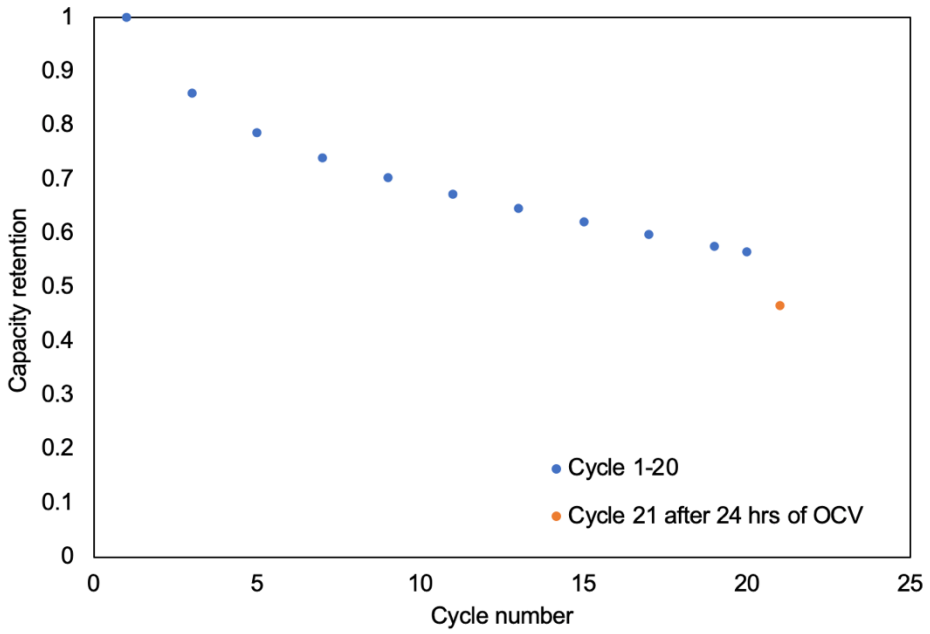

Figure 3. 33**:** Porous S vs. porous S full cell cycling; after cycle 20, the cell was let sit at OCV for 24 hours before cycle 21

Strategies were pursued to reduce the capacity loss as a function of cycle number. For example, Figure 3.34 shows the porous NiSn/porous S full cell cycling over different potential windows. Initially, the full cell is cycled within 0.6 – 2V at 0.3 mA. There is significant capacity decay over the first ten cycles. Then the voltage windows are expanded to 0.4 – 2.2V and 0 – 2.4V. Capacity stabilization is observed, which may be attributed to the SEI formation in the first ten cycles that prevented further side reactions. Thus, better formation protocols need to be developed to ensure better capacity retention in layer cycles.

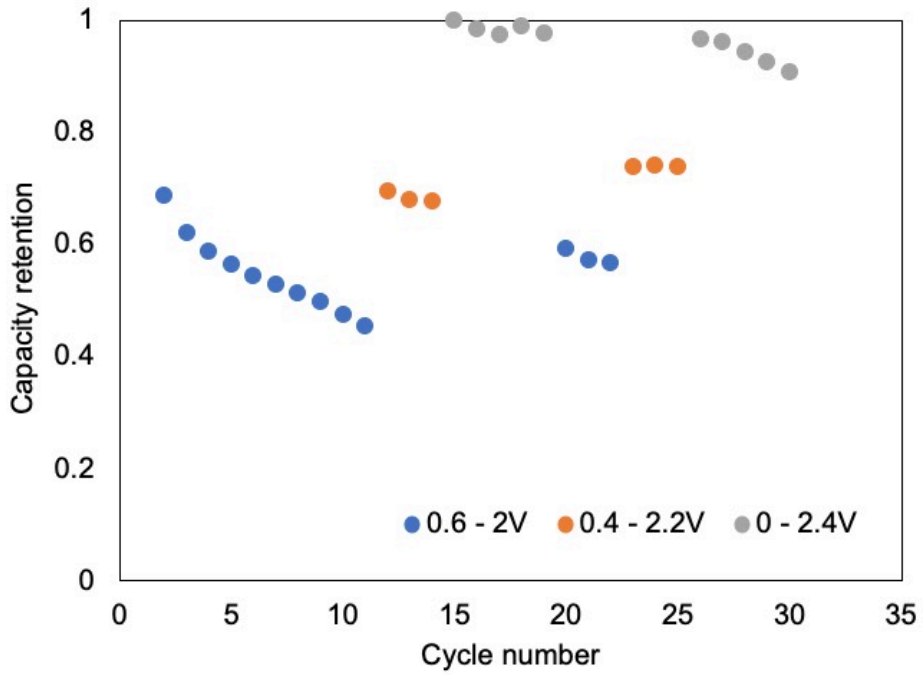

Figure 3. 34**:** Capacity retention as a function of cycle for porous NiSn/porous S full cell within different voltage windows

In addition, controlling the voltage window over which the electrodes are cycled may also have an impact on the cycling performance. Porous NiSn symmetric cells are prepared by cycling half cells to 50% SOC and assembled into symmetric cells, which have OCV close to 0V before cycling. Then these symmetric cells are cycled within different voltage windows. Figure 3.35 demonstrates the effect of cycling three symmetric cells within different voltage windows. Capacity retention decreases with expansion in voltage windows. It is likely that the extent of NiSn volume expansion/contraction increases with the voltage window. Although the NiSn is still attached to the porous Cu substrate, the amount of cracks may increase, destroying previously formed SEI and exposing fresh NiSn surfaces for side reactions to occur.

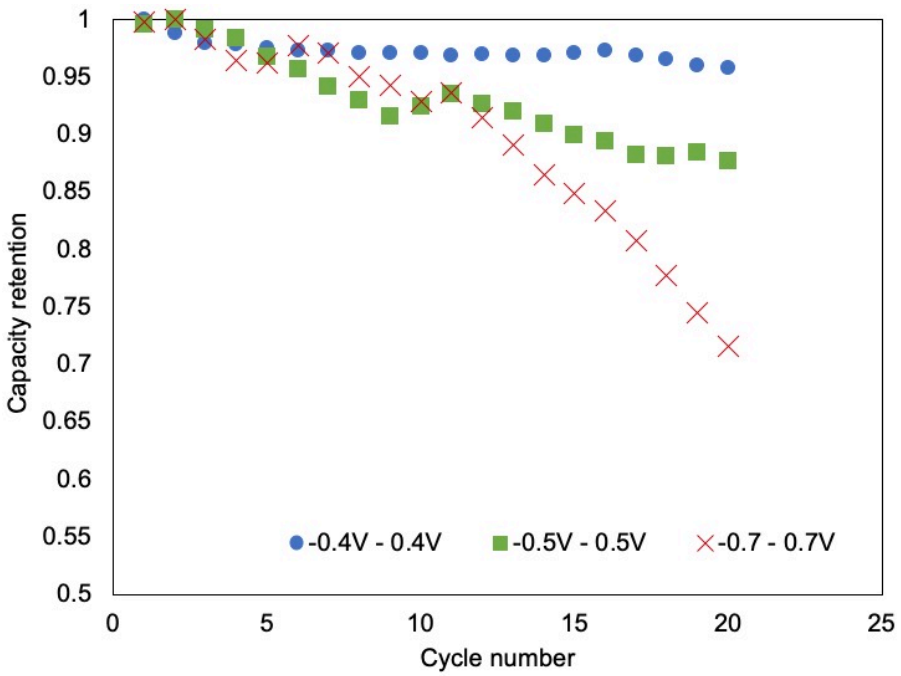

Figure 3. 35**:** Capacity retention as a function of cycle number for porous NiSn symmetric cells that are cycled over different voltage windows

Although strategies are still being pursued to reduce loss of lithium inventory and achieve stable full cell performance, first cycle areal capacity of 3 mAh/cm^2 (Figure 3.36 (a)) has been attained with 2.3 mWh/cm^2 areal power density. This performance is within the upper range of the micro-batteries developed so far as shown in the Ragone plot in Figure 3.36 (b) below.

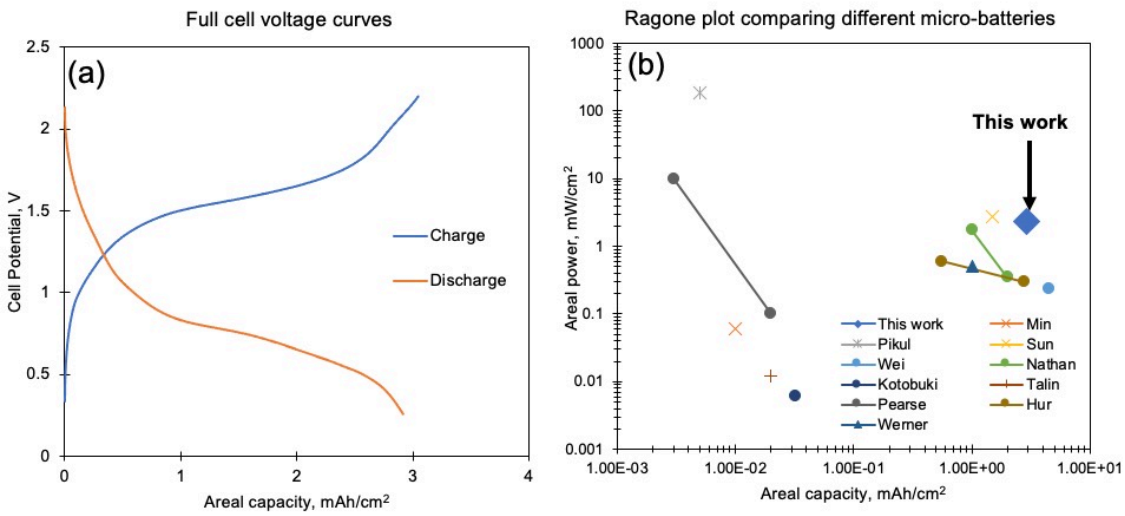

Figure 3. 36**:** (a) Full cell voltage profile for porous NiSn/S full cell cycled between 0.25V and 2.2V (b) Ragone plot comparing different micro-batteries

3.6. Conclusions

In this chapter, fabrication of Li-ion micro-batteries using porous copper as scaffold is demonstrated. Electrochemical methods such as alternating deposition and stripping cycles are applied to ensure conformal plating of secondary metal and active material on the mm scale scaffold. The resulting 3D porous electrodes have demonstrated superior energy and cycle performance compared with those on a planar substrate, with the help from electrolyte additives and gel polymer electrolyte. Such improved performance are attributed to high surface area and scalability of the porous Cu scaffolds. In addition, the design of hole size on the Cu substrates decreases the mass and charge transport resistance and allows higher capacity utilization to be achieved. Full cell cycling of porous NiSn/S experiences capacity loss due to lithium inventory loss. Strategies are still being pursued to achieve better cycling performance, such as improved formation protocols and control of potential windows.

3.7. Reference

1. Suk, J., Kim, D. W., & Kang, Y. (2014). Electrodeposited 3D porous silicon/copper films with excellent stability and high rate performance for lithium-ion batteries. *Journal of Materials Chemistry A*, *2*(8), 2478-2481.
2. Ott, A., Jones, L. A., & Bhargava, S. K. (2011). Direct electrodeposition of porous platinum honeycomb structures. *Electrochemistry communications*, *13*(11), 1248-1251.
3. Cherevko, S., & Chung, C. H. (2010). The porous CuO electrode fabricated by hydrogen bubble evolution and its application to highly sensitive non-enzymatic glucose detection. *Talanta*, *80*(3), 1371-1377.
4. Wang, Y., Liu, B., Li, Q., Cartmell, S., Ferrara, S., Deng, Z. D., & Xiao, J. (2015). Lithium and lithium ion batteries for applications in microelectronic devices: A review. *Journal of Power Sources*, *286*, 330-345.
5. Jiang, T., Zhang, S., Qiu, X., Sun, M., & Chen, L. (2008). A three-dimensional cellular copper prepared by multiple-step electrodeposition. *Electrochemical and Solid State Letters*, *11*(5), D50.
6. Pikul, J. H., Liu, J., Braun, P. V., & King, W. P. (2016). Integration of high capacity materials into interdigitated mesostructured electrodes for high energy and high power density primary microbatteries. *Journal of Power Sources*, *315*, 308-315.
7. Wu, S., Liu, X., Hu, T., Jiang, J., Chu, P. K., Yeung, K. W. K., ... & Cheung, K. M. C. (2009). Electrochemical stability of orthopedic porous NiTi shape memory alloys treated by different surface modification techniques. *Journal of the Electrochemical Society*, *156*(6), C187.
8. Liu, L., Xie, F., Lyu, J., Zhao, T., Li, T., & Choi, B. G. (2016). Tin-based anode materials with well-designed architectures for next-generation lithium-ion batteries. *Journal of Power Sources*, *321*, 11-35.
9. Mukaibo, H., Momma, T., Mohamedi, M., & Osaka, T. (2005). Structural and morphological modifications of a nanosized 62 atom percent Sn-Ni thin film anode during reaction with lithium. *Journal of the Electrochemical Society*, *152*(3), A560.

10. Ishikawa, M., Enomoto, H., Matsuoka, M., & Iwakura, C. (1995). Effect of some factors on electrodeposition of nickel-copper alloy from pyrophosphate-tetraborate bath. *Electrochimica acta*, *40*(11), 1663-1668.
11. Peng, H. J., Huang, J. Q., Cheng, X. B., & Zhang, Q. (2017). Review on high-loading and high-energy lithium–sulfur batteries. *Advanced Energy Materials*, *7*(24), 1700260.
12. Zhao, Q., Hu, X., Zhang, K., Zhang, N., Hu, Y., & Chen, J. (2015). Sulfur nanodots electrodeposited on Ni foam as high-performance cathode for Li–S batteries. *Nano letters*, *15*(1), 721-726.
13. Ji, X., Lee, K. T., & Nazar, L. F. (2009). A highly ordered nanostructured carbon–sulphur cathode for lithium–sulphur batteries. *Nature materials*, *8*(6), 500-506.
14. Markevich, E., Salitra, G., Rosenman, A., Talyosef, Y., Aurbach, D., & Garsuch, A. (2014). High performance of thick amorphous columnar monolithic film silicon anodes in ionic liquid electrolytes at elevated temperature. *RSC Advances*, *4*(89), 48572-48575.
15. Zhou, D., Fan, L. Z., Fan, H., & Shi, Q. (2013). Electrochemical performance of trimethylolpropane trimethylacrylate-based gel polymer electrolyte prepared by in situ thermal polymerization. *Electrochimica Acta*, *89*, 334-338.
16. Li, X., Qian, K., He, Y. B., Liu, C., An, D., Li, Y., ... & Kang, F. (2017). A dual-functional gel-polymer electrolyte for lithium ion batteries with superior rate and safety performances. *Journal of Materials Chemistry A*, *5*(35), 18888-18895.
17. Xu, K. (2014). Electrolytes and interphases in Li-ion batteries and beyond. *Chemical reviews*, *114*(23), 11503-11618.
18. Li, X., Shao, J., Kim, S. K., Yao, C., Wang, J., Miao, Y. R., ... & Braun, P. V. (2018). High energy flexible supercapacitors formed via bottom-up infilling of gel electrolytes into thick porous electrodes. *Nature communications*, *9*(1), 1-8.
19. Liu, M., Zhou, D., He, Y. B., Fu, Y., Qin, X., Miao, C., ... & Zhao, T. S. (2016). Novel gel polymer electrolyte for high-performance lithium–sulfur batteries. *Nano energy*, *22*, 278-289.

20. Hassoun, J., Panero, S., Simon, P., Taberna, P. L., & Scrosati, B. (2007). High-rate, long-life Ni–Sn nanostructured electrodes for lithium-ion batteries. *Advanced Materials*, *19*(12), 1632-1635.
21. Hong, S., Choo, M. H., Kwon, Y. H., Kim, J. Y., & Song, S. W. (2016). Mechanisms for Stable Solid Electrolyte Interphase Formation and Improved Cycling Stability of Tin-Based Battery Anode in Fluoroethylene Carbonate-Containing Electrolyte. *Advanced Materials Interfaces*, *3*(22), 1600172.
22. Aupperle, F., von Aspern, N., Berghus, D., Weber, F., Eshetu, G. G., Winter, M., & Figgemeier, E. (2019). The Role of Electrolyte Additives on the Interfacial Chemistry and Thermal Reactivity of Si-Anode-Based Li-Ion Battery. *ACS Applied Energy Materials*, *2*(9), 6513-6527.
23. Seo, D. M., Nguyen, C. C., Young, B. T., Heskett, D. R., Woicik, J. C., & Lucht, B. L. (2015). Characterizing solid electrolyte interphase on Sn anode in lithium ion battery. *Journal of the Electrochemical Society*, *162*(13), A7091.
24. Dalavi, S., Guduru, P., & Lucht, B. L. (2012). Performance enhancing electrolyte additives for lithium ion batteries with silicon anodes. *Journal of The Electrochemical Society*, *159*(5), A642.
25. Xu, C., Lindgren, F., Philippe, B., Gorgoi, M., Björefors, F., Edström, K., & Gustafsson, T. (2015). Improved performance of the silicon anode for Li-ion batteries: understanding the surface modification mechanism of fluoroethylene carbonate as an effective electrolyte additive. *Chemistry of Materials*, *27*(7), 2591-2599.
26. Chen, X., Li, X., Mei, D., Feng, J., Hu, M. Y., Hu, J., ... & Liu, J. (2014). Reduction mechanism of fluoroethylene carbonate for stable solid–electrolyte interphase film on silicon anode. *ChemSusChem*, *7*(2), 549-554.
27. Burns, J. C., Krause, L. J., Le, D. B., Jensen, L. D., Smith, A. J., Xiong, D., & Dahn, J. R. (2011). Introducing symmetric Li-ion cells as a tool to study cell degradation mechanisms. *Journal of The Electrochemical Society*, *158*(12), A1417.
28. Doyle, M., Fuller, T. F., & Newman, J. (1993). Modeling of galvanostatic charge and discharge of the lithium/polymer/insertion cell. *Journal of the Electrochemical society*, *140*(6), 1526.

29. Du, Z., Wood, D. L., Daniel, C., Kalnaus, S., & Li, J. (2017). Understanding limiting factors in thick electrode performance as applied to high energy density Li-ion batteries. *Journal of Applied Electrochemistry*, *47*(3), 405-415.
30. Zhang, S., Ueno, K., Dokko, K., & Watanabe, M. (2015). Recent advances in electrolytes for lithium–sulfur batteries. *Advanced Energy Materials*, *5*(16), 1500117.
31. Yim, T., Park, M. S., Yu, J. S., Kim, K. J., Im, K. Y., Kim, J. H., ... & Lee, I. (2013). Effect of chemical reactivity of polysulfide toward carbonate-based electrolyte on the electrochemical performance of Li–S batteries. *Electrochimica Acta*, *107*, 454-460.
32. Fang, R., Zhao, S., Sun, Z., Wang, D. W., Cheng, H. M., & Li, F. (2017). More reliable lithium-sulfur batteries: status, solutions and prospects. *Advanced materials*, *29*(48), 1606823.
33. Li, X., Lushington, A., Sun, Q., Xiao, W., Liu, J., Wang, B., ... & Li, R. (2016). Safe and durable high-temperature lithium–sulfur batteries via molecular layer deposited coating. *Nano letters*, *16*(6), 3545-3549.
34. Li, X., Banis, M., Lushington, A., Yang, X., Sun, Q., Zhao, Y., ... & Wang, C. (2018). A high-energy sulfur cathode in carbonate electrolyte by eliminating polysulfides via solid-phase lithium-sulfur transformation. *Nature communications*, *9*(1), 1-10.
35. Lee, J. T., Eom, K., Wu, F., Kim, H., Lee, D. C., Zdyrko, B., & Yushin, G. (2016). Enhancing the stability of sulfur cathodes in Li–S cells via in situ formation of a solid electrolyte layer. *ACS Energy Letters*, *1*(2), 373-379.
36. Markevich, E., Salitra, G., Rosenman, A., Talyosef, Y., Chesneau, F., & Aurbach, D. (2015). Fluoroethylene carbonate as an important component in organic carbonate electrolyte solutions for lithium sulfur batteries. *Electrochemistry Communications*, *60*, 42-46.
37. Li, Q., Yang, H., Naveed, A., Guo, C., Yang, J., Nuli, Y., & Wang, J. (2018). Duplex component additive of tris (trimethylsilyl) phosphite-vinylene carbonate for lithium sulfur batteries. *Energy Storage Materials*, *14*, 75-81.
38. Wood III, D. L., Li, J., & An, S. J. (2019). Formation challenges of lithium-ion battery manufacturing. *Joule*, *3*(12), 2884-2888.

39. Birkl, C. R., Roberts, M. R., McTurk, E., Bruce, P. G., & Howey, D. A. (2017). Degradation diagnostics for lithium ion cells. *Journal of Power Sources*, *341*, 373-386.
40. Dubarry, M., Devie, A., & Liaw, B. Y. (2014). The value of battery diagnostics and prognostics. *J. Energy Power Sources*, *1*(5), 242-249.
41. Bloom, I., Jansen, A. N., Abraham, D. P., Knuth, J., Jones, S. A., Battaglia, V. S., & Henriksen, G. L. (2005). Differential voltage analyses of high-power, lithium-ion cells: 1. Technique and application. *Journal of Power Sources*, *139*(1-2), 295-303.
42. Smith, A. J., Burns, J. C., & Dahn, J. R. (2010). A high precision study of the Coulombic efficiency of Li-ion batteries. *Electrochemical and Solid State Letters*, *13*(12), A177.

CHAPTER 4: FABRICATION OF LI-ION MICRO-BATTERIES USING POROUS NiSn/Si COMPOSITES AS SCAFFOLDS

In the previous chapter, the fabrication of Li-ion micro-batteries using porous copper as scaffold was demonstrated. However, it requires two separate fabrication processes, one for cathode and one for anode respectively, which then had to be combined to form the full-cell battery. The manufacturing process can be simplified if one monolithic piece of device can be fabricated, including cathode, anode, and electrolyte. In addition, the gel electrolyte developed in chapter 3 still contains significant amount of liquid content. It would be more desirable to have an all-solid-state electrolyte since it possesses better thermal, mechanical, chemical, and electrochemical stabilities compared to liquid electrolytes. Thus, a new process is investigated in the present chapter. A composite porous NiSn/Si anode, instead of porous copper, is utilized as the scaffold where subsequent battery components are loaded. An ultrahigh areal capacity about 40 mAh/cm^2 is achieved. Stable cycling performance is realized with the help of binder materials. Then, a layer of solid polymer electrolyte, poly(phenylene oxide) (PPO), is electrodeposited onto the porous NiSn, followed by a lithium sulfide (Li_2S) cathode slurry infiltration into the porous structure (See Figure 4.1 below). In addition, PPO electrodeposition is further investigated in detail to avoid incomplete coverage of PPO electrolyte on the anode surface and reduce the failure rate due to shorting.

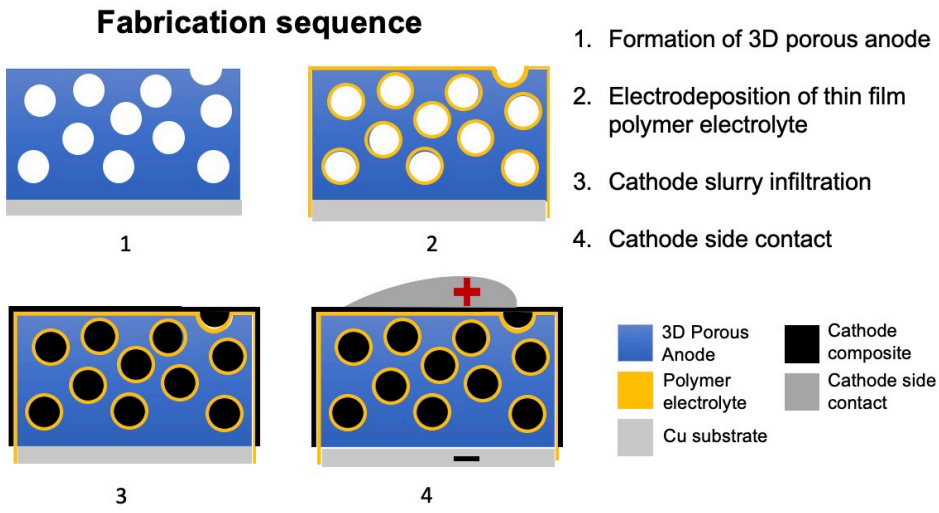

Figure 4. 1**:** Fabrication sequence of Li-ion micro-batteries using porous NiSn as the scaffold

4.1. Fabrication of porous NiSn/Si composite anode

The NiSn/Si composite is prepared in a similar fashion as described in Chapter 2. The major difference is that Si particles are settled at the bottom of the deposition bath and Cu substrate is submerged within this layer of Si particles, as illustrated in Figure 4.2. The bath composition is 0.4M $NiCl_2$, 0.04M $SnCl_2$, and 1M H_2SO_4. As a high reduction current of 3 A/cm^2 is applied, hydrogen bubbles evolve from the Cu substrate surface due to reduction of H^+ ions. 3D NiSn structure grows simultaneously and uses the H_2 bubbles as dynamic templates to result in a porous structure. This time, the porous NiSn grows through the settled Si particles and embed the Si particles within the NiSn matrix. Compared to the previous process where an extra step has to be added to deposit NiSn onto the porous structure, the active material itself serves as the scaffold and is deposited in a single, facile step. In addition, there is no concern regarding conformal deposition of the active material onto a 3D structure.

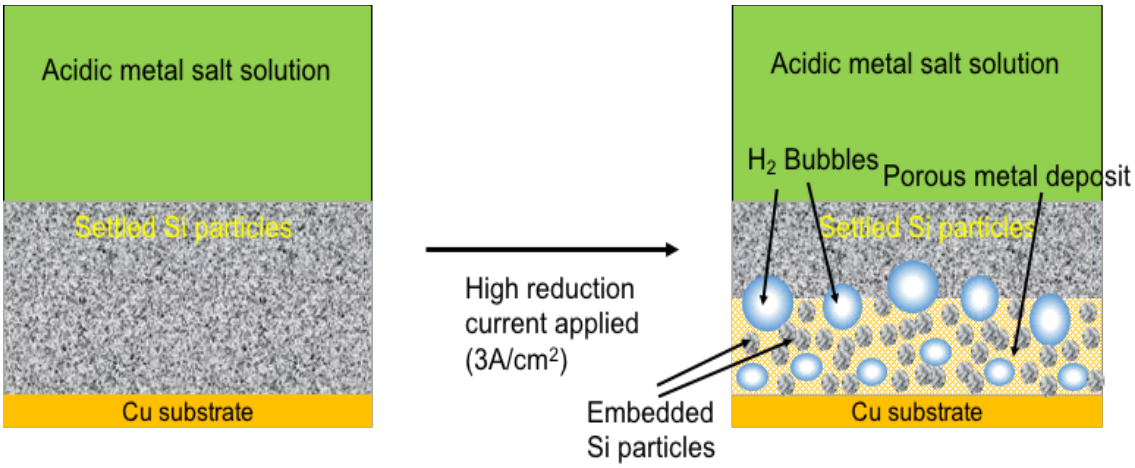

Figure 4. 2**:** Fabrication of composite porous NiSn/Si anode

Figure 4.3 (a) shows the top-view SEM image for this composite structure, which is uniform in X-Y direction over millimeter scale. In addition, as illustrated in (b), this composite is highly scalable to mm scale in z direction with a deposition duration of 10 minutes. Porous NiSn not only serves as the active material, but also provides an electrical conduction network for Si particles to be electrochemically utilized. Since both NiSn and Si have high specific energy, in combination with scalability of the electrode, a 3D porous electrode with ultrahigh areal capacity is expected.

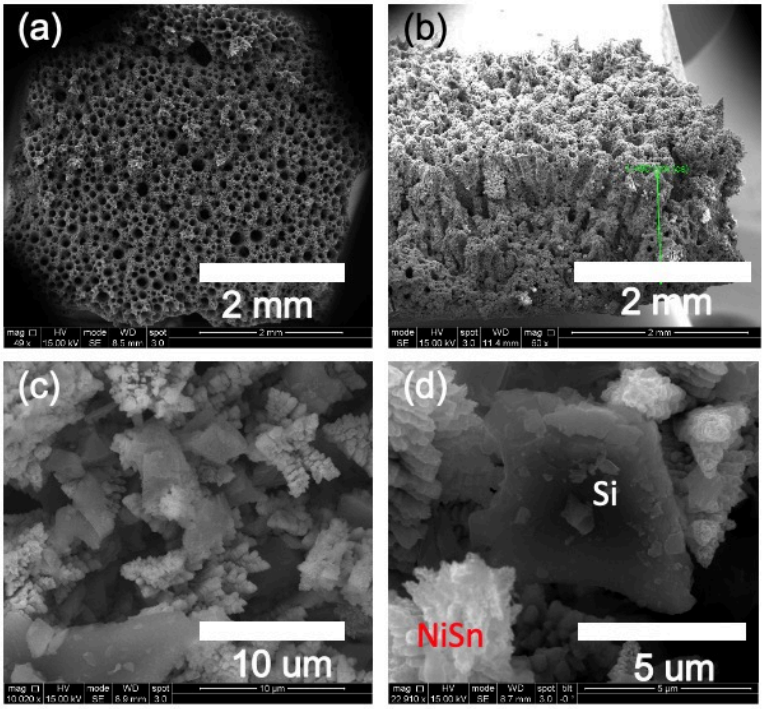

Figure 4. 3**:** (a) Top view of the porous NiSn/Si composite (b) Cross-sectional view of the porous NiSn/Si composite (c) (d) Zoom-in views of the porous NiSn/Si composite at different magnifications

The sample is then subjected to electrochemical testing after cleaning in water and drying in vacuum oven for 12 hours at 50 ℃. Li foil is used as the counter electrode and 1M $LiPF_6$ in 1:1 EC/DEC (v/v) with 10% FEC and 1% VC additive is used as the electrolyte during testing, which is shown in the previous chapter to improve cycle life of the electrode. 20 mA/g or 1 mA/cm^2 current is applied to charge/discharge the electrode between 0.01V and 1.5V versus lithium counter electrode. Figure 4.4 (a) exhibits an ultrahigh capacity of 40 mAh/cm^2**,** owing to scalability of the deposited sample and high specific capacity of NiSn and Si.

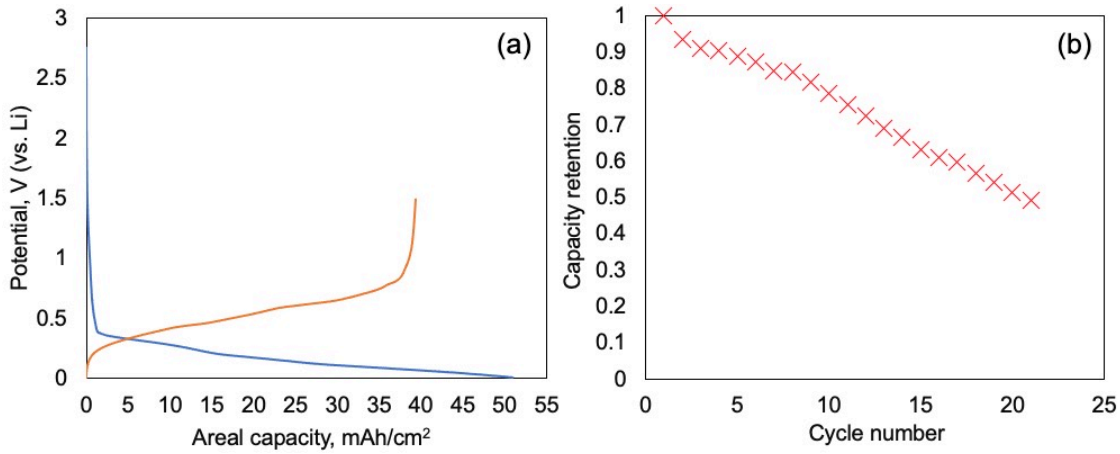

Figure 4. 4**:** (a) 1st cycle areal capacity of porous NiSn/Si composite electrode at 20 mA/g (b) Cycling stability of the porous NiSn/Si composite electrode without binder materials

However, as shown in Figure 4.4 (b), the cyclability of the electrode is undesirable due to the severe volume expansion/contraction of Sn/Si based materials during cycling, which causes the active material to detach from the conductive network and results in loss of capacity. Thus, it is essential to utilize a binder material to hold the active materials together and prevent them from disconnecting from the conductive network. Commonly used binder materials for Sn/Si materials include carboxylmethylcellulose (CMC) and poly(acrylic acid) (PAA) [1][2][3]. High mechanical rigidity, the lack of interactions with solvent molecules, and strong hydrogen bonds that form between carboxyl (-COOH) groups and hydroxyl (-OH) groups on the Si enable improved capacity retention using these binders, compared to conventional binder materials such as polyvinylidene fluoride (PVDF) with no specific interactions [1][3]. More recently, other novel binder materials have also been utilized. For example, conductive polymers such as poly(3,4-ethylenedioxythiophene) polystyrene sulfonate (PEDOT:PSS) eliminate the tenuous interface between silicon and

conventional inorganic conductive matrix and avoids capacity loss due to physical separations [4]. In this study, three different binder materials, namely PAA, CMC, and PEDOT:PSS, are investigated for the electro-deposited porous NiSn/Si composite.

Following the electrodeposition process described earlier, samples are immersed in aqueous solutions containing the polymer binders. The concentration of each aqueous solution is listed in Table 4.1. Before immersion, samples are briefly dipped in IPA. Then the samples are immersed in the respective polymer aqueous solutions and placed in the vacuum oven overnight at 50 ℃, such that bubbles trapped in the porous structure can be removed, and polymer binders can infiltrate into the pores more easily. Figure 4.5 shows the SEM image before and after PAA infiltrates and integrates with the composite anode.

	PAA	CMC	PEDOT
Concentration, weight %	1%	0.2%	1 – 1.5%

Table 4. 1**:** Concentrations of polymer binder aqueous solution

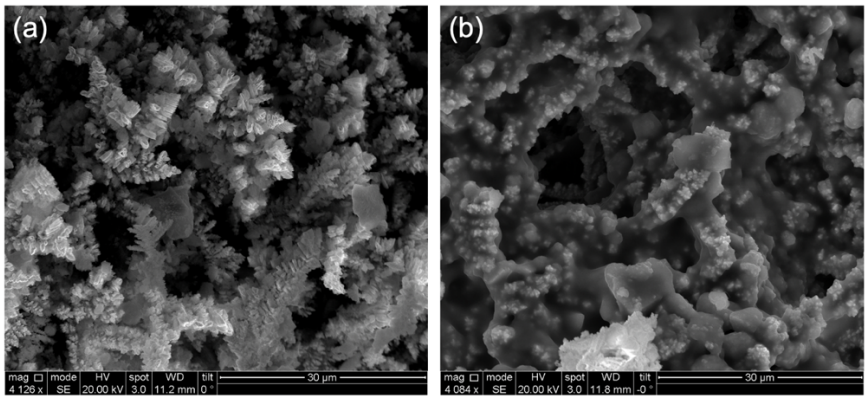

Figure 4. 5**:** NiSn/Si composite (a) Before and (b) after polymer infiltration

Figure 4.6 (a) compares the capacity retention performance using different polymer binder materials at a cycling rate of 75 mA/g. Each binder accounts for 10% of the total electrode weight. All samples with binders exhibit better capacity retention compared to the case without any binders. PEDOT retains the least percentage of capacity after 20 cycles, likely due to the lack of carboxylic acid functional groups required for self-healing [4]. As a result of the higher concentration of carboxylic acid groups on PAA compared to CMC, the sample with PAA binder has better capacity retention [2][3].

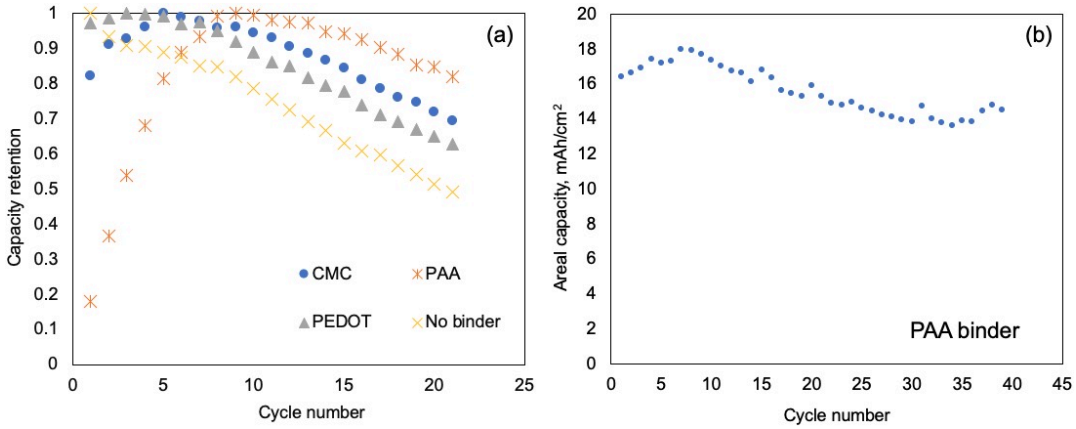

Figure 4. 6**:** (a) Capacity retention of composite NiSn/Si anode using different binder materials at 75mA/g (b) Cycling data of composite NiSn/Si anode using PAA at 39 mA/g

Figure 4.6 (b) shows the cycling data of NiSn/Si composite with 10% PAA at a cycling rate of 39 mA/g. The sample retains about 90% percent of its first cycle capacity and 82% of its highest capacity at 8th cycle. A high average areal capacity of 15 mAh/cm^2 is exhibited. Note that the better capacity retention performance in Figure 4.6 (b) compared to that in Figure 4.6 (a) with PAA binder is partially attributed to the smaller specific current, which reduces the stress exerted on the active material particles [5].

As described in Section 3.4.1, electrode utilization can increase when laser-machined holes are applied on the substrate surface. The total capacity increases with decrease in hole size, which increases the contact area with the bulk electrolyte and results in reduction of charge and mass transport resistance. Similar improvement can also be observed for porous NiSn/Si composite electrodes. Composite electrodes using different hole size on the substrate are both cycled at 75 mA/g. Note that both samples possess similar mass loading (9 mg for 200 μm sample and 8.2 mg for 400 μm sample). The sample with 200 μm holes exhibits much higher capacity than the one with 400 μm holes, as shown in Figure 4.7.

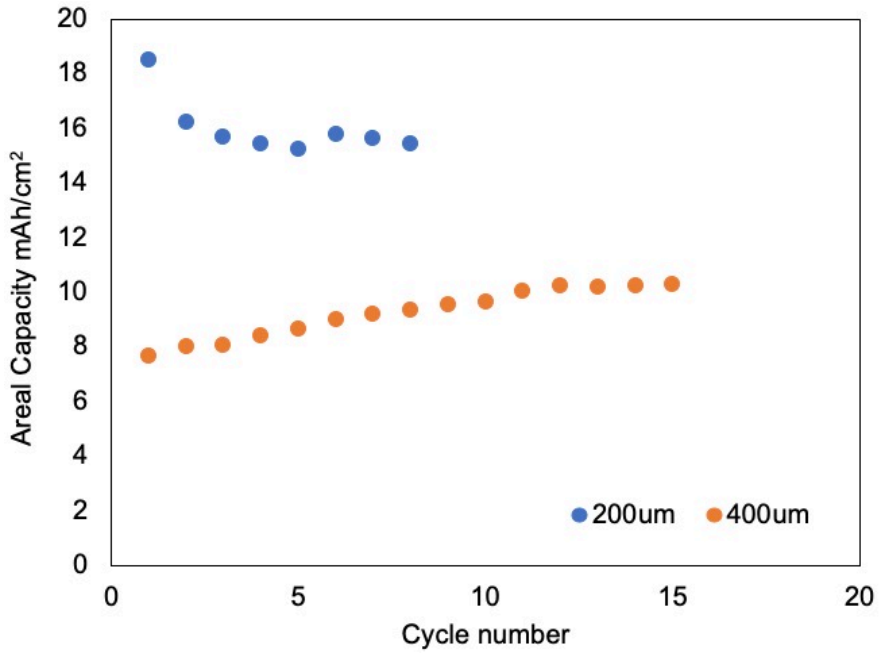

Figure 4. 7: Cycling of porous NiSn/Si composite using Cu substrates with different laser-machined hole sizes at 75mA/g

4.2. Electrodeposition of poly(phenylene oxide) (PPO) solid electrolyte

A solid electrolyte layer must ensure electronic insulation, but still allow ionic transport

between the cathode and anode networks [6]. Any pinholes on the electrolyte layer may potentially lead to contact between cathode and anode materials and shorting of the battery. Electro-polymerization of electrically insulating polymers enables self-limiting conformal growth until the entire electrochemically accessible surface is homogeneously covered, due to the propensity of deposition on previously uncoated areas [6]. Poly(phenylene oxide) (PPO) has attracted attention as a potential material for use as solid electrolyte since it is electrically insulating, conducts Li ions, and can be fabricated through self-limited electro-polymerization onto 2D/3D surfaces according to previous studies [6][7]. In this study, cyclic voltammetry is utilized to deposit PPO onto NiSn/Si composite [6][7]. In a cyclic voltammetry deposition, the potential is varied linearly as a function of time with scan rate v in both anodic and cathodic directions. Peaks in the voltammogram indicate that electrochemical reactions has reach a maximum rate and become mass transfer limited. Before depositing PPO onto the actual anode composite, evaporated gold is utilized as a model substrate to study the characteristics of PPO deposition. The composition of the deposition bath is listed below in Table 4.2. Note that tetrabutylammonium perchlorate (TBAP) is used as the supporting electrolyte, and tetramethylammonium hydroxide (TMAH) is used to make the bath with basic pH and therefore prevent the formation of side products [8].

Component	Concentration
Acetonitrile	Solvent
Tetrabutylammonium perchlorate (TBAP)	0.1M
Tetramethylammonium hydroxide (TMAH)	0.05M
Phenol	0.05M

Table 4. 2**:** Composition of PPO deposition bath

Figure 4.8 (a) shows the cyclic voltammogram of PPO deposition from 0 – 3V on an evaporated gold substrate. The counter electrode is Pt foil and the scan rate is 10 mV/s. The experiment is performed in a argon atmosphere glovebox. In the first cycle, a peak at 2.7V indicates PPO deposition. The current then rapidly drops after 2nd cycle and the peak is barely visible after 3rd cycle. In Figure 4.8 (b), the current at 3V dropped by three orders of magnitude after 40 cycles. This suggests that an electrically insulating layer is deposited on the substrate surface and therefore it is increasingly hard to deposit any thicker due to the growing impedance.

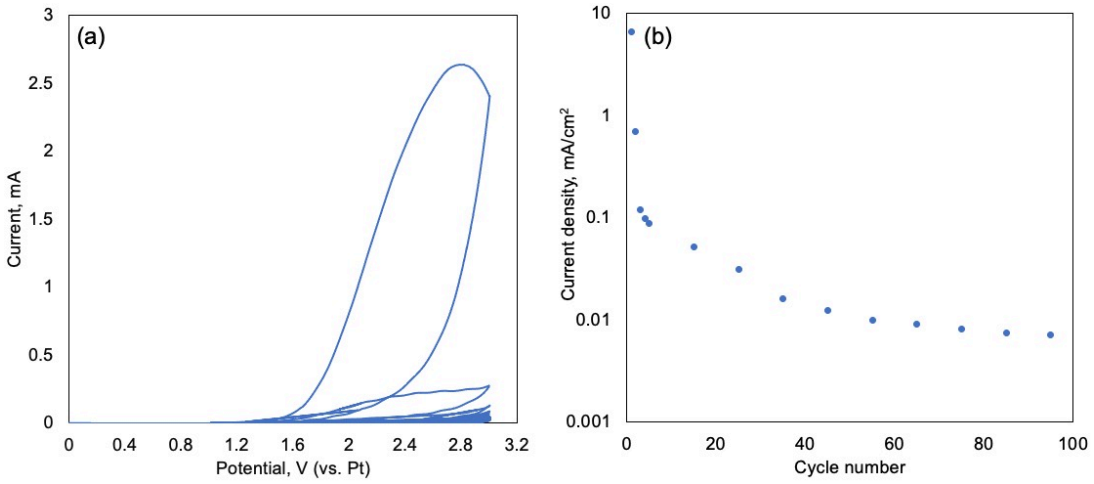

Figure 4. 8**:** (a) Cyclic voltammogram for PPO deposition on Au at 10 mV/s scan rate (b) Current at 3V as a function of cycle number

The deposited polymer film after 100 cycles is characterized using atomic force microscopy (AFM), which measures the film thickness by quantifying the interaction between the scanning probe and the sample surface. The inset of Figure 4.9 shows the topography map of the sample. The dark region on the top left corner is the bare gold. It

is protected by Kapton tape during PPO deposition, which is peeled off afterwards. The rest of the area with lighter color is covered with PPO film. As the probe scans diagonally across the separation line (as indicated by the white line in the inset image), there's jump in height about 30 nm, which is the PPO film thickness. This nanometer-scale film thickness allows fast ion transport between the cathode and the anode, even though the ionic conductivity of the PPO film is only on the order 10^{-10} S.cm^{-1} [7].

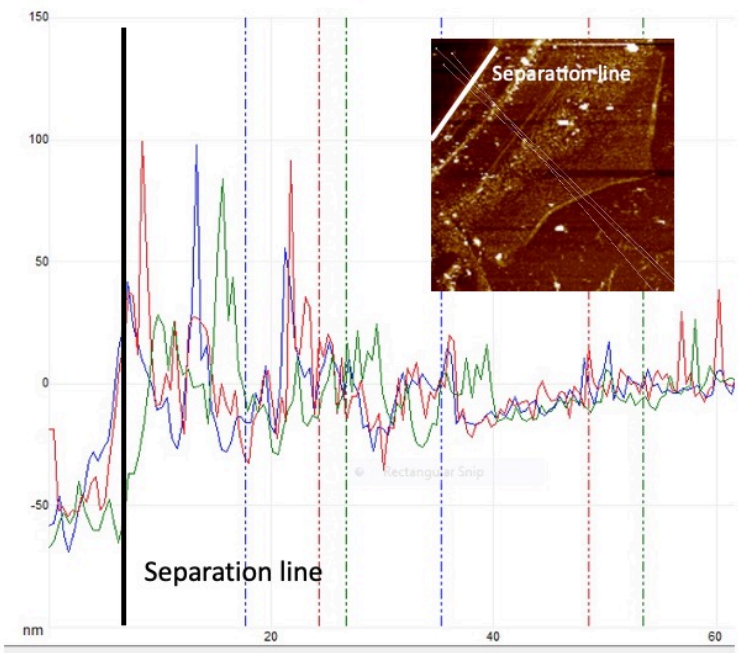

Figure 4. 9**:** AFM scanning for PPO deposited on the evaporated Au. X-axis in the distance along the scanning trajectory in nm while y-axis is the roughness of the sample surface in nm. The inset image shows the sample topography, where lighter shows higher altitude. The white separation line in the inset image corresponds to the black line in the main image

Since any pinholes on the film would cause shorting of the battery, techniques need to be developed to determine the coverage of PPO films. In this study, a hydroquinone redox

couple test is utilized [9]. In this test, a sample is immersed in 2mM hydroquinone aqueous solution containing phosphate buffer (pH = 7), and cyclic voltammetry is performed on the sample. If the sample surface is conductive, hydroquinone undergoes electrochemical oxidation/reduction as indicated by peaks on the CV curve, whereas if the sample surface is insulating, the electron conduction pathway is blocked, and no electrochemical reactions can occur.

In Figure 4.10, the gold substrate is cycled in the hydroquinone solution before and after PPO deposition. Pt is used as the counter electrode and Ag/AgCl in 3M KOH as the reference electrode. Two peaks can be observed in the voltammogram for the bare gold, indicating hydroquinone redox reactions occurred on Au. However, after PPO deposition, these peaks disappeared, and the current is effectively zero. This suggests that qualitatively, the Au surface is well covered with PPO polymer film.

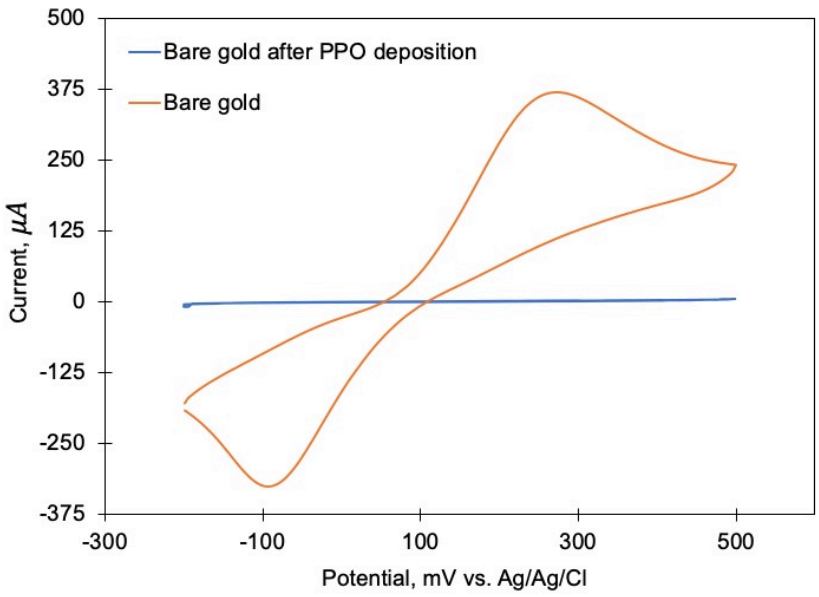

Figure 4. 10**:** Cyclic voltammogram of gold in 2mM hydroquinone before and after PPO deposition

Following the Au substrate model system, PPO is subsequently deposited on the porous NiSn/Si substrate. Initially, binder materials are not added, and a plain substrate with no laser-machined holes is utilized. Figure 4.11 (a) shows the cyclic voltammogram for PPO deposition on NiSn/Si composite at 10 mV/s using Pt as the counter electrode. As seen in (b), the current decays with cycle number, indicating deposition of an insulating layer of PPO polymer. The current dropped by two orders of magnitude after 300 cycles, which is less compared to the current drop for PPO deposition on gold. Widening the potential window will cause side reactions on the sample surface and interfere with the deposition process. This will be discussed in section 4.3.

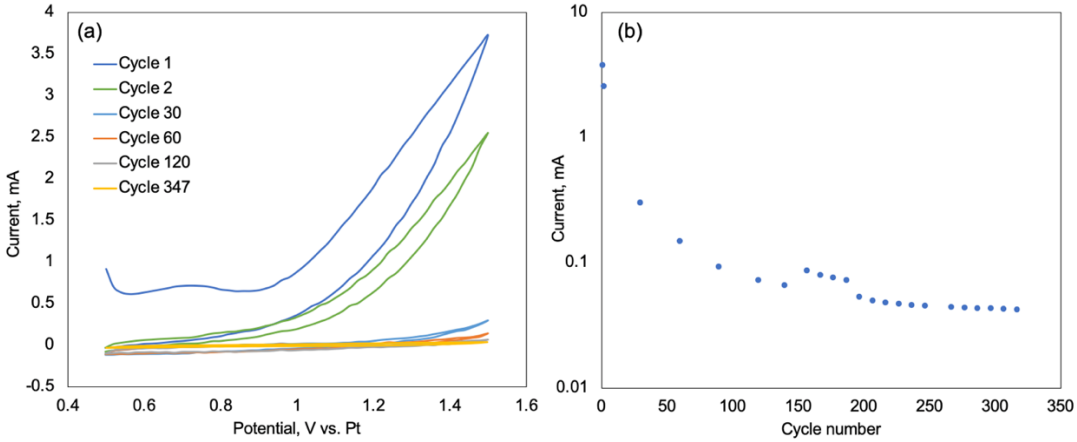

Figure 4. 11**:** (a) Cyclic voltammogram for PPO deposition on NiSn/Si at 10 mV/s scan rate (b) Current at 1.5V as a function of cycle number

Due to complex geometry of the composite and small thickness of the deposited polymer, it is hard to visually inspect the deposition. Thus, electrochemical methods are utilized for qualitative characterizations. Similar to PPO deposition on Au, porous NiSn is subjected to hydroquinone redox couple test. For bare porous NiSn/Si, there are no obvious peaks

for hydroquinone redox reactions, as shown in Figure 4.12 below. The current response at both ends of the voltammogram can be due to the onset of oxygen and hydrogen evolution, respectively. After PPO deposition, the current response decreases substantially, which suggests that the surface has been covered with a layer of insulating PPO film.

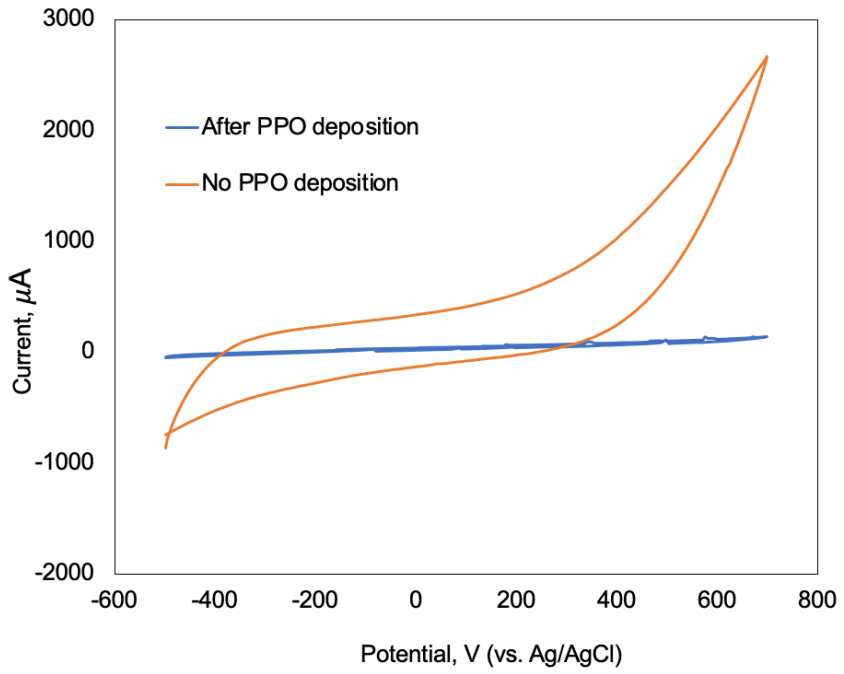

Figure 4. 12**:** Cyclic voltammogram of porous NiSn/Si in 2 mM hydroquinone before and after PPO deposition

In addition to the redox couple test, electrochemical impedance spectroscopy (EIS) is also used to characterize the deposition. In an EIS experiment, the electrode is perturbed with an alternating voltage of small amplitude around the equilibrium potential to observe the way in which the system follows the perturbation at steady state [10]. The electrode impedance is calculated from the current response. A Nyquist plot can be generated where y-axis is the imaginary part of the impedance and x-axis is the real part. Figure 4.13 shows

such a plot for two porous NiSn/Si samples, where one of them is deposited with PPO and the other is not. Both the counter and reference electrode for this test is Li foil and 1M $LiClO_4$ in 1:1 EC/DMC is used as the electrolyte. The sample with PPO deposition shows much higher impedance, which can be attributed to the insulating nature of the film that impedes charge transfer at the interface.

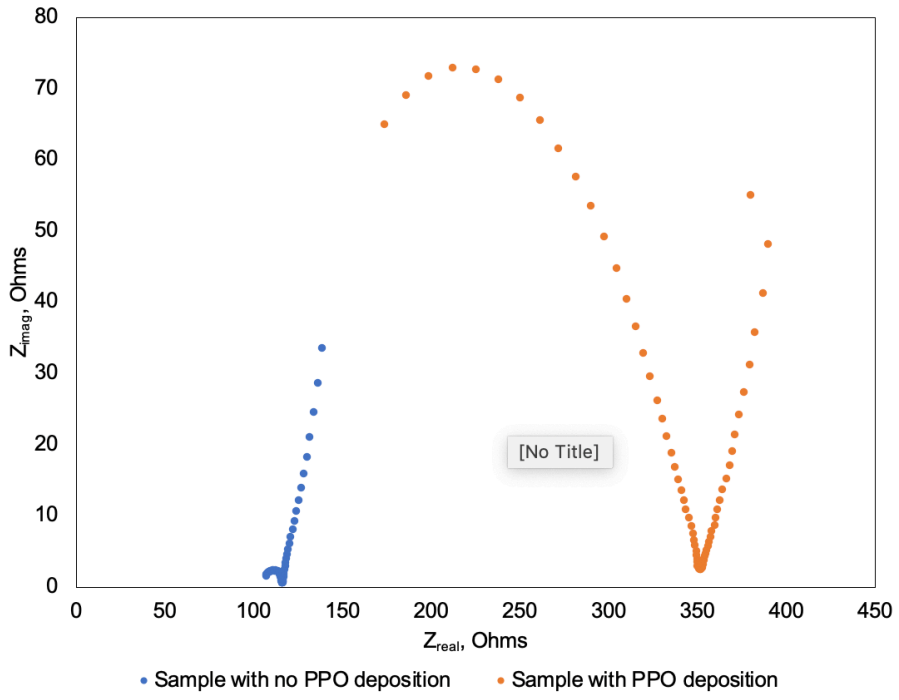

Figure 4. 13: Nyquist plot for samples with and without PPO deposition

4.3. Cathode preparation and full cell test

Following the polymer electrolyte deposition, a cathode slurry is cast onto the PPO-covered anode scaffold. Li_2S is chosen as the cathode material for this proof-of-concept study, as it possesses high specific capacity that can match high capacity of the anode. Using a mortar and pestle, the cathode slurry is made in an argon glovebox by mixing Li_2S powder, carbon conductives and polyvinylidene difluoride (PVDF) binder pre-dissolved in NMP.

The mass percentage of each component is listed in Table 4.3. Sample is placed in a glovebox until visually dry and then held in glovebox antechamber under vacuum overnight. Figure 4.14 shows the sample surface after cathode slurry dries. Note that for this proof-of-concept study, a relatively small amount of cathode material is added and the pores are not completely filled.

Chemical	Mass percentage
Li_2S	50%
Super P	10%
Graphene nanoplatelets	10%
Carbon nanofibers	10%
PVDF (40 mg/mL NMP)	20%

Table 4. 3**:** Mass composition for cathode slurry

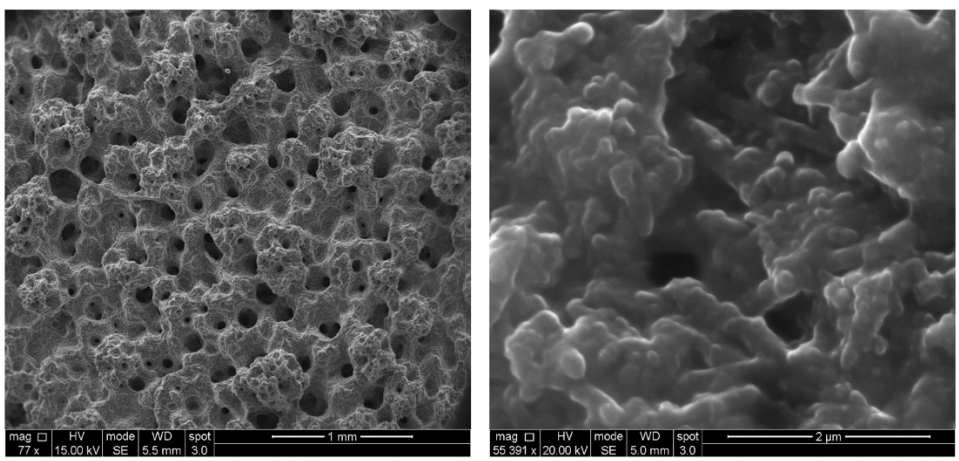

Figure 4. 14**:** SEM image of Li_2S cathode on PPO-covered NiSn/Si composite

Silver epoxy is then carefully applied onto the cathode surface with a copper wire buried within to make connections with external circuits. The sample is baked at 120℃ to harden

the silver epoxy. Due to the absence of an ion-conducting phase in the cathode, the full cell test is conducted in the liquid electrolyte to check whether the coverage of PPO is sufficient to serve as a polymer electrolyte/separator. The testing configuration is shown in Figure 4.15 (a), where the cell components, including the silver epoxy, are submerged in 1M LiTFSI in 1:1 DME/DOL with 1% $LiNO_3$. The copper wire at the cathode end and copper foil substrate at the anode end make electrical connections to the external circuit. Prior to cycling, OCV of the cell is approximately 0.2V. This indicates there is no shorting between the cathode and the anode. Figure 4.15 (b) shows the voltage profile of the full cell during cycling at 30 μA, which exhibits battery-like behavior instead of Ohmic behavior. The abrupt change in potential at the end of the cycling is due to softening of the silver epoxy in ether-based electrolyte that weakens the electrical conduction. In spite of incomplete cell cycling, a functional full cell with a nanometer level layer of PPO polymer electrolyte that separates the cathode and the anode is demonstrated.

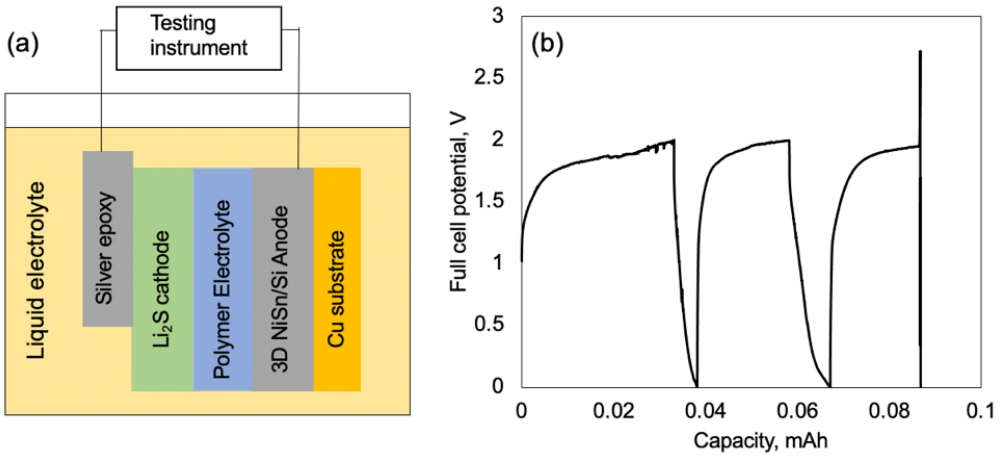

Figure 4. 15: (a) Li_2S/PPO/NiSn/Si full cell testing configuration (b) Li_2S/PPO/NiSn/Si full cell potential profile

4.4. Further investigation of PPO deposition on different metals

Although some non-shorting, functional full cells are demonstrated, the results are not highly reproducible, mostly due to shorting of the battery. As shown in Figure 4.11, no peak for PPO deposition appears in the cyclic voltammogram. This suggests that although the current decreases with cycle number, PPO deposition rate did not reach the maximum rate, and this may result in incomplete coverage. Thus, PPO deposition behavior on the anode scaffold are further investigated. To simply the complex system, only the deposition onto the metal parts are investigated, including Ni, Sn, and Cu substrate.

In order to completely cover the porous NiSn, all metal parts on the sample, including Ni, Sn, and Cu, have to be covered with pin-hole free PPO. Thus, the deposition behavior of PPO will be first studied on individual metal foils using cyclic voltammetry. In order to have better control over the potential window, a polished silver wire is used as the reference electrode and Pt is used as the counter electrode.

Figure 4.16 shows the cyclic voltammogram profile and the hydroquinone test results for PPO deposition on Cu, Ni, and Sn metal foils after 3 cycles. For both Cu and Ni, at about 0.75V versus the. Ag reference electrode, a peak appears in the voltammogram, which indicates the deposition reaches mass transfer limitations. The hydroquinone results for Cu and Ni both show a much reduced current signal after PPO deposition. Note that as shown in Figure 4.16 (e), the hydroquinone redox reaction does not occur until 0.9V vs. Ag/AgCl, where there is significant oxygen evolution. However, the hydroquinone redox peak disappeared for the sample with 3 cycles of PPO deposition using 0.8V as the upper

potential. The remaining current signal may be due to migration of hydroxide ions into the PPO film. For Sn, as shown in Figure 4.16 (c) the current on the reverse scan becomes larger than that during the forward scan when using 0.8V as the upper end potential, which is not observed in previous trials. The hydroquinone test shows much reduced signal after PPO deposition in Figure 4.16 (f).

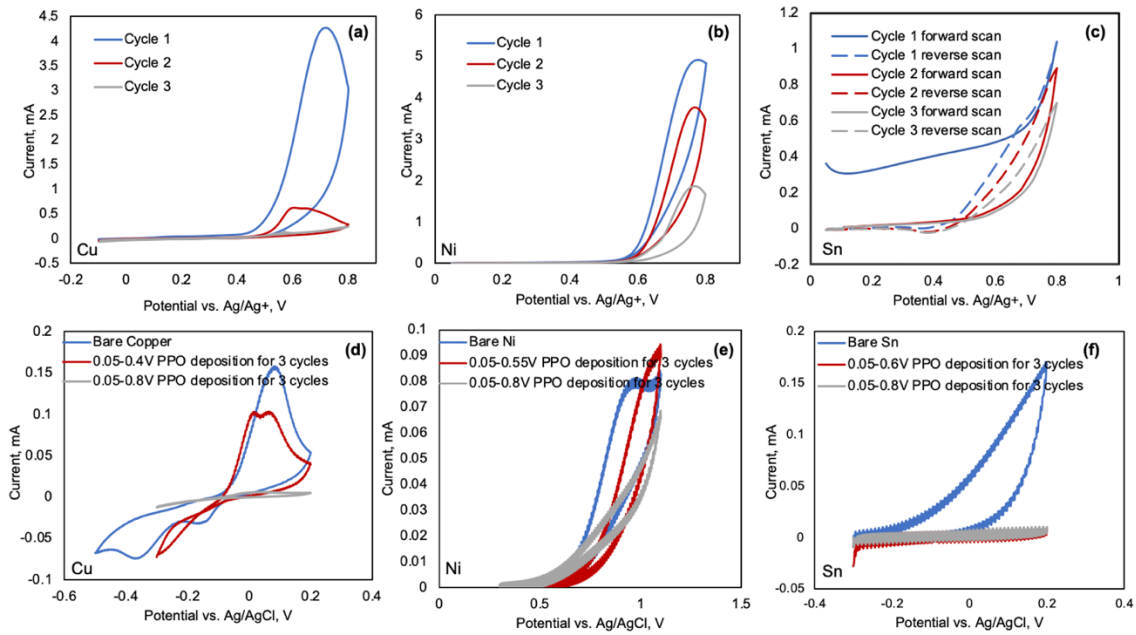

Figure 4. 16**:** (a)(b)(c) Cyclic voltammogram of 3-cycle PPO deposition on Cu, Ni, and Sn using 0.8V vs. Ag reference electrode as the upper potential (d)(e)(f) Hydroquinone test for PPO deposition on Cu, Ni, and Sn

In Figure 4.17, when extending the upper voltage to 1.2V for PPO deposition on Sn, a peak occurred during the reverse scan, and white, flocculus debris is observed simultaneously on the sample surface. The second cycle current abnormally increases compared to the first cycle, which indicates the occurrence of side reactions. Such side reactions may be caused

by catalytic capabilities of Sn in organic solutions [11-12].

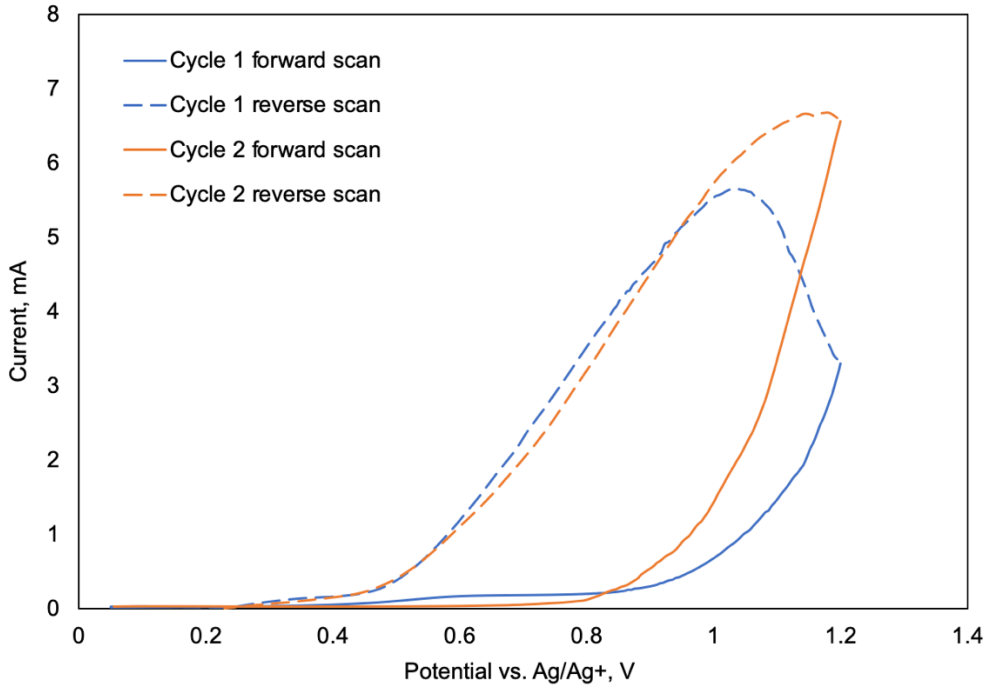

Figure 4. 17**:** Cyclic voltammogram of 2-cycle PPO deposition Sn using 1.2V vs. Ag reference electrode as the upper potential

Figure 4.18 (a) illustrates the cyclic voltammogram deposition of PPO on porous NiSn with Cu substrate. The upper voltage increases with the cycle number until a peak appears in cycle 10, after which the upper end potential is held at 1.1V. The current starts to increase with cycle number since then, similar to Figure 4.17 above. In addition, flocculus deposit appears on the sample surface as shown in Figure 4.18 (b). The sample is subjected to hydroquinone test before and after PPO deposition. Although there is a much reduced current signal after 120 cycles of PPO deposition, the cell still shorts during full cell test as described in section 4.2. The side product deposits, whose formation is likely catalyzed by

Sn, may have interfered with the PPO deposition process and resulted in subsequent increase in current with cycle number. Thus, a more stable solvent system or additives that could expand the stability window might help with the deposition process. In addition, more reliable testing methods other than the redox couple test need to be developed to check pinhole-free PPO deposition has occurred.

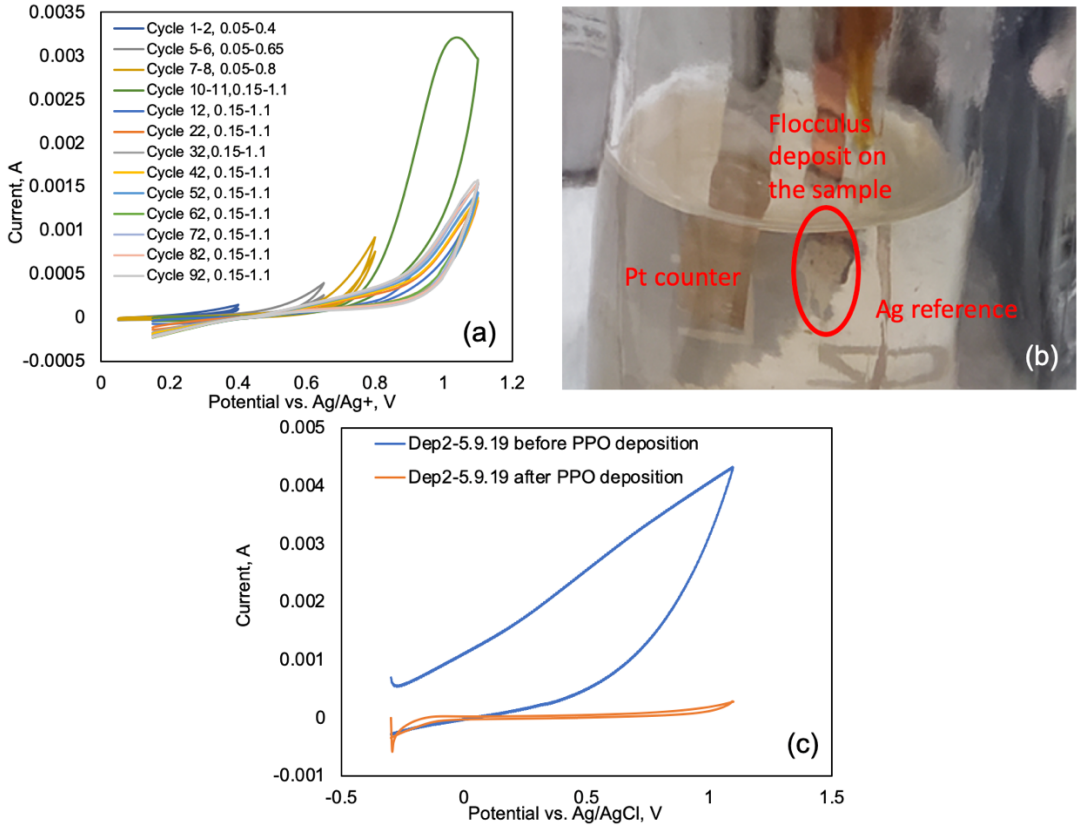

Figure 4. 18**:** (a) Cyclic voltammogram of PPO deposition on porous NiSn using progressively increasing voltage windows (b) Side product formation on the sample surface (c) Hydroquinone test before and after PPO deposition on the porous NiSn/Si sample

4.5. Conclusions

In this chapter, the fabrication of a monolithic piece of Li-ion microbattery is demonstrated. A poorous NiSn/Si scaffold is deposited using hydrogen-templated electrodeposition method, with the 3D structure growing through Si particles. Owing to high specific capacity of NiSn and Si materials, the electrode can achieve an ultrahigh areal capacity of 40 mAh/cm^2. With the incorporation of PAA binder materials, the cycling performance can be stabilized. In addition, the utilization of laser fabricated holes on the Cu substrates decreases the mass and charge transport resistance and allows higher capacity utilization to be achieved. An ultrathin layer of poly(phenylene oxide) (PPO) polymer electrolyte is deposited electrochemically onto the porous electrode using cyclic voltammetry. Coverage of the PPO is shown qualitatively using redox couple test and impedance spectroscopy. A full cell test is conducted following infiltration of the Li_2S cathode material, and functional proof-of-concept full cell is demonstrated. Further investigations of PPO deposition are conducted to better understand the deposition mechanism on the porous NiSn composite. It is concluded that side reaction products catalyzed by Sn in the composite may have interfered with PPO deposition at high upper end potential limits. In addition, more reliable testing methods other than the redox couple test are needed to determine whether pinhole free PPO deposition has occurred.

4.6. Reference

1. Komaba, S., Shimomura, K., Yabuuchi, N., Ozeki, T., Yui, H., & Konno, K. (2011). Study on polymer binders for high-capacity SiO negative electrode of Li-ion batteries. *The Journal of Physical Chemistry C*, *115*(27), 13487-13495.
2. Kwon, T. W., Choi, J. W., & Coskun, A. (2018). The emerging era of supramolecular polymeric binders in silicon anodes. *Chemical Society Reviews*, *47*(6), 2145-2164.
3. Magasinski, A., Zdyrko, B., Kovalenko, I., Hertzberg, B., Burtovyy, R., Huebner, C. F., ... & Yushin, G. (2010). Toward efficient binders for Li-ion battery Si-based anodes: polyacrylic acid. *ACS applied materials & interfaces*, *2*(11), 3004-3010.
4. Higgins, T. M., Park, S. H., King, P. J., Zhang, C., McEvoy, N., Berner, N. C., ... & Nicolosi, V. (2016). A commercial conducting polymer as both binder and conductive additive for silicon nanoparticle-based lithium-ion battery negative electrodes. *Acs Nano*, *10*(3), 3702-3713.
5. Pharr, M., Suo, Z., & Vlassak, J. J. (2014). Variation of stress with charging rate due to strain-rate sensitivity of silicon electrodes of Li-ion batteries. *Journal of Power Sources*, *270*, 569-575.
6. Werner, J. G., Rodríguez-Calero, G. G., Abruña, H. D., & Wiesner, U. (2018). Block copolymer derived 3-D interpenetrating multifunctional gyroidal nanohybrids for electrical energy storage. *Energy & Environmental Science*, *11*(5), 1261-1270.
7. Rhodes, C. P., Long, J. W., Doescher, M. S., Fontanella, J. J., & Rolison, D. R. (2004). Nanoscale polymer electrolytes: ultrathin electrodeposited poly (phenylene oxide) with solid-state ionic conductivity. *The Journal of Physical Chemistry B*, *108*(35), 13079-13087.
8. Bruno, F., Pham, M. C., & Dubois, J. E. (1977). Polaromicrotribometric study of polyphenylene oxide film formation on metal electrodes by electrolysis of disubstituted phenols. *Electrochimica Acta*, *22*(4), 451-457.
9. Sun, B., Rehnlund, D., Lacey, M. J., & Brandell, D. (2014). Electrodeposition of thin poly (propylene glycol) acrylate electrolytes on 3D-nanopillar electrodes. *Electrochimica Acta*, *137*, 320-327.

10. Allen, J. B., & Larry, R. F. (2001). *Electrochemical methods fundamentals and applications*. Hoboken: John Wiley & Sons.
11. Jiang, L., Sun, G., Sun, S., Liu, J., Tang, S., Li, H., ... & Xin, Q. (2005). Structure and chemical composition of supported Pt–Sn electrocatalysts for ethanol oxidation. *Electrochimica Acta*, *50*(27), 5384-5389.
12. Andrew, M. R., Drury, J. S., McNicol, B. D., Pinnington, C., & Short, R. T. (1976). The characterization of Pt/Sn catalyst for the electrochemical oxidation of methanol. *Journal of Applied Electrochemistry*, *6*(2), 99-106.

CHAPTER 5: MODEL-ASSISTED DESIGN OF ELECTRODE STRUCTURES

The development of an electrochemical model for a 3D micro-battery system will aid in the understanding of how electrode architecture and materials affect the physical processes that limit energy density, power density, and cycle life. Once the model is validated against experimental data, it can be used to optimize the design of the 3D electrodes and guide the fabrication processes to enable high energy and power density applications. Herein, a rationally designed and deterministically engineered 3D $Ni(OH)_2$ cathode for NiZn battery applications was used as a preliminary study, as the well-defined geometry of these electrodes allows easier implementation of the mathematical models for the optimization of their characteristic dimensions, as well as for performance projections. Well-defined geometries provide insights on exactly how various parameters could affect electrode performance and help design better electrodes in future studies. This model may be extended to the more complex porous electrodes that are fabricated experimentally in Chapter 2 – 4 based on similar mass/charge transport and reaction kinetics principles as developed here.

5.1. Fabrication of 3D $Ni(OH)_2$ electrode model system

This study involves rationally designed and deterministically engineered 3D structures that resulted in high-power capability. A series of fabrication methods encompassing electrochemical techniques and microfabrication technologies have been utilized for the formation and characterization of the scalable, well-ordered, and high-surface-area 3D architectures that can be potentially used as high-power electrodes in a variety of

applications, ranging from autonomous microsystems to macroscale portable electronics. $Ni(OH)_2$, one of the most well-studied active material in secondary (i.e., rechargeable) battery systems [1] , was chosen in this study as the energy storage material. Fabrication and electrochemical characterization of the 3D electrode will be detailed as follows.

5.1.1. 3D $Ni(OH)_2$ electrode fabrication

The electrodes are based on the anchor-supported lateral high-aspect-ratio structures whose fabrication process was schematically illustrated in Figure 5.1. In summary, a photoresist mold was patterned and developed on a metalized glass substrate. Next, alternating Ni and Cu layers were deposited by electroplating in a well-controlled and systematic fashion using an automated robotic plating setup. Following the electroplating of the multilayer structure, the photoresist mold was stripped, and a second photoresist film was formed, which served as the mold for electroplating of thick Ni anchors on specific regions of the sidewalls of the multilayer structures. Thereafter, sacrificial Cu layers were selectively etched resulting in a high-surface-area multilayer Ni backbone. Finally, $Ni(OH)_2$ was electrodeposited onto the Ni backbone in a conformal fashion. Figure 5.2 shows the SEM images of the sidewall of the multilayer structure before and after active material deposition.

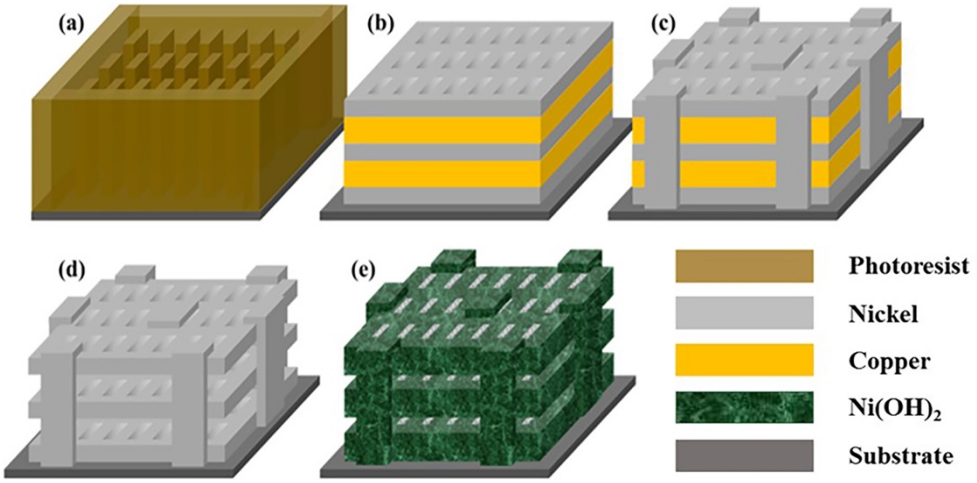

Figure 5. 1**:** Schematic illustration of the fabrication process for the $Ni(OH)_2$-based electrodes: **(a)** Deposition of UV-patterned photoresist mold onto a metallized glass substrate, **(b)** robot-assisted electroplating of alternating Ni and Cu layers followed by the removal of the photoresist, **(c)** electroplating of the Ni anchors through a second photoresist mold, **(d)** selective etching of the sacrificial Cu layers, and **(e)** electrodeposition of the $Ni(OH)_2$ onto the multilayer Ni backbone.

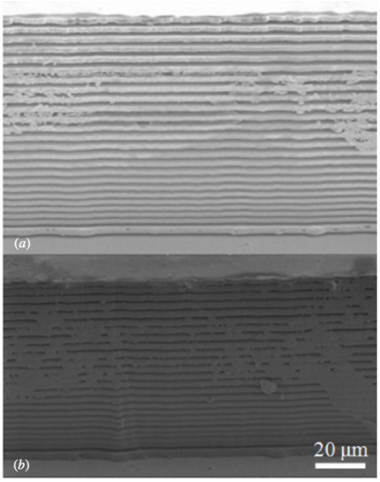

Figure 5. 2**:** SEM images of the sidewall of the multilayer structure: (a) before and (b) after active material deposition [2].

5.1.2. 3D $Ni(OH)_2$ electrode characterization and experimental performance

A multilayers $Ni(OH)_2$/Ni structure composed of 100 layers was prepared using methods described in section 5.1.1. For the characterization of the $Ni(OH)_2$ electrodes, a three-electrode-cell configuration was used, in which a platinum mesh and an Ag/AgCl electrode were utilized as the counter and reference electrodes, respectively. All of the charging/discharging experiments were conducted galvanostatically at various rates ranging from 1C to 150C in 6M KOH electrolyte with the aid of a potentiostat (WaveDriver 10, Pine Instruments). Here the x C rate is defined as the charge/discharge current will charge/discharge the entire battery in x^{-1} hours.

Discharge profiles of a 100-layer electrode with respect to its capacity are presented in Figure 5.3 (a). Respective charge and discharge rates of 20C and 10C are applied for over 80 cycles, and profiles of six representative cycles are plotted. These profiles are in good agreement with those of $Ni(OH)_2$ electrodes reported previously in the literature [3-4]. The measured capacity of 2.43 mAh cm^{-2} after the 30th cycle is found to drop to 2.02 mAh cm^{-2} after the 80th cycle, which corresponds to a significant capacity retention of 83% even at these high charge and discharge rates. The realization of this high-power capability can be attributed to a thin and conformal active material coating on each Ni layer, which reduces the diffusion and conduction path lengths for the solid-state ions and electrons, respectively. In addition, the high electronic conductivity of Ni backbone minimizes resistance for the transfer of electrons to and from the active material.

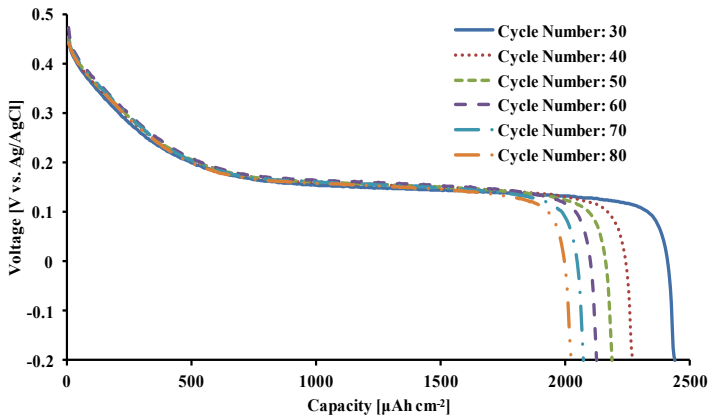

Figure 5. 3**:** Discharge profiles of a 100-layer electrode charged at 20C and discharged at 10C for over 80 cycles

5.2. Mathematical modeling of 3D $Ni(OH)_2$ electrode

A mathematical model relying on fundamental mass transport and reaction kinetics principles has been developed to optimize the characteristic dimensions of the multilayer electrodes suitable for high-power batteries.

5.2.1. Model description

The model was assembled using COMSOL 5.2 Multiphysics Software. Since a 2D model is able to capture most of the essential features of the multilayer structure, we chose to model in 2D instead of 3D to reduce computation time. A repeating unit of the multilayer electrode was defined as shown in Figure 5.4. Note that a 30-layer structure is shown for clarity of individual layers; additional layers can easily be incorporated in the actual model. Width L corresponds to the distance between the adjacent etching holes (i.e., from point a to b in Figure 5.4 (a)). The lower limit of this width was determined by the design of the lithographic photomask that was used during the photolithography process, and its flexibility was limited due to constraints pertaining to the fabrication of the photoresist

mold (i.e., AZ 125 nXT) prior to the automated electroplating process. Designs that have densely packed etching holes, i.e., L<<300 µm, require a dense packing of the photoresist pillars, which complicates the fabrication process. Therefore, an experimentally fabricated structure with a pillar size of 150 x 600 μm^2 and a spacing L of 300 µm was selected for the modeling purposes.

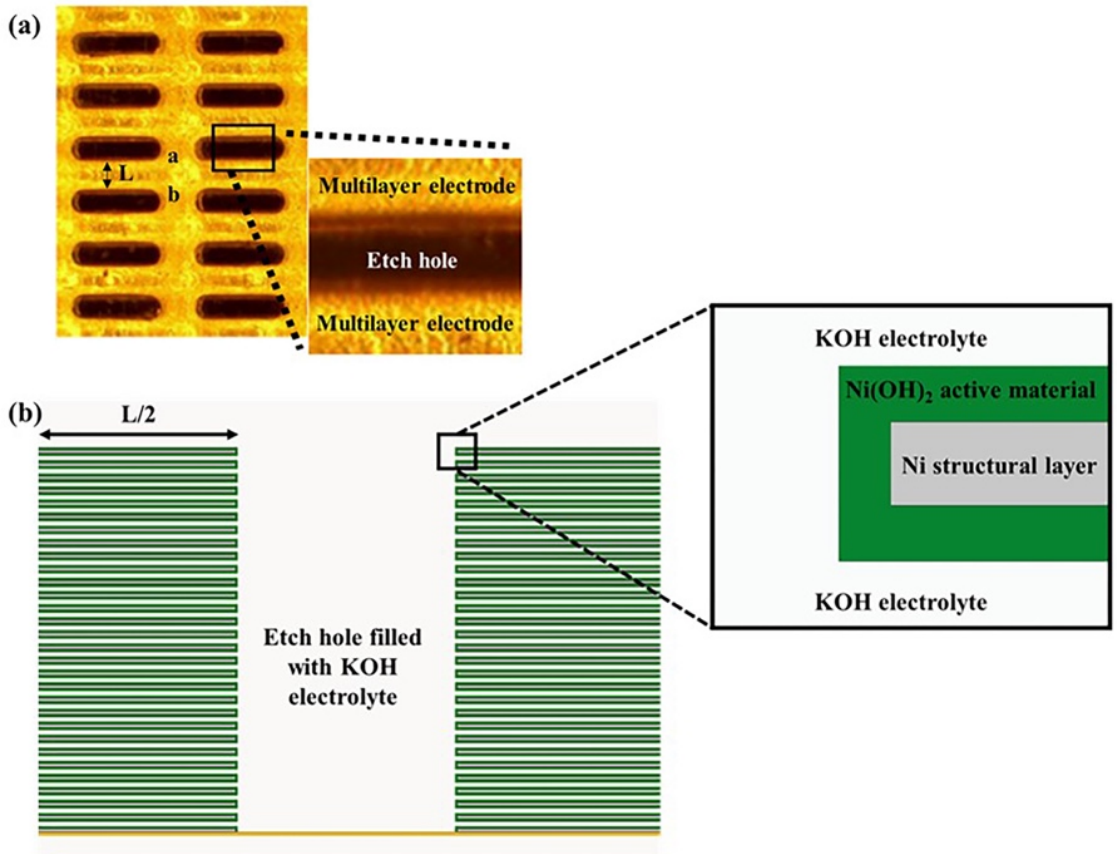

Figure 5. 4**: (a)** Optical images showing a section from the top view of the fabricated multilayer electrode along with its etching holes, **(b)** schematic illustration showing the cross-section of the multilayer electrode for the COMSOL tertiary current distribution interface, with the inset showing a single layer.

The tertiary current distribution interface in COMSOL 5.2, which takes into account the effect of variations in electrolyte composition and ionic strength on the charging and

discharging process, was used to calculate the ion concentration distribution in both the liquid and solid phases. The COMSOL partial differential equation interface was used to model the proton diffusion within the $Ni(OH)_2$ active material. In addition, although the electrochemical characterizations in the experimental work were carried out in a three-electrode set-up, where Pt electrode and Ag/AgCl electrode served as the counter electrode and the reference electrode, respectively, the model assumed a two-electrode configuration for simplicity in modeling. In principle, this should not affect performance predictions of the $Ni(OH)_2$ multilayer half-cell, which is the main focus of this this study.

$Ni(OH)_2$ chemistry exhibits a reversible charge storage redox mechanism in which it converts to nickel oxyhydroxide (NiOOH) via diffusion of protons through its solid state lattices. The electrochemical reactions occurring at the $Ni(OH)_2$ cathode/electrolyte interface are given by:

$$Ni(OH)_2 + OH^- \underset{\text{Charging}}{\overset{\text{Discharging}}{\leftrightharpoons}} NiOOH + H_2O + e^- \quad (1)$$

$$2OH^- \underset{\text{Charging}}{\overset{\text{Discharging}}{\leftrightharpoons}} 0.5O_2 + H_2O + 2e^- \quad (2)$$

The Zn counter electrode reactions are as follows:

$$Zn + 4OH^- \underset{\text{Discharging}}{\overset{\text{Charging}}{\leftrightharpoons}} Zn(OH)_4^{2-} + 2e^- \quad (3)$$

$$2OH^- \underset{\text{Discharging}}{\overset{\text{Charging}}{\leftrightharpoons}} 0.5O_2 + H_2O + 2e^- \quad (4)$$

Proton diffusion to and from the bulk of the active material enables reaction (1) to continue at the interface. Reaction (2) refers to the oxygen evolution side reaction during electrode

overcharging. Inclusion of this reaction mechanism is necessary because it is fueled by part of the current used to charge the electrode, thus decreasing the capacity retention [5-6]. Reaction (3) refers to the zinc reaction at the anode. Since the focus of this study is on performance of the $Ni(OH)_2$ cathode, the concentration of $Zn(OH)_4^{2-}$ and its conversion to ZnO were not taken into account in the model.

Note that although the OH^- ions are produced from the zinc reaction at the anode during charging, which may potentially deviate from the actual three-electrode scenario, the simulation results, which focused on capacity retention of the $Ni(OH)_2$ cathode, should still be valid as long as the cathode is set sufficiently far away from the Zn counter electrode such that semi-infinite condition for the potassium hydroxide (KOH) electrolyte diffusion is satisfied.

The reaction rates for the electrochemical reactions involved in NiZn cell can be described by Equations (5) – (8), using either Butler-Volmer equations or the anodic Tafel equation with respect to a specific reference state [5-9]:

$$i_{loc,1} = i_{01,ref}\big((C_{OH}/C_{OH,ref})(C_H/C_{H,ref})\exp(\alpha_{a1}F\eta_1/RT) - ((C_{H,max} - C_H)/(C_{H,max} - C_{H,ref}))\exp(-\alpha_{c1}F\eta_1/RT)\big) \quad (5)$$

$$i_{loc,2} = i_{02,ref}(C_{OH}/C_{OH,ref})^2 \exp(\eta_2/b_{oer}) \quad (6)$$

$$i_{loc,3} = i_{03,ref}(\exp(\alpha_{a3}F\eta_3/RT) - \exp(-\alpha_{c3}F\eta_3/RT)) \quad (7)$$

$$i_{loc,4} = i_{04,ref}\left(\left(C_{OH}/C_{OH,ref}\right)^2 \exp(\alpha_{a4}F\eta_4/RT) - (C_{O_2}/C_{O_2,ref})\exp(-\alpha_{c4}F\eta_4/RT)\right) \quad (8)$$

The local reaction rates of Reaction (1), Reaction (2), Reaction (3), and Reaction (4) are given as $i_{loc,1}$, $i_{loc,2}$, $i_{loc,3}$, and $i_{loc,4}$, respectively. C_m [mol cm^{-3}] and $C_{m,ref}$ [mol cm^{-3}] denote the local concentration and the reference concentration of the corresponding species m, respectively. In Equation (5), $C_{H,max}$ [mol cm^{-3}] is the proton concentration of $Ni(OH)_2$ in a fully discharged state and is calculated by dividing the density of Ni(OH)2 (3.55 g cm^{-3}) by its molecular weight (92.71 g mol^{-1}), yielding a value of 0.0383 mol cm^{-3}. Note that the volumetric change of the active material owing to the difference between the density of the charged and discharged state, was neglected. $i_{0j,ref}$ is the exchange current density evaluated at the reference conditions (where $C_H = C_{H,ref}$, $C_{OH} = C_{OH,ref}$, and $C_{O2} = C_{O2,ref}$); b_{oer}[V] is the Tafel slope for oxygen evolution reaction at the cathode; α_{aj} and α_{cj} are the anodic and cathodic charge transfer numbers of jth reaction, respectively. Note that $i_{04,ref}$, α_{a4}, and α_{c4} on Zn were assumed to be the same as those on Cd; these parameters had minimal effects on capacity retention calculations of the nickel hydroxide cathode. F [C mol^{-1}] is the Faraday's constant; R [J mol^{-1} K^{-1}] is the gas constant, and T [K] is the absolute temperature. The over-potential η_j [V] is defined by:

$$\eta_j = \phi_s - \phi_l - U_{j,ref} \quad (9)$$

where ϕ_s [V] is the electric potential of the solid phase; ϕ_l [V] is the electrolyte potential; $U_{j,ref}$[V] is the equilibrium potential at the reference condition.

Within the active material, the diffusion of the protons is dictated by Fick's second law:

$$\frac{\partial C_H}{\partial t} = D_H \nabla^2 C_H \tag{10}$$

where D_H [cm^2 s^{-1}] is the proton diffusion coefficient. For the purposes of this model, the charging is assumed to take place under isothermal conditions at room temperature. Previous studies by Paxton and Newman [10], and more recently by Gu et al. [8] indicate that the diffusion coefficient value can be approximated as a constant for diffusion lengths smaller than 3 μm, which is also the case in the present study. Thus, despite the fact that the diffusion coefficient of the protons depends on the state of charge (SOC) of the active material [11], a constant value is assumed for D_H throughout charging of the electrode. A wide range of values from 10^{-12} to 10^{-8} [cm^2 s^{-1}] have been reported for the $Ni(OH)_2$-based electrodes, which, in addition to SOC, reportedly are also dependent on the synthesis methods and measurement techniques [10][12-13].

Herein, we measured the average diffusion coefficient of our electrodeposited active material over all states of charge by utilizing cyclic voltammetry (CV), which was shown to yield reliable results in other studies [14-17]. Specific description of the experimental procedure will be detailed in 5.3.1.

At the active material-electrolyte interface (at x = L), the proton flux is proportional to the nickel hydroxide reaction rate (Reaction (1)). At the interface of the active material and the Ni current collector (at x = 0), since no mass transfer is taking place, the flux equals

zero. Taking these assumptions into account, the initial and boundary conditions for the model can be written as:

At x = L:

$$D_H \frac{\partial C_H}{\partial x} = -\, i_{loc,1}/F \tag{11}$$

At x = 0:

$$D_H \frac{\partial C_H}{\partial x} = 0 \tag{12}$$

At t = 0

$$C_H = C_{H,max} \tag{13}$$

The electron conduction within all solid phases is given by Ohm's law and the conservation of current:

$$i_s = -\sigma_s \nabla \phi_s \tag{14}$$

$$\nabla . i_s = 0 \tag{15}$$

where i_s [A cm^{-2}] is the local current density within the solid phase; σ_s [S cm^{-1}] is the electrical conductivity of the solid; ϕ_s[V] is the electric potential in the solid phase.

The transport of the ionic species within the liquid electrolyte is dictated by the Nernst-Planck equation:

$$\frac{\partial C_m}{\partial t} = \nabla \cdot \left((D_m \nabla C_m) + z_m u_m F C_m \nabla \phi_l \right) \tag{16}$$

$$i_l = F\sum_m z_m(-D_m\nabla C_m - z_m u_m F C_m \nabla\phi_l) \tag{17}$$

$$u_m = D_m/(k_B T) \tag{18}$$

where m = K^+ and OH^- ; i_l[A cm^{-2}] is the local current in the KOH electrolyte; ϕ_l[V] is the electrolyte potential; D_m[cm^2 s^{-1}] is the diffusion coefficient of ionic species within the KOH electrolyte; z_m is the charge number of the ionic species; u_m [s kg^{-1}] is the mobility of the charge species; k_B [J K^{-1}] is the Boltzmann's constant. In Equations (17) and (18), the interactions between KOH solutes are neglected, and thus the activity gradients are assumed to be equal to the concentration gradients. In addition, natural convection due to local electrolyte density variations is ignored in this model.

Electro-neutrality is assumed to be maintained throughout the solution at all times:

$$\sum_m z_m C_m = 0 \tag{19}$$

The capacity retention τ of the electrode at a given charge rate is defined as:

$$\tau = \int_{\text{Electrode area}} \left(\oiint i_{loc,1} dS \right) dt/(F C_{H,max} V) \tag{20}$$

where t [s] is the charge time; S [cm^2] is the electrode active area; V [cm^3] is the volume of the active material. The integration is first performed over the entire electrode/electrolyte interface and then over time.

5.2.2. Comparison with experimental data

To determine whether the model can successfully predict the performance of the fabricated electrodes, the cycling performance of the 100-layer electrode is assessed by varying charging rates to generate the data for model validation. For a constant discharge rate of 4C, the electrode is charged at 8 different rates, as shown in Figure 5.5 below. More than 80 charge and discharge cycles are conducted, and the average capacity retention at each rate is used as the value for comparison with experimental data.

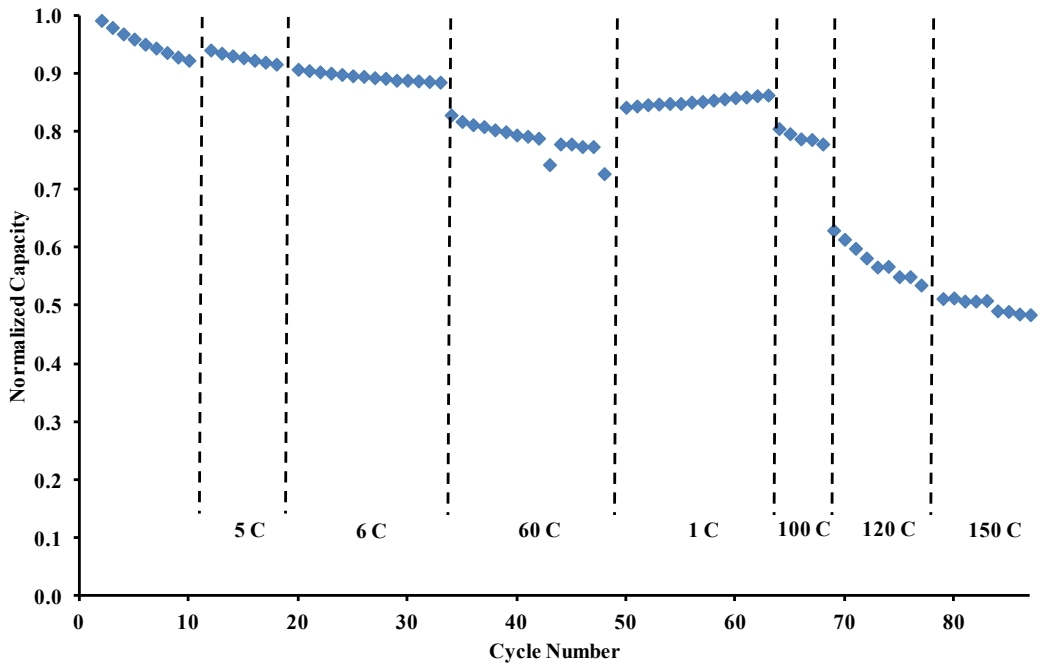

Figure 5. 5**:** Normalized capacity of a 100-layer electrode charged at various rates (1 to 150C) and discharged at a constant rate of 4C for over 80 cycles.

Capacity retention calculations (Equation (20)) are then performed using the model described earlier, based on experimental dimensions of the aforementioned 100-layer structure: 1 μm for active material thickness, 2 μm for interlayer spacing, and 1.5 μm for

Ni structural layer. The mathematical model requires a number of physical properties. These parameters can be found in [18].

As can be seen in Figure 5.6, the theoretical results obtained from the model agree with the experimental results. This agreement between the experimental and the modeling results indicates that the model can be employed to optimize the design of multilayer electrodes for rapid charge and discharge power applications.

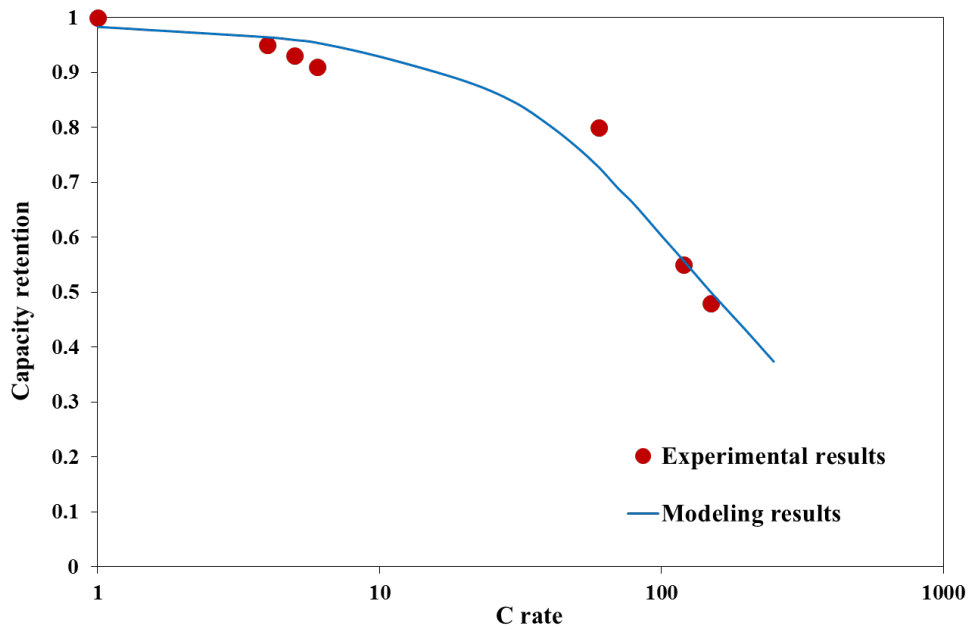

Figure 5. 6: Experimental vs. model capacity retention of a 100-layer electrode with 1.5 µm Ni structural layer, 1 µm $Ni(OH)_2$ on each side of a single Ni layer, and 2 µm interlayer spacing at various charge rates.

Note that, as mentioned previously, a key model input parameter is the diffusion coefficient of protons within the $Ni(OH)_2$ active material, D_H. In the model, a best-fit value of 3.4×10^{-10} cm^2 s^{-1} is used for D_H. Repeated cyclic voltammetry measurements show that the experimental diffusion coefficient value ranges from 2×10^{-10} cm^2 s^{-1} to 3×10^{-10} cm^2 s^{-1}.

Since the best-fit value from the mathematical model is close to the experimentally measured value and a constant average diffusion coefficient could be used as previous studies suggest, we are justified in using the best-fit value for the model.

5.2.3. Electrode design optimizations

One of the main motivations of this modeling study is the ability to optimize the characteristic dimensions, such as the surface area and the active material thickness, of the fabricated electrodes to enhanced power performance. As mentioned in Chapter 1, maximization of the surface area, along with the minimization of the diffusion and conduction path lengths, would lead to electrodes with high capacity and rapid charging capabilities. In the multilayer fabrication approach, the surface area maximization can be achieved by increasing the number of layers, as well as by decreasing the interlayer spacing and Ni structural layer thickness. Thus, two geometrical parameters are considered in this optimization study in order to maximize the surface area: the interlayer spacing between two active material layers and the thickness of the Ni structural layer. However, the minimization of the diffusion and conduction paths, which enables high charge rates, has to be achieved at the expense of energy density, due to decreased active material thickness relative to the thickness of the Ni structural layer. Consequently, the optimum active material thickness used for the multilayer structure depends on the specific application scenario.

Figure 5.7 shows the relationship between energy/power density and interlayer spacing for a fixed total height of 218 μm, the active material thickness, the Ni structural layer

thickness, and the charge rate. The total height is fixed in this optimization study to reflect the fabrication constraint due to maximum height that can be achieved by the photoresist mold experimentally, which is approximately 300 μm. Values higher than 218 μm are not used due to significant computational loads. Also note since we mainly focus on cathode optimization in the current study and the anode is assumed to be in great excess, the energy and power densities are calculated based only on the cathode structure (including the mass and the volume of the Ni current collector, the active material, and the electrolyte within the cathode structure). It can be seen from Figure 5.7 (a) and (b) that when interlayer spacing is greater than 0.2 μm, both the energy and power densities decrease as interlayer spacing increases, as a result of decreased number of layers. However, when the interlayer spacing decreases below 0.2 μm, as can be seen in Figure 5.7 (c), the capacity retention decreases dramatically below 95%, which is likely due to the amount of electrolyte (i.e., KOH) in between two active material layers, especially for the layers in the middle of the structure, being insufficient to support the electrochemical reaction as the interlayer spacing narrows. This causes a decrease in the active material utilization and thus energy density [18]. In addition, through extrapolation, the gravimetric power density improves marginally below 0.2 μm for all active material thicknesses shown. Hence, an interlayer spacing of 0.2 μm is set to be the optimal value.

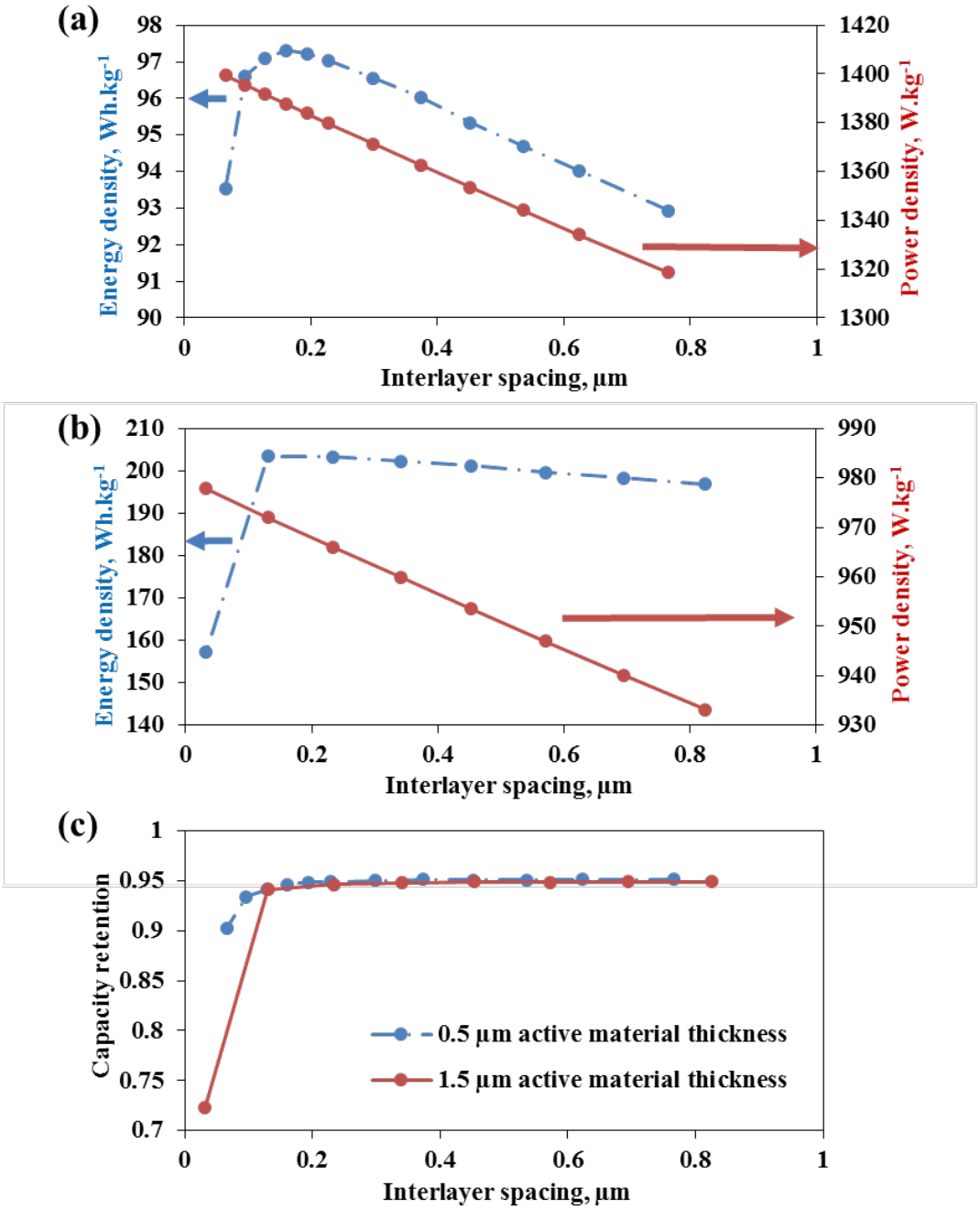

Figure 5. 7**:** Gravimetric energy and power densities as a function of interlayer spacing for an electrode with 218 µm total height and 1.5 um Ni thickness: **(a)** 0.5-µm-thick active material at 13.5C, **(b)** 1.5-µm-thick active material at 4.5C. **(c)** capacity retention as a function of interlayer spacing for electrodes with 0.5 µm and 1.5 µm thick active material, 13.5 C and 4.5 C charge rates respectively, 218 µm total height, and 1.5 µm Ni thickness.

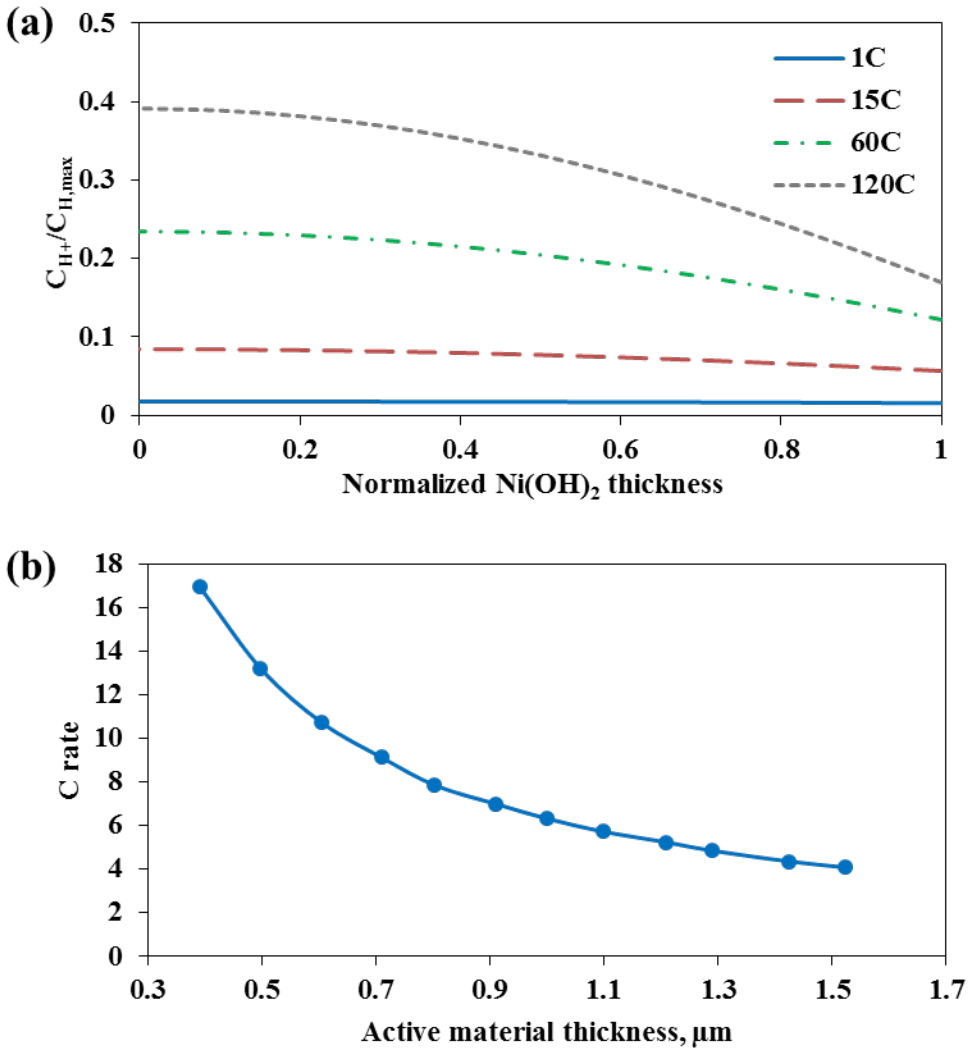

Figure 5. 8: **(a)** Concentration profiles of H^+ across the active material thickness at the end of the charging process at different C rates, at the middle layer of a 10-layer structure. Normalized thickness values of 0 and 1 refer to Ni current collector/$Ni(OH)_2$ and $Ni(OH)_2$/KOH electrolyte interfaces, respectively, and **(b)** Maximum charge rate that allows 95% capacity retention of different active material thickness. Structure dimensions: 1.5 µm Ni thickness, 0.2 µm interlayer spacing, 218 µm total height.

During charging of the electrode, protons diffuse from the bulk of the active material (i.e., $Ni(OH)_2$) to the electrode/electrolyte interface, resulting in a concentration gradient that forms within the active material film. As the charge rate increases, the concentration

gradient for the protons increases. At sufficiently high charge rates, it may not be possible for the protons to diffuse away from the active material in a desired duration of time due to limited proton diffusion rates and earlier onset of the oxygen evolution reaction. Figure 5.8 (a) shows the concentration profile of protons across the active material film at the end of the charging process. It can be clearly seen from Figure 5.8 (a) that for a $Ni(OH)_2$ film thickness of 1 μm, a negligible concentration profile forms across the active material at 1C, indicating that it is possible to almost fully charge the electrode at this rate. As the charge rate increases, there is a gradual increase in the amount of protons at the current collector/$Ni(OH)_2$ interface, which are not able to be delivered to the electrolyte. With a charge rate of 120C, about 30% of the protons cannot be transported to the electrolyte in 30 seconds.

Thus, we can conclude that for each active material thickness, there is a maximum C rate, say x C, for the active material to be fully (or almost fully, i.e., 95%) charged within x^{-1} hours. Figure 5.8 (b) shows the relationship between this maximum charge rate and the active material thickness. As expected, the maximum charge rate that allows at least 95% capacity retention decreases with the active material thickness due to increased diffusion lengths. Hence, we can clearly observe the tradeoff between energy density and power density for the $Ni(OH)_2$ electrode, and in fabrication we can choose the active material thickness depending on whether energy density or power density is deemed more important in the actual application scenario. The gravimetric density is more important for macroscale applications where the mass of the power source is usually the limiting factor (e.g., cell

phones), whereas the volumetric density is generally the main concern for applications with limited space (e.g., microsensors and microactuators).

In Figure 5.9, we construct Ragone plots of the micro-fabricated multilayer electrode by plotting the projected power density on the y-axis and the projected energy density on the x-axis, parametrized by the Ni structural thickness. For each Ni current collector thickness, energy densities for active material thickness ranging from 0.4 μm to 1.5 μm at an interval of 0.1 μm are calculated. All data points are generated using an optimal interlayer spacing of 0.2 μm and the corresponding power density on the y-axis represents the maximum power that could be obtained with 95% capacity retention. We also incorporate the performance of the experimentally fabricated structure on the plot. Based on the projections, it can be seen that for both gravimetric and volumetric basis, by reducing the interlayer spacing from 2 μm to 0.2 μm and Ni structural layer thickness from 1.5 μm to 0.5 μm, we can double the energy density and increase the power density by almost one order of magnitude, in comparison with experimental performance.

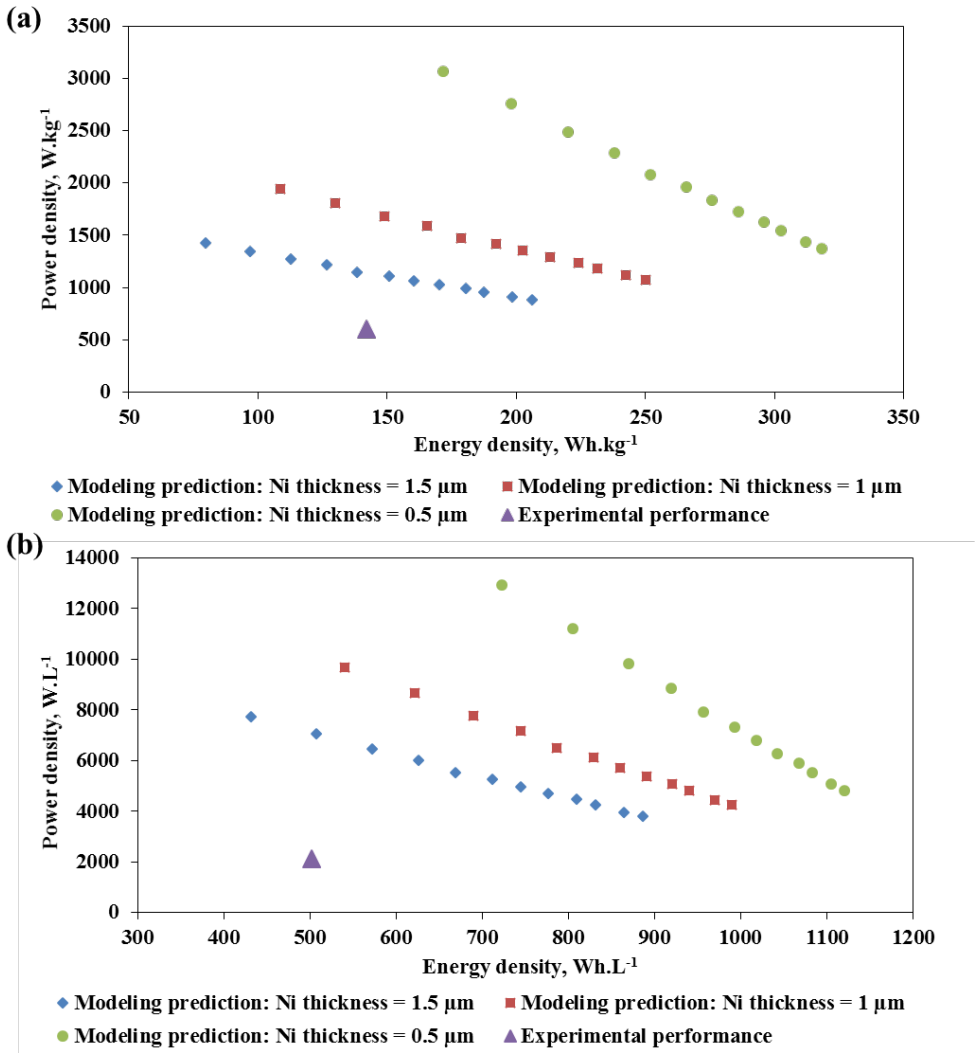

Figure 5. 9**:** For a 218 µm tall structure with 0.2 µm interlayer spacing, theoretical power density of the electrodes is plotted as a function of theoretical energy density, parametrized by the Ni current collector layer thickness; comparison is made with experimental performance on: **(a)** gravimetric basis, **(b)** volumetric basis. For each Ni current collector thickness, the individual data points represent active material thicknesses ranging from 0.4 µm to 1.5 µm, with an interval of 0.1 µm.

5.3. Physical parameter measurement

In order to obtain accurate prediction through electrochemical modeling, key physical parameters such as diffusion coefficient and exchange current density of the active material need to be measured. As shown in Figure 5.10 below, inaccuracies associated with the measurement of the diffusion coefficient would significantly impact prediction accuracy. The values of these parameters are not reported in a consistent way in literature. For example, depending on the synthesis methods and measurement techniques, the diffusion coefficient of $Ni(OH)_2$ could vary by 5 orders of magnitude in addition to changes in state of charge (SOC), as seen in Figure 5.11. In this study, we measured the diffusion coefficient of our electrodeposited $Ni(OH)_2$ using cyclic voltammetry (CV) to ensure an accurate value is used in the model and validate it against the best-fit diffusion coefficient. In addition, we utilized two other commonly used techniques, namely galvanostatic intermittent titration technique (GITT) and electrochemical impedance spectroscopy (EIS) to measure the Li diffusion coefficient in NiSn anode for Li-ion battery, as well as cyclic voltammetry (CV). GITT and EIS can measure diffusion coefficients as a function of Li intercalation level, or state of charge (SOC), whereas only the average diffusion coefficient can be measured for CV. The working principles of these three methods and measurement results will be detailed in this section.

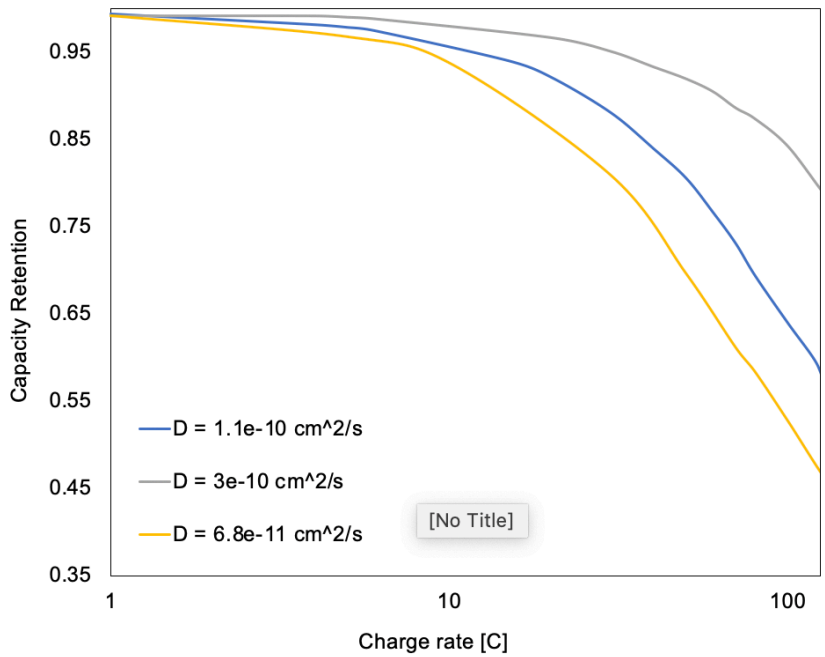

Figure 5. 10: Sensitivity analysis for the effect of proton diffusion coefficient on capacity retention

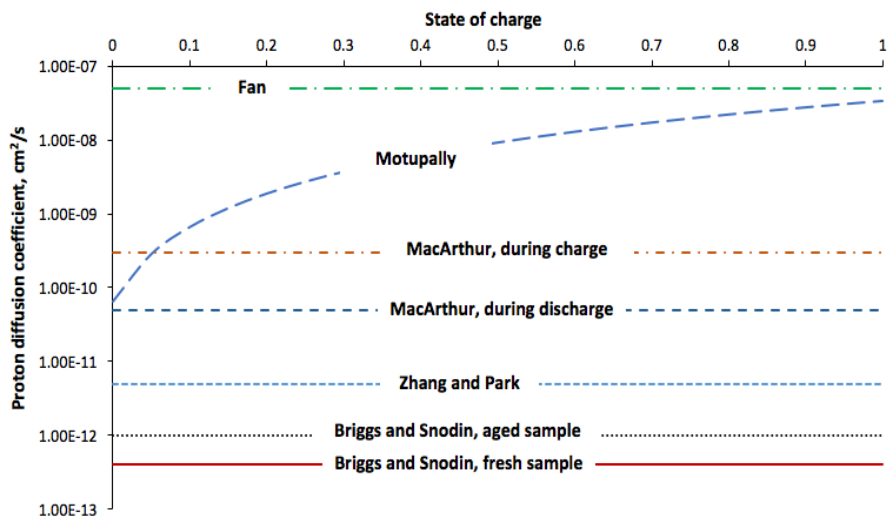

Figure 5. 11: Variation of proton diffusion coefficient in $Ni(OH)_2$ cathode in literature [19-22]

Note that for the diffusion coefficient to have an unambiguous physical meaning, the concentration of the intercalants must change monotonically as intercalation proceeds [23],

which is only valid for topotactic solid-state reactions. When the intercalation of ions is accompanied by strong electron–ion interactions, the intercalation proceeds following one or several reaction fronts and leads to the coexistence of two phases [24]. The coexistence of two phases makes the meaning of the chemical diffusion coefficient as a function of the composition ambiguous [25]. However, the measured diffusion coefficient may still be taken as an effective measurement, mainly reflecting attractive interactions between the intercalation species in the narrow layer in which the boundary between the co-existing phases moves as a result of the applied potential that drives the insertion-deinsertion process [23].

5.3.1. Cyclic voltammetry

Cyclic voltammetry is widely used to study the oxidation/reduction characteristics in electrochemical reactions and to obtain the diffusion coefficient of intercalant ions. During a typical cyclic voltammetry experiment, the potential is varied linearly as a function of time with sweep rate v in both anodic and cathodic directions, over a range that covers all relevant electrochemical reactions of interest. Specifically, if the scan is initiated at the cathodic side of E_{eq}, the equilibrium potential of the electrochemical reaction, only non-faradaic currents flow initially. When the electrode potential reaches the vicinity of E_{eq}, the reduction begins and current starts to flow. As the potential continues to grow more positive (anodic), the surface concentration of reductant must drop; hence, the flux to the surface increases. If the electrochemical reaction is assumed to be diffusion-limited, as is the case for most processes, the current would be proportional to the flux of ions and increase correspondingly. As the potential moves past E_{eq}, the surface concentration of the

reductant drops nearly to zero, the mass transfer of reductant to the surface reaches a maximum rate and then declines as the depletion effect is initiated [26]. The observation is therefore a peaked current-potential curve as depicted in Figure 5.12 below. The reverse procedure occurs when the potential is scanned in the opposite direction.

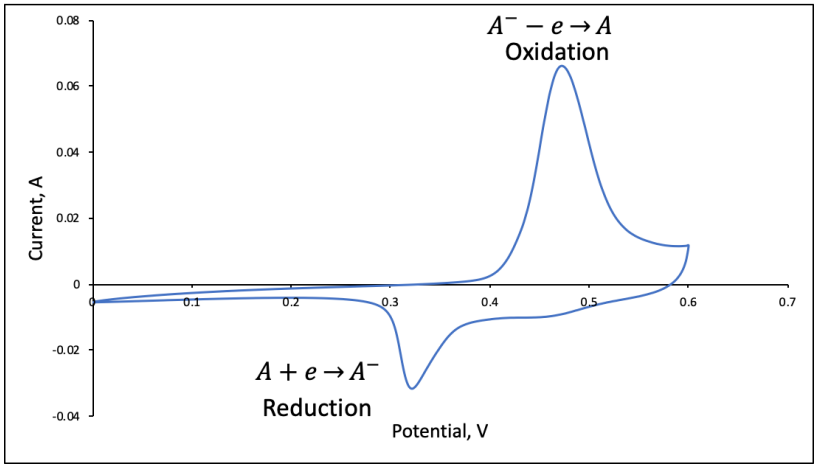

Figure 5. 12**:** A sample voltammogram

Extraction of the diffusion coefficient of the intercalant species requires the use of Fick's first law and the conservation of mass:

$$\frac{\partial C_o(x,t)}{\partial t} = D_o \frac{\partial^2 C_o(x,t)}{\partial x^2} \qquad \frac{\partial C_R(x,t)}{\partial t} = D_R \frac{\partial^2 C_R(x,t)}{\partial x^2} \tag{21}$$

with the initial conditions:

$$C_o(x,0) = 0 \qquad C_R(x,0) = C_{R,0} \tag{22}$$

where C_o is the concentration of the oxidant, C_R is the concentration of the reductant. Assuming the semi-infinite diffusion condition holds for the time scale of the experiment (i.e. the active material has sufficient thickness):

$$\lim_{x\to\infty} C_o(x,t) = 0 \qquad \lim_{x\to\infty} C_R(x,t) = C_{R,0} \tag{23}$$

where the infinite distance is set at the active material/current collector interface. A flux balance at active material surface (x= 0) gives:

$$D_o\left(\frac{\partial C_o(x,t)}{\partial x}\right)_{x=0} + D_R\left(\frac{\partial C_R(x,t)}{\partial x}\right)_{x=0} = 0 \tag{24}$$

Assuming an irreversible reaction $Oxidant + e^- \xrightarrow{k_f} Reductant$, the final boundary condition is:

$$\frac{i}{FA} = D_o\left(\frac{\partial C_o(x,t)}{\partial x}\right)_{x=0} = k_f(t)C_o(0,t) = k^0 \exp\{-\alpha f\left(E(t) - E_{eq}\right)\} C_o(0,t) \tag{25}$$

The solution of the diffusion equations yields the following expression for the peak current (check detailed solution procedure at Chapter 5 and 6 of reference [26]):

$$I_P = 2.99 \cdot 10^5 \cdot n \cdot (\alpha \cdot n_\alpha)^{0.5} \cdot A \cdot C_{R,0} \cdot v^{0.5} \cdot D_R^{0.5} \tag{26}$$

where I_p [A] is the peak current, n is the number of electrons transferred, α is the transfer coefficient with n_α being the apparent number of electrons transferred, A [cm^2] is the

surface area of the electrode (cm^2), $C_{R,0}$ [mol cm^{-3}] is the initial reductant concentration within the active material, and v [V s^{-1}] is the potential scan rate. Here, $n = 1$, and the $\alpha \cdot n_\alpha$ value of 1.5 was assumed [27]. In addition, the geometrical area of the electrode was used for A. Based on Equation (26), the slope of I_p vs. $v^{0.5}$ from cyclic voltammograms can be used to determine diffusion coefficient of the intercalant D_R.

Herein, we measured the average diffusion coefficient of our electrodeposited $Ni(OH)_2$ over all states of charge by utilizing cyclic voltammetry (CV). A three-electrode cell configuration was used for diffusion coefficient measurement. Freshly electrodeposited $Ni(OH)_2$ on a Ni foil was used as the working electrode, a large Ni sheet as the counter electrode, and a Hg/HgO electrode (6M KOH) as the reference. A 6M KOH solution was used as the electrolyte. The scan range was 0~0.6V relative to the reference electrode. Scan rates of 2 mV s^{-1}, 4 mV s^{-1}, 6 mV s^{-1}, 8 mV s^{-1}, 10 mV s^{-1}, 15 mV s^{-1}, and 20 mV s^{-1} were used.

Figure 5.13 (a) below shows a sample cyclic voltammogram for $Ni(OH)_2$ at varying scan rates. Peak currents during anodic scan are plotted versus square root of the scan rate $v^{1/2}$ to extract diffusion coefficient from slope of the curve in Figure 5.13 (b), according to equation (26).

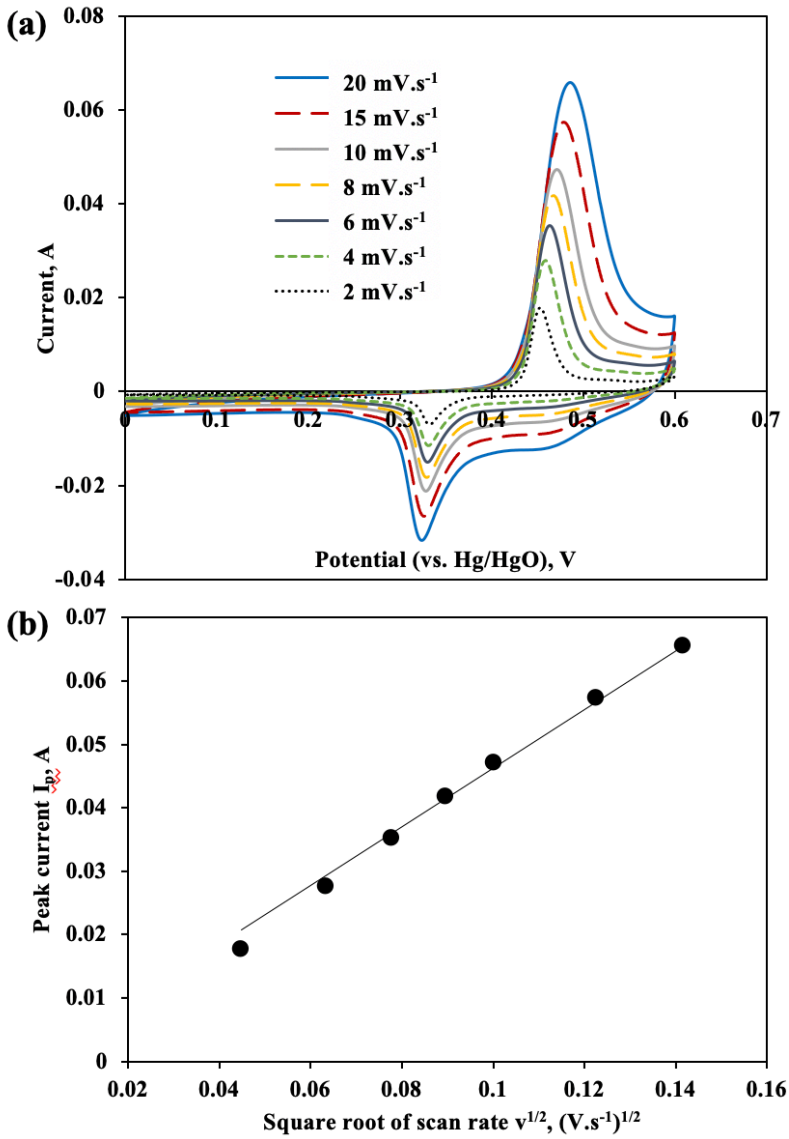

Figure 5. 13: **(a)** Sample CV of $Ni(OH)_2$ electrode at various scan rates, **(b)** anodic peak currents of the CV as a function of square root of the scan rates.

Repeated cyclic voltammetry measurements show that the experimental diffusion coefficient value ranges from 2×10^{-10} cm^2 s^{-1} to 3×10^{-10} cm^2 s^{-1}. Best-fit value from the 2D electrode model is 3.4×10^{-10} cm^2 s^{-1}, which is in reasonable agreement with the experimentally measure value.

The diffusion coefficient of Li ions in NiSn anode was also determined, using a three-electrode cell configuration. Freshly electrodeposited NiSn on a Cu foil was used as the working electrode, a Li foil as the counter electrode, and a thin Li strip as the reference. The electrolyte was 1M $LiClO_4$ in 1:1 dimethyl carbonate (DMC)/ethylene carbonate (EC) (v/v) . The scan range was 0.01V ~ 1.5V relative to the reference electrode. Scan rates of 0.05 mV s^{-1}, 0.1 mV s^{-1}, and 0.2 mV s^{-1} were used. Peak currents during anodic scan are plotted versus square root of the scan rate $v^{1/2}$ to extract Li diffusion coefficient from slope of the curve in Figure 5.14, according to equation (26). The calculated average Li diffusion coefficient over all states of charge is 3.63×10^{-13} cm^2/s. This value was compared with values measured from galvanostatic intermittent titration (GITT) and electrochemical impedance spectroscopy (EIS) to validate accuracy of the measurement, shown in section 5.3.4.

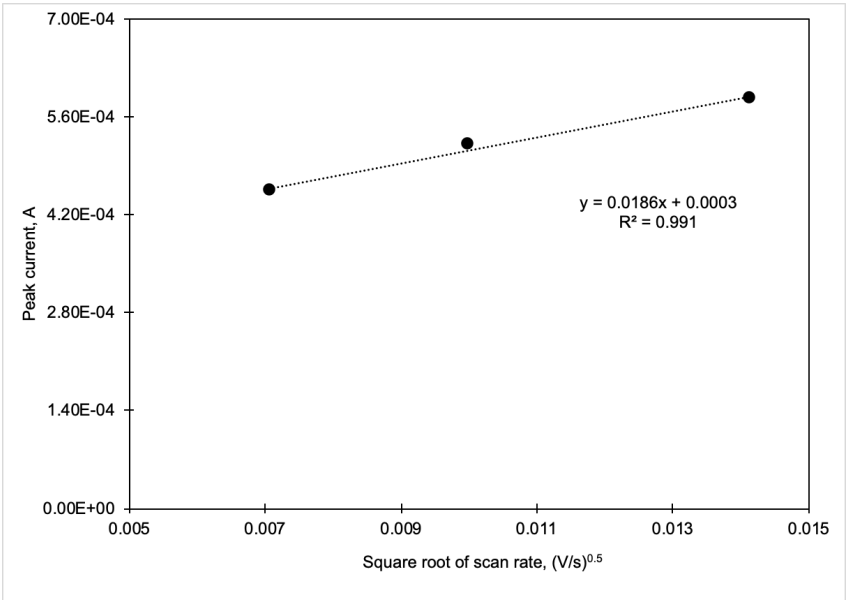

Figure 5. 14**:** Anodic peak currents of the CV as a function of square root of the scan rates.

5.3.2. Galvanostatic intermittent titration technique (GITT)

Among the current pulse methods, the galvanostatic intermittent titration technique (GITT) proposed by Weppner and Huggins [28] has been used as a standard method to obtain chemical diffusion coefficients in electrode materials. For notation purposes, we assume Li ion as the intercalant and Li-ion battery material B as the host. In a typical GITT experiment, starting with a sample of known stoichiometric composition with potential E_0 at thermodynamic equilibrium (i.e. homogenous Li concentration throughout thickness of the sample with no gradient), a small current I_0 is applied to the cell at t_0 for a time interval τ. The applied potential increases/decreases due to change of lithiation level in the electrode, and a Li concentration gradient forms throughout thickness of the electrode due to finite Li ion diffusion. A voltage drop, corresponding to the IR drop due to the current flux, is superimposed, whose magnitude depends on position of the reference electrode [28], as shown in Figure 5.15. However, this voltage drop is time-independent constant and does not alter the geometrical shape of the voltage-time curve [28]. After time period τ, the current is interrupted and consequently the IR voltage drop is removed. The Li ion concentration becomes homogeneous again by diffusion during this equilibration process, and the potential of the electrode drifts back toward a new steady state value E_1, corresponding to a new activity of Li ions in the electrode as result of change of stoichiometry [28]. This current application/interruption process is repeated until the composition interval of interest is covered.

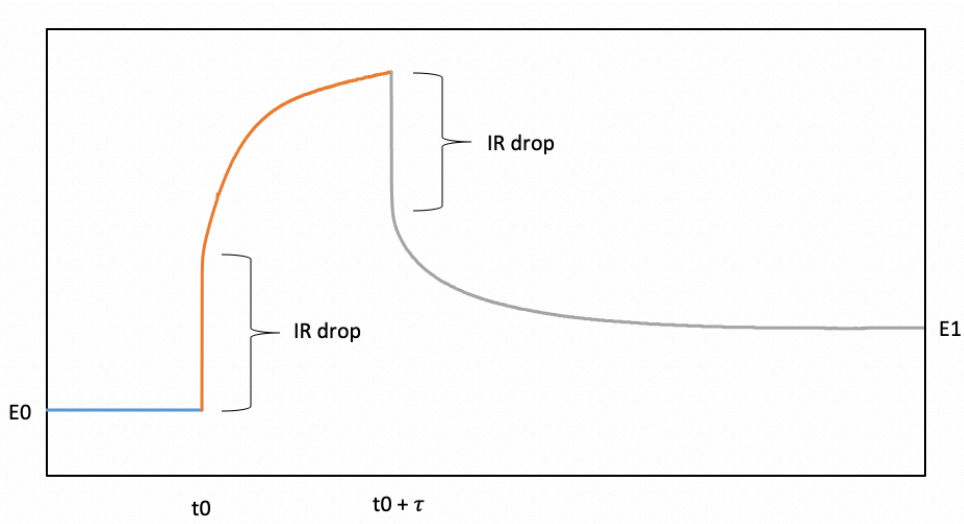

Figure 5. 15: Schematic illustration of a single step of GITT

In order to extract the diffusion coefficient of the intercalant species, we need to solve the diffusion equations with appropriate boundary reactions for electrode reactions, as we did for the CV method.

$$\frac{\partial C_{Li}(x,t)}{\partial t} = D_{Li}\frac{\partial^2 C_{Li}(x,t)}{\partial x^2} \tag{27}$$

with initial and boundary conditions

$$C_{Li}(x,0) = C_{Li,0} \tag{28}$$

$$D_{Li}\left(\frac{\partial C_{Li}(x,t)}{\partial x}\right)_{x=0} = \frac{I_0}{nFA} \tag{29}$$

$$D_{Li}(\frac{\partial C_{Li}(x,t)}{\partial x})_{x=L} = 0 \tag{30}$$

where n is the number of electrons transferred per mole of Li. Solution of the diffusion equations yields the following expression for lithium concentration at the electrode surface:

$$C_{Li}(x=0,t) = C_{Li,0} + \frac{2I_0\sqrt{t}}{nAF}\sum_{n=0}^{\infty}(ierfc\left[\frac{nL}{\sqrt{D_{Li}t}}\right] + ierfc\left[\frac{(n+1)L}{\sqrt{D_{Li}t}}\right]) \tag{31}$$

At times t << $\frac{L^2}{D}$, the infinite sum can be approximated by the first term, thus:

$$\frac{dC_{Li}(x=0,t)}{d\sqrt{t}} = \frac{2I_0}{nAF\sqrt{D_{Li}\pi}} \qquad \left(t \ll \frac{L^2}{D}\right) \tag{32}$$

If changes of the molar volume with composition may be neglected, the changes in the concentration and the stoichiometry are related through

$$dC_{Li} = \frac{1}{V_M}d\delta \qquad \text{where } \Delta\delta = \frac{I_0\tau M_B}{nm_BF} \tag{33}$$

where V_M is the molar volume of the host, M_B is the molecular weight of the most, m_B is the mass of the host, and $\Delta\delta$ is the change of stoichiometry due to coulometric titration. Inserting equation (33) into (32), expanding by dE on both sides, and rearranging the

equation gives:

$$D_{Li^+} = \frac{4}{\pi}\left(\frac{V_M}{AFn}\right)^2\left[I_0 \left(dE/d\delta\right) \Big/ \left(dE/d\sqrt{t}\right)\right]^2 \qquad \left(t \ll \frac{L^2}{D}\right) \tag{34}$$

$dE/d\delta$ is found by calculating the slope of the titration curve by plotting the equilibrium potential after each rest period versus δ. $dE/d\sqrt{t}$ is found for $t \ll \frac{L^2}{D}$ when the current is applied.

The diffusion coefficient of Li ions in our electrodeposited NiSn anode was measured by GITT as a function of Li intercalation level, or state of charge (SOC). A three-electrode cell configuration was used for diffusion coefficient measurement to avoid issues with electrode polarizations. Freshly electrodeposited NiSn on a Cu foil was used as the working electrode, a Li foil as the counter electrode, and a Li strip as the reference. A Gamry electrochemical cell [29] for Li-ion battery testing was utilized to hold the electrodes and Li strip is placed in between the NiSn working electrode and the Li foil counter electrode. 1M $LiClO_4$ in 1:1 dimethyl carbonate (DMC)/ethylene carbonate (EC) (v/v) was used as the electrolyte. Here we only measured the diffusion coefficient during delithiation, since the side reactions occur during the NiSn anode lithiation making it difficult to accurately determine Li intercalation levels [30]. Thus, a current rate of C/6 was first used to fully lithiate the NiSn electrode until a cutoff potential of 0.01V, followed by 3 hours of OCV. Within each cycle, a C/12 rate was applied for 10 min, followed by an OCV period of 60

minutes so that the electrode reached a new equilibrium state. When the current was applied, the potential increases with time (Figure 5.16 (a)). The initial 100s was used to generate the E vs. $\sqrt{t}$ curve to find the $dE/_{d\sqrt{t}}$ term in equation (34). As we can see from Figure 5.16 (b), a linear relationship is satisfied, suggesting validity of $t \ll \frac{L^2}{D}$ assumption for the first 100s.

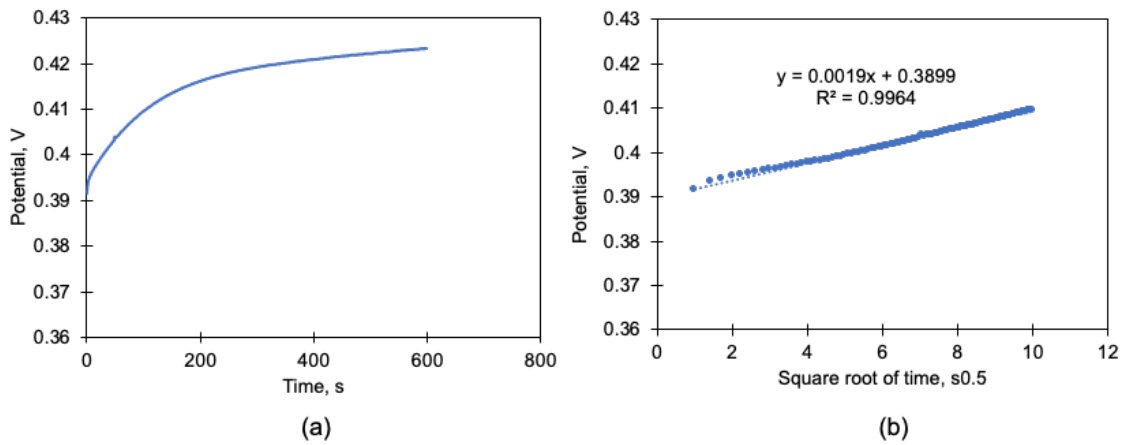

Figure 5. 16: (a) Potential vs. time when current is applied (b) Initial 100s of potential vs. square root of time when current is applied

A total of 72 cycles were performed, and the voltage at the end of each equilibration period was plotted as a function of lithium intercalation as shown in Figure 5.17 below. Equilibrium curve was divided into sections and each section was fitted with polynomial functions to calculate $dE/_{d\delta}$ at each δ.

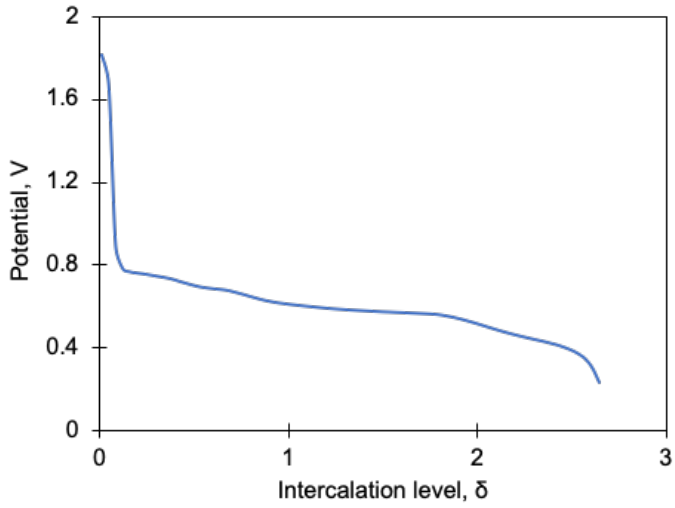

Figure 5. 17**:** Equilibrium potential vs. lithium intercalation level in NiSn anode

With $dE/_{d\sqrt{t}}$ and $dE/_{d\delta}$ information, the Li diffusion coefficient was calculated according to equation (34) as shown in Figure 5.18 below. Note a molar volume V_M = 16 cm^3/mol was used.

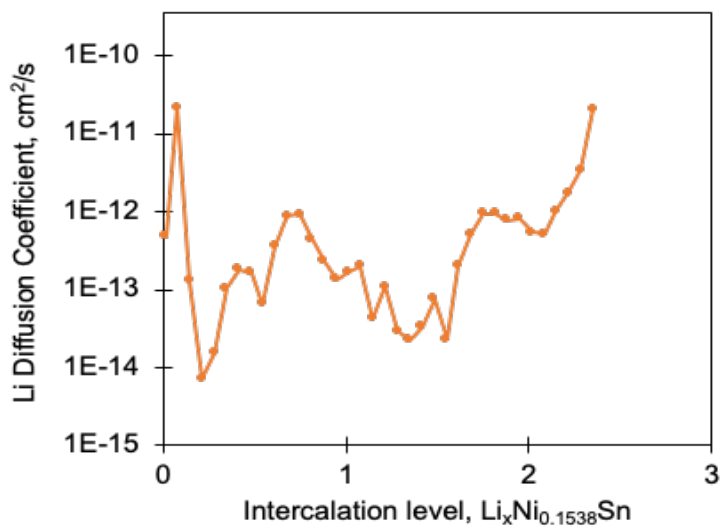

Figure 5. 18**:** Li diffusion coefficient in NiSn anode as a function of intercalation level, measured by GITT

Note that there are two minimums at $\delta = 0.2$ and $\delta = 1.5$, which correspond to two-phase regions of LiNiSn alloys. As described previously, although the interpretation of the diffusion coefficient becomes unclear in these regions, the measured diffusion coefficient may still be taken as an effective measurement as D_{app}.

5.3.3 Electrochemical impedance spectroscopy (EIS)

Electrochemical impedance spectroscopy is a powerful tool to identify the kinetics of lithium-ion intercalation/deintercalation into the electrodes [31]. In a typical EIS experiment, the cell is perturbed with an alternating voltage of small amplitude around the equilibrium potential to observe the way in which the system follows the perturbation at steady state [26]. For data interpretation and analysis, an electrochemical cell can be considered simply an impedance to a small sinusoidal excitation; hence, its performance can be represented by an equivalent circuit of resistors and capacitors that pass current with the same amplitude and phase angle [26]. If measurements are made over a wide-enough frequency range, then the different physical processes may be separated by their time constants in the complex plane [31], where the x-axis is the real part of the impedance and the y-axis is the imaginary part of the impedance (i.e. a Nyquist plot).

For example, one of the most common equivalent circuit is the Randles circuit as shown below in Figure 5.19:

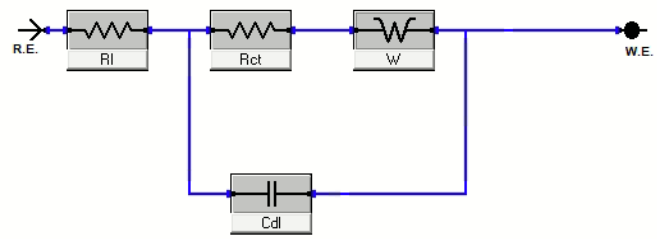

Figure 5. 19**:** The Randles equivalent circuit

In this circuit, R_I is the ohmic resistance of the electrolyte and the electrode, including any contact resistance; C_{dl} is the double layer capacitance of the electrode – electrolyte interface; R_{ct} is the charge transfer resistance at the electrode/electrolyte interface, and can be related to the exchange current density i_0 through linearization of Butler-Volmer equation for small overpotential, which is satisfied during EIS:

$$R_{ct} = \frac{\partial E}{i} = \frac{RT}{nFi_0}, \quad \partial E \ll \frac{RT}{F} \tag{35}$$

W is a complex impedance arising from the diffusion of the intercalant species. For the case of semi-infinite diffusion:

$$W = B\omega^{-\frac{1}{2}} - jB\omega^{-\frac{1}{2}} \tag{36}$$

where ω is the radial frequency, j = $\sqrt{-1}$, and B is a constant which contains a concentration independent diffusion coefficient.

Since W is a function of frequency and R_{ct} is independent of frequency, then an electrode reaction may be controlled by diffusion at low frequencies and by charge transfer at high frequencies [31]. A sample Nyquist plot is shown below.

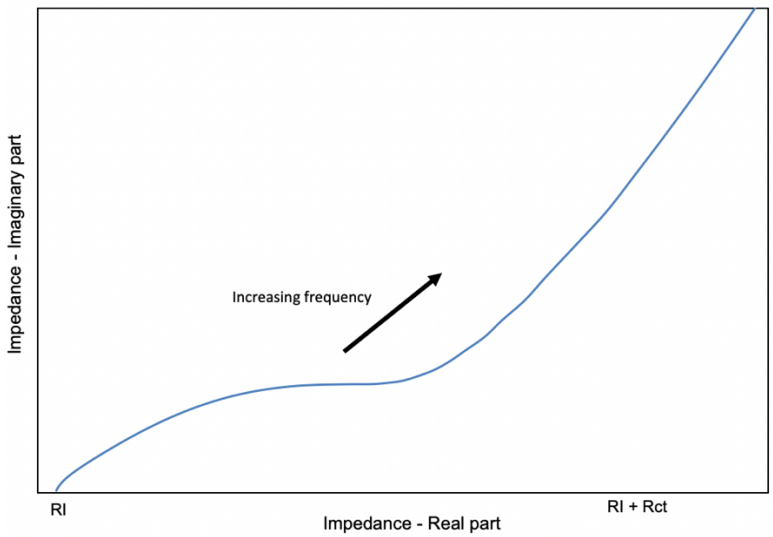

Figure 5. 20**:** Sample Nyquist plot

In order to find diffusion coefficient from EIS, Fick's law equation with suitable initial and boundary conditions need to be solved, analogous to the determination of D from GITT. The governing equation (equation 37), boundary conditions (equations 38 and 39), and initial conditions (equation 40) are shown below. Detailed solution procedures can be found in reference [31]:

$$\frac{\partial[\Delta C_{Li}(x,t)]}{\partial t} = D_{Li}\frac{\partial^2[\Delta C_{Li}(x,t)]}{\partial x^2} \tag{37}$$

$$\Delta C_{Li}(0,t) = \frac{v_0 \sin(\omega t)}{V_M}\left({}^{dE}/_{d\delta}\right)^{-1} \tag{38}$$

$$D_{Li}\left(\frac{\partial[\Delta C_{Li}(x,t)]}{\partial x}\right)_{x=L} = 0 \tag{39}$$

$$\Delta C_{Li}(x,0) = 0 \tag{40}$$

where $v_0 \sin(\omega t)$ is the sinusoidal voltage excitation, V_M is the molar volume of the host, $dE/d\delta$ is found by plotting the equilibrium potential after each rest period versus δ and calculating the titration curve slope. Solution of the equations 37 - 40 yields the expression for B in equation (36):

$$B = \left|\frac{V_M\left(dE/d\delta\right)}{\sqrt{2}FD_{Li}A}\right| \tag{41}$$

A value for B can be obtained by fitting the response of the electrode, namely Nyquist plot, with an appropriate equivalent circuit that has the semi-infinite Warburg element. Thus D_{Li} at state of charge δ can be calculated accordingly as:

$$D_{Li} = \left|\frac{V_M\left(dE/d\delta\right)}{\sqrt{2}FAB}\right| \tag{42}$$

Note that EIS is must be performed during equilibrium. However, GITT and EIS tests can be combined. Using the same three-electrode set-up as GITT, for each current application/interruption interval, EIS can be performed at the end of each GITT

interruption period, assuming the interruption period is long enough and equilibrium has been reached. For each EIS measurement, a voltage excitation amplitude of 10 mV was used and frequencies spanned from 100 kHz to 10 mHz.

The Nyquist plot data requires an appropriate equivalent circuit model. In the case of lithium-ion battery anode including Sn, several processes have been reported in the literature, including ion conduction in solution, migration of Li-ions through the surface film, charge transfer at electrode/electrolyte interface in parallel with double layer capacitive behavior, solid state diffusion, and finally, accumulation (sorption) in the bulk sample [32-34]. Thus, the following circuit containing two RC circuits in series was proposed [33-35]:

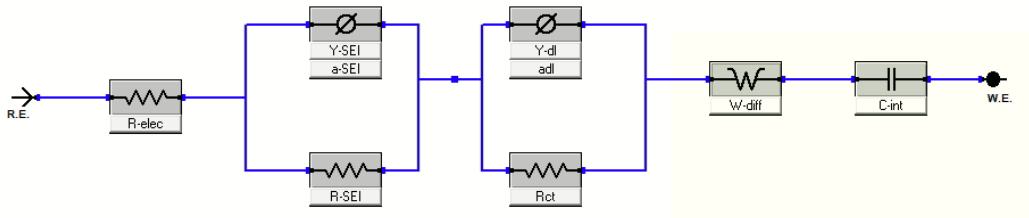

Figure 5. 21: Equivalent circuit of NiSn anode behavior in 1M $LiClO_4$ in 1:1 EC/DMC electrolyte

In this circuit, R_{elec} is the ohmic resistance of the electrolyte and the electrode, including any contact resistance. Y_{SEI} is the double layer capacitance of the surface layer resulting reduction of electrolyte species on the electrode surface. Here a constant phase element is used to account for any deviations from pure capacitive behavior. R_{SEI} represents the resistance associated with Li-ion migration through the surface film. Y_{dl} is the double layer capacitance at the electrode surface and R_{ct} is the charge transfer resistance. The use of an

infinite Warburg W_{diff} is justified to account for diffusion of Li ions since the time constant for Li diffusion calculated using L^2/D is on the order of 10^4 seconds and is much larger than the time scale of the experiment even at the lowest frequency (10 mHz). C_{int} represents accumulation of Li-ions in the bulk sample [33-34].

The data was fitted using Gamry Echem Analyst software. The model fit the data well, with a goodness of fit on the order of 10^{-6}. Figure 5.22 below shows (a) the measured exchange current density and (b) diffusion coefficient as a function of lithium intercalation level.

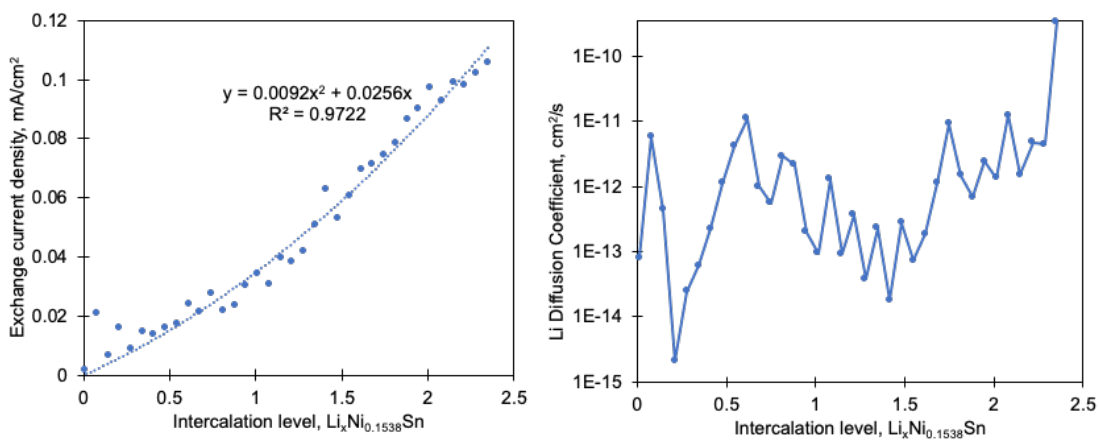

Figure 5. 22**: (a)** Exchange current density **(b)** Li ion diffusion coefficient in NiSn anode as a function of Li intercalation level, measured by EIS

Note that in Figure 5.22 (a) the exchange current density almost increases monotonically with Li intercalation level, and the shape can be captured by a parabolic equation. This trend was also observed in similar alloy-based anode material such as Si [36].

5.3.4 Comparison of results from three techniques

The Li diffusion coefficient was measured by three separate techniques, namely CV, GITT, and EIS. The values obtained can be compared for cross-validation purposes. Figure 5.23 compares the diffusion coefficient measured by these three methods in a single plot:

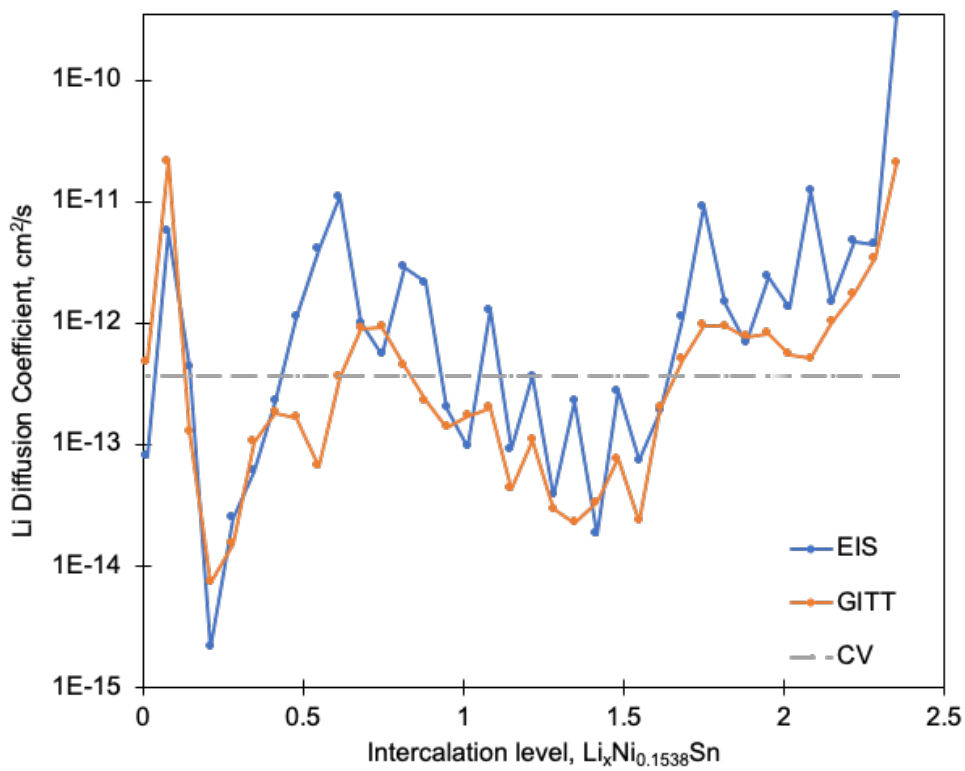

Figure 5. 23**:** Comparison of diffusion coefficient measured by EIS, GITT, and CV

As we can see, despite small variations within the same order of magnitude, Li diffusion coefficient D_{Li} measured by EIS and GITT follow very similar trends. In addition, D_{Li} measured by CV is close to the average value of those determined by GITT and EIS. This result suggests good agreement between different measurement types, and the measured diffusion coefficient is validated to be utilized for physical modeling purposes.

5.4. Conclusions

In this chapter, a mathematical model was developed based on a highly scalable and well-ordered microfabricated 3D $Ni(OH)_2$ electrodes to demonstrate its application to designing electrode architecture to optimize energy density and power density.

The model was validated against experimental data and some insights were obtained: (1) with a decrease in interlayer spacing, the energy density first increases as more layers can be included for a fixed total height, and then decreases since the amount of electrolyte becomes insufficient to support the electrochemical reaction as the interlayer spacing narrows, which demonstrates the importance of sufficient porosity in a tall 3D electrode. (2) the maximum charge rate that allows at least 95% capacity retention decreases with the active material thickness due to increased ion diffusion lengths. Hence there is a clear tradeoff between energy density and power density for the micro-battery electrode, and in fabrication we may choose the active material thickness depending on whether energy density or power density is deemed more important in the actual application scenario.

We can then use the model to optimize the design of the 3D electrodes and guide the fabrication processes. Based on model projections, by reducing the interlayer spacing from 2 μm to 0.2 μm and Ni structural layer thickness from 1.5 μm to 0.5 μm, the energy density can be doubled and the power density can be increased by almost one order of magnitude. Thus, we can see that these models open up the possibility for the realization of deterministically engineered electrodes for both micro- and macro-scale application.

Well-defined geometries of 3D $Ni(OH)_2$ electrodes provides insights on how geometric parameters could affect electrode performance. In future studies, these models may be extended to the more complex porous electrodes that we developed in Chapter 2 – 5, by applying similar mass/charge transport and reaction kinetics principles. The modeling would assist in optimizing the design of the porous electrodes by adjusting parameters such as active material thickness, porosity, tortuosity, and overall electrode thickness.

In order to obtain accurate prediction through electrochemical modeling, key physical parameters such as diffusion coefficient and exchange current density of the active material need to be measured reliably. In this study, the diffusion coefficient of $Ni(OH)_2$ and NiSn for Li-ion battery was measured using three different electrochemical methods: cyclic voltammetry (CV), galvanostatic intermittent titration technique (GITT), and electrochemical impedance spectroscopy (EIS). For $Ni(OH)_2$, the measured diffusion coefficient by CV is very close to the best-fit value from the 2D electrode model. For NiSn, there is good agreement of measured Li-ion diffusion coefficient among three techniques. The exchange current density of NiSn is also measured by EIS.

5.5. Reference

1. Reddy, T. B. (2010). *Linden's Handbook of Batteries: Set 2*. New York: McGraw-Hill Professional.
2. Armutlulu, A., Allen, S. B., & Allen, M. G. (2013). Microfabricated nickel-based electrodes for high-power battery applications. *Journal of Micromechanics and Microengineering*, *23*(11), 114008.
3. Zhang, H., Yu, X., & Braun, P. V. (2011). Three-dimensional bicontinuous ultrafast-charge and-discharge bulk battery electrodes. *Nature nanotechnology*, *6*(5), 277-281.
4. Wu, M. S., Huang, C. Y., & Lin, K. H. (2009). Electrophoretic deposition of nickel oxide electrode for high-rate electrochemical capacitors. *Journal of Power Sources*, *186*(2), 557-564.
5. Ayeb, A., & Notten, P. H. L. (2008). The oxygen evolution kinetics in sealed rechargeable NiMH batteries. *Electrochimica acta*, *53*(19), 5836-5847.
6. Ta, K. P., & Newman, J. (1999). Proton intercalation hysteresis in charging and discharging nickel hydroxide electrodes. *Journal of the Electrochemical Society*, *146*(8), 2769-2779.
7. De Vidts, P., & White, R. E. (1995). Mathematical Modeling of a Nickel-Cadmium Cell: Proton Diffusion in the Nickel Electrode. *Journal of the Electrochemical Society*, *142*(5), 1509-1519.
8. Gu, W. B., Wang, C. Y., Li, S. M., Geng, M. M., & Liaw, B. Y. (1999). Modeling discharge and charge characteristics of nickel–metal hydride batteries. *Electrochimica Acta*, *44*(25), 4525-4541.
9. Isaacson, M. J., McLarnon, F. R., & Cairns, E. J. (1990). Current Density and ZnO Precipitation-Dissolution Distributions in Zn-ZnO Porous Electrodes and Their Effect on Material Redistribution: A Two-Dimensional Mathematical Model. *Journal of the Electrochemical Society*, *137*(7), 2014-2021.
10. Paxton, B., & Newman, J. (1997). Modeling of nickel/metal hydride batteries. *Journal of the Electrochemical Society*, *144*(11), 3818-3831.

11. Motupally, S., Streinz, C. C., & Weidner, J. W. (1995). Proton diffusion in nickel hydroxide films: measurement of the diffusion coefficient as a function of state of charge. *Journal of the Electrochemical Society*, *142*(5), 1401-1408.
12. Srinivasan, V., Weidner, J. W., & White, R. E. (2000). Mathematical models of the nickel hydroxide active material. *Journal of Solid State Electrochemistry*, *4*(7), 367-382.
13. Gomadam, P. M., Weidner, J. W., Dougal, R. A., & White, R. E. (2002). Mathematical modeling of lithium-ion and nickel battery systems. *Journal of power sources*, *110*(2), 267-284.
14. MacArthur, D. M. (1970). The hydrated nickel hydroxide electrode potential sweep experiments. *Journal of The Electrochemical Society*, *117*(4), 422-426.
15. Zhang, C., & Park, S. M. (1987). The anodic oxidation of nickel in alkaline media studied by spectroelectrochemical techniques. *Journal of the Electrochemical Society*, *134*(12), 2966-2970.
16. Bing, L., Huatang, Y., Yunshi, Z., Zuoxiang, Z., & Deying, S. (1999). Cyclic voltammetric studies of stabilized α-nickel hydroxide electrode. *Journal of power sources*, *79*(2), 277-280.
17. Wang, X. Y., Yan, J., Zhang, Y. S., Yuan, H. T., & Song, D. Y. (1998). Cyclic voltammetric studies of pasted nickel hydroxide electrode microencapsulated by cobalt. *Journal of applied electrochemistry*, *28*(12), 1377-1382.
18. Huang, C., Armutlulu, A., Allen, M. G., & Allen, S. A. B. (2017). Model-assisted development of microfabricated 3D Ni (OH) 2 electrodes with rapid charging capabilities. *Journal of Power Sources*, *358*, 101-111.
19. Zhang, C., & Park, S. M. (1987). The anodic oxidation of nickel in alkaline media studied by spectroelectrochemical techniques. *Journal of the Electrochemical Society*, *134*(12), 2966.
20. MacArthur, D. M. (1970). The hydrated nickel hydroxide electrode potential sweep experiments. *Journal of The Electrochemical Society*, *117*(4), 422-429.

21. Motupally, S., Streinz, C. C., & Weidner, J. W. (1995). Proton diffusion in nickel hydroxide films: measurement of the diffusion coefficient as a function of state of charge. *Journal of the Electrochemical Society*, *142*(5), 1401-1413.
22. Fan, D., & White, R. E. (1991). A Mathematical Model of a Sealed Nickel-Cadmium Battery. *Journal of the Electrochemical Society*, *138*(1), 17-25.
23. Levi, M. D., Gamolsky, K., Aurbach, D., Heider, U., & Oesten, R. (1999). Determination of the Li ion chemical diffusion coefficient for the topotactic solid-state reactions occurring via a two-phase or single-phase solid solution pathway. *Journal of Electroanalytical Chemistry*, *477*(1), 32-40.
24. Murphy, D. (Ed.). (2013). *Materials for advanced batteries* (Vol. 2). New York: Springer Science & Business Media.
25. Prosini, P. P., Lisi, M., Zane, D., & Pasquali, M. (2002). Determination of the chemical diffusion coefficient of lithium in LiFePO4. *Solid State Ionics*, *148*(1-2), 45-51.
26. Allen, J. B., & Larry, R. F. (2001). *Electrochemical methods fundamentals and applications*. Hoboken: John Wiley & Sons.
27. Zhang, C., & Park, S. M. (1987). The anodic oxidation of nickel in alkaline media studied by spectroelectrochemical techniques. *Journal of the Electrochemical Society*, *134*(12), 2966.
28. Weppner, W., & Huggins, R. A. (1977). Determination of the kinetic parameters of mixed-conducting electrodes and application to the system Li3Sb. *Journal of The Electrochemical Society*, *124*(10), 1569-1576.
29. GamryInstruments. (2020). *Lithium Battery Cell*. Retrieved from https://www.gamry.com/cells-and-accessories/electrochemical-cells/lithium-battery-cell/
30. Swamy, T., & Chiang, Y. M. (2015). Electrochemical charge transfer reaction kinetics at the silicon-liquid electrolyte interface. *Journal of The Electrochemical Society*, *162*(13), A7129-7134.
31. Ho, C., Raistrick, I. D., & Huggins, R. A. (1980). Application of A-C techniques to the study of lithium diffusion in tungsten trioxide thin films. *Journal of the Electrochemical Society*, *127*(2), 343-358.

32. Xu, H., Li, S., Zhang, C., Chen, X., Liu, W., Zheng, Y., ... & Li, J. (2019). Roll-to-roll prelithiation of Sn foil anode suppresses gassing and enables stable full-cell cycling of lithium ion batteries. *Energy & Environmental Science*, *12*(10), 2991-3000.
33. Levi, M. D., & Aurbach, D. (1997). Simultaneous measurements and modeling of the electrochemical impedance and the cyclic voltammetric characteristics of graphite electrodes doped with lithium. *The Journal of Physical Chemistry B*, *101*(23), 4630-4640.
34. Levi, M. D., Salitra, G., Markovsky, B., Teller, H., Aurbach, D., Heider, U., & Heider, L. (1999). Solid-state electrochemical kinetics of Li-Ion intercalation into Li1− x CoO2: simultaneous application of electroanalytical techniques SSCV, PITT, and EIS. *Journal of the Electrochemical Society*, *146*(4), 1279-1288.
35. Swamy, T., & Chiang, Y. M. (2015). Electrochemical charge transfer reaction kinetics at the silicon-liquid electrolyte interface. *Journal of The Electrochemical Society*, *162*(13), A7129-7136.
36. Baggetto, L., Oudenhoven, J. F. M., Van Dongen, T., Klootwijk, J. H., Mulder, M., Niessen, R. A. H., ... & Notten, P. H. L. (2009). On the electrochemistry of an anode stack for all-solid-state 3D-integrated batteries. *Journal of Power Sources*, *189*(1), 402-410.

Chapter 6: Conclusions and future work

6.1. Summary and Conclusions

The work reported herein focuses on the design, fabrication, and characterization of 3D porous structures for use as high-performance power source for micro-electronics devices. These electrodes possess high areal capacity suited for the target applications and are realized by electrochemical techniques. Areal capacity as high as 40 mAh/cm^2 has been demonstrated on the half-cell level for Si-based composite anodes. On the full cell level, areal capacity of 3 mAh/cm^2 has been attained with 2.3 mWh/cm^2 areal power density for NiSn/S electrodes, which is within the upper range of the micro-batteries developed so far [1-9].

The superior performance of the electrodes is mainly attributed to their high porosity. First, the high surface area increases the effective contact area between electrode and electrolyte, which decreases the overall charge transfer resistance and improves the electrochemical reaction kinetics. In addition, the porous structures significantly facilitate mass transport across the thickness of the structure by increasing the effective ion diffusion coefficient. The void volume inside the porous electrodes allows the deployment of conversion-type, high energy density battery materials such as sulfur and silicon by mitigating volume expansion issues. These porous structures are fabricated based on a scalable and facile hydrogen-templated electrodeposition using a bath that contains a proton source and metal salts [10-11]. In this process, high cathodic current is applied to the Cu substrate, and hydrogen bubbles evolve from the substrate surface from reduction of H^+ ions.

Concurrently, metal structures are co-deposited using hydrogen bubbles as dynamic templates to form a porous metal network. Compared with previous approaches that utilize the hydrogen-templated electrodeposition process [10-11], a mm-scale electrode structure is generated in the current study that enables a substantial improvement in areal capacity. In addition, the process developed allows the porous structure to grow through high energy density Si active material, resulting in an ultrahigh areal capacity of 40 mAh/cm^2. Finally, the utilization issue common with thick electrodes is resolved by introducing hollow channels into electrodes, which is enabled by laser-machining holes onto the Cu substrate before the hydrogen-templated electrodeposition. These channels simultaneously facilitate the charge and mass transport across the thickness of the electrode and allow higher capacity utilization of the porous electrodes.

In the first demonstration of this porous structure, porous Cu is used as a scaffold for the current collector. Cu and Ni are utilized as the secondary metals for the for the anode side and the cathode side, respectively, to cover the loosely connected porous Cu and increase the mechanical rigidity and electrical conduction of the structure. The combination of deposition and stripping cycles are utilized, and uniform coverage of the 2nd metal along mm thick electrodes is achieved, which to the best of the author's knowledge, has not been realized previously. Subsequently, NiSn and S active materials are electro-deposited onto the anode and the cathode scaffolds, respectively. High areal capacity of 10 mAh/cm^2 is achieved on the half-cell level that is superior than most of the electrodes developed so far [1-9], owing to high porosity, z-direction scalability, and highly integrated conductive network of the fabricated electrodes. Furthermore, the S electrode developed in the study

reacts through a different pathway compared to conventional S electrodes, which allows the usage of carbonate-based electrolyte, avoids the polysulfide shuttling issue encountered in most S-based electrodes, and results in about 85% capacity retention in 50 cycles. In addition, a gel electrolyte is synthesized in-situ that can improve the cycling performance of the electrodes. On the full cell level, an areal capacity of 3 mAh/cm^2 has been attained with 2.3 mWh/cm^2 areal power density in the first cycle.

Another demonstration developed in this study involves the direct hydrogen-templated electro-deposition of active material onto a Cu substrate by using Ni and Sn salts and having the porous structure grow through sedimented Si particles. An ultrahigh first cycle capacity of 40 mAh/cm^2 is achieved for this type of electrodes in half-cell tests, which can be attributed to the scalability, porosity of the electrode structure, and high energy density of the battery materials. The cycling performance of the electrode is demonstrated through the utilization of appropriate binder materials. It is found that binders with a higher linear concentration of carboxylic functional groups, such as poly(acrylic acid) (PAA), more closely adheres to the Si particle through hydrogen bonding and results in better capacity retention over cycles. In addition, the deposition condition for the porous composite is crucial, which could potentially enable better infiltration of the binder material into the structure. An ultrathin layer of polymer electrolyte, poly(phenylene oxide) (PPO), is subsequently directly electrodeposited onto the porous composite anode scaffold to provide an ionically conducting yet electrically insulating layer between the anode and the cathode. The cathode slurry is subsequently infiltrated into the porous structure to make the full battery. This approach has the potential advantage to accelerate the manufacturing process

by incorporating all electrode components onto one single piece of device, compared to the previous approach where separate pieces of anode and cathode are required. A non-shorting, proof-of-concept functional full cell is demonstrated.

An electrochemical model for a multi-layer $Ni(OH)_2$ system is developed to help understand how electrode architecture and materials affect the physical processes that limit energy density. The model is initially developed based on and verified with non-porous electrodes, but similar principles can be extended to porous systems. In addition, in order to ensure accuracy of the model, key physical parameters such as diffusion coefficient of the active material are measured. In this study, the diffusion coefficient of NiSn anode active material is measured for the first time as a function of the state of charge using galvanostatic intermittent titration technique (GITT) and electrochemical impedance spectroscopy (EIS). The results are compared with the single average value measured using cyclic voltammetry (CV). The results are in general agreement with each other, which indicated the validity of all measurement techniques. Since it is not always feasible to develop an accurate equivalent circuit model for EIS, GITT with longer resting period provides an alternative to measuring the diffusion coefficient as a function of the state of charge. However, GITT is time-consuming and in cases where an average value would suffice, CV can be utilized instead.

The porous electrodes introduced in this work address several aspects of electrochemical energy storage dynamics that are essential for powering micro-electronic devices. First, the high surface area provided by the porous structure enables a large contact area between

the electrode and electrolyte, resulting in decreased charge transfer resistance and facile reaction kinetics. Second, the porous structure, together with the uniquely designed laser-machined holes on the Cu substrate, facilitates the mass and charge transport throughout the thickness of the electrode. In this way, the capacity utilization of the electrode active material is significantly improved. Specifically, in the current study, the holes on the Cu substrate result in a 90% improvement in areal capacity. Third, the hydrogen-templated electrodeposition method allows good scalability of the electrode in the z-direction that gives rise to high areal capacity. Lastly, the interconnected metal network largely eliminates the ohmic resistance issue encountered in previous studies, which limits the electrode capacity.

6.2. Suggestions for Future Work

Suggestions for future work involves two types of approaches: (1) improvement of the design and fabrication techniques reported in this work and (2) development of new processes

6.2.1. Improvement for S cathodes

In Chapter 3, the capacity of sulfur electrodes lags behind that of the NiSn anode, such that the full cell capacity is limited by the cathode side. Thus, in order to improve the cathode side capacity, deposition of S is investigated at different conditions, and the resulting S cathodes is cycled electrochemically at 2.5 mA/cm^2 versus lithium in 1M $LiPF_6$ in 1:1 EC/DEC with 10% FEC and 1% VC to check their performance. As shown in Figure 6.1 (a), the capacity and cycling performance of the S electrodes are largely impacted by the

deposition conditions. For constant current depositions (CC), the capacity is almost doubled compared to that from the constant voltage depositions. However, the capacity fade is also much more rapid. In addition, the performance varies even for samples under constant voltage conditions. Comparing samples deposited under 0.7V and 0.5V, the 0.7V sample exhibits both better stability and higher capacity. It is interesting to note that the electrodes deposited under 0.7V for 12 hours and 6 hours have almost the same areal capacity. As illustrated in Figure 6.1 (b), the impedance of the S electrode continuously increases with deposition time. It is likely that the capacity beyond 6 hours of deposition cannot be effectively utilized unless a smaller cycling current is used.

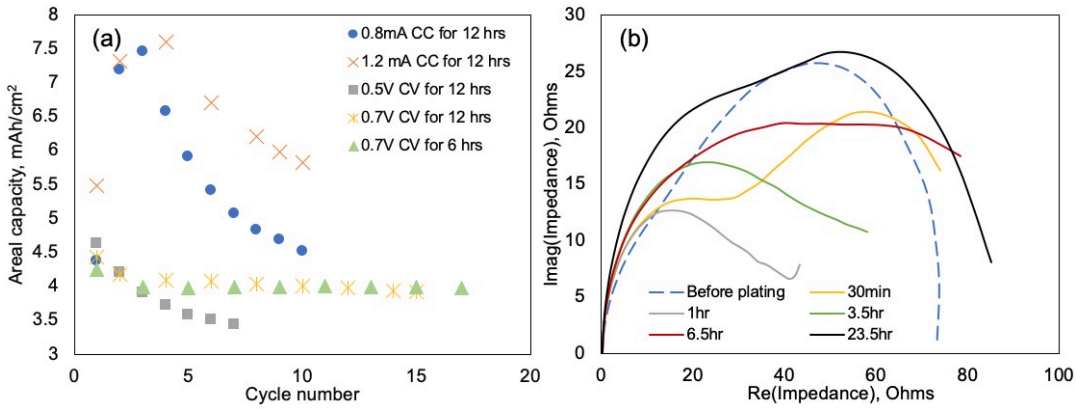

Figure 6. 1**:** (a) Cycling performance S cathodes deposited under different conditions (CC: constant current; CV: constant voltage) (b) Electrochemical impedance spectrum of S cathode during different stages in the deposition process

The cycling instability associated with the galvanostatically deposited samples may stem from the deposition inhomogeneities. As can be seen in Figure 6.2, the resulting S deposition is not uniform across surface of the sample. Better pre-deposition protocols

need to be devised to ensure homogeneous surface reactivities so that certain areas do not get over-plated. The deposition/stripping protocols that result in conformal deposition in the z-direction may also reduce overplating and give rise to better electrochemical performance. Additionally, the deposition conditions could affect the reaction mechanism during S lithiation/delithiation during cycling. Thus, different electrolytes in terms of salts, solvents, and additives may improve electrochemical performance of the S electrodes deposited under varying conditions.

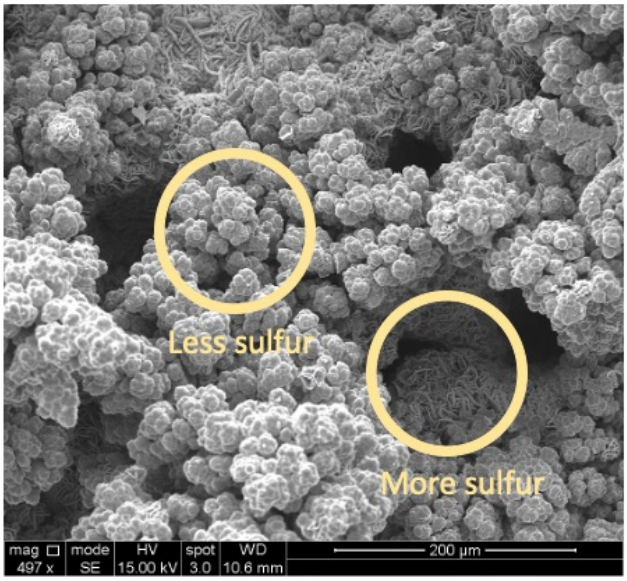

Figure 6. 2**:** SEM image of porous Ni after 0.8 mA constant current S deposition

6.2.2 Full cell cycling

It is determined from Chapter 3 that the loss of lithium inventory is the major culprit for capacity loss during full cell cycling. Thus, strategies need to be devised to reduce the side reaction rates that cause this issue.First, robust passivation interface layers need to

form on the active material surface in a controlled manner before full-cell cycling through reactions with the electrolyte, such that the outermost active material is passivated and does not further react with the electrolyte [12]. This process is vital in the manufacturing of commercial cells and may take as long as 3 – 7 days to ensure good cycling performance. Although the formation process for this interfacial layer is well-established for commercially available electrode materials, there have not been many studies on novel electrode materials, especially for high volume expansion/contraction materials, including S cathodes and NiSn anodes, that may damage the interfacial layer during cycling. Therefore, a systematic study should be conducted to find out the best combination of electrolyte solvent, salt(s), and electrolyte additives that result in the best cycling performance. In addition, the rate of formation also matters. Although electrodes are generally formed at low C rates like C/20, studies have shown that cycling experiments from faster formation protocols at C/5 and C/10 with different voltage cutoffs show better capacity retention compared to those from C/20 [13]. In addition to the electrolyte, C rate, and voltage windows, it is also important to make sure that the porous electrodes are completely wetted before the formation process. Elevating the wetting temperature to 40 – 60 ℃ reduces the liquid electrolyte contact angle and provides access of the electrolyte to the sub-micron-sized pores [12].

In addition to forming a robust solid electrolyte interface in-situ electrochemically, artificial layers may be deposited prior to the formation process. Chemical vapor deposition techniques such as atomic layer deposition (ALD) may be used to deposit an insulating layer like Al_2O_3 that reduces the contact between the electrolyte and the electrode surface

and mitigates the capacity loss due to side reactions. Additionally, ALD coatings may also help prevent the mechanical degradation of high-volume expansion/contraction materials [14].

Since Ni is the inactive component that suppresses the volume expansion of Sn, increasing the Ni ratio in the NiSn active material by changing the deposition bath concentration may alleviate the volume expansion issue. Less volume expansion minimizes the cracking of the active material which in turn reduces the side reactions between the electrode and the electrolyte. However, this would need to be optimized with the loss that would occur in the energy density.

6.2.3 Monolithic cell fabrication

In Chapter 4, PPO deposition on various metal components in the porous NiSn anode is investigated. In order to increase the areal capacity of the electrodes, Si particles are incorporated. Therefore, a better understanding of the PPO growth characteristics on Si surface is required. Due to the semi-conducting nature of Si, electrodeposition on Si surface is not expected to be as facile as that on metal surfaces. However, it has been demonstrated in previous studies that it is possible to grow polymer layers even onto metal oxide surfaces like MnO_2 [15].

A new process is needed to permit better coverage of the 3D electrode surface with PPO. One possibility involves the use of a liquid electrolyte that contains the gelation precursors as described in Chapter 3. Instead of flooding the entire electrode, the volume of the liquid electrolyte precursor is less than the void volume within the porous electrode to allow

infiltration of the cathode slurry in the subsequent processes. It is likely that the porous electrode will be wetted by capillary force, and the electrolyte can spread across the electrode surface via surface diffusion [16]. Then the electrode can be annealed both to evenly distribute the liquid precursor across the surface and to solidify the system in-situ. This whole process may need to be repeated several times until a pin-hole free surface is created to serve as the gel electrolyte. Then, a cathode slurry can be incorporated in the remaining void volume within the electrode to assemble the full cell. This process may avoid the concerns regarding side reactions during high voltage anodic electrodeposition, as described in Chapter 4.

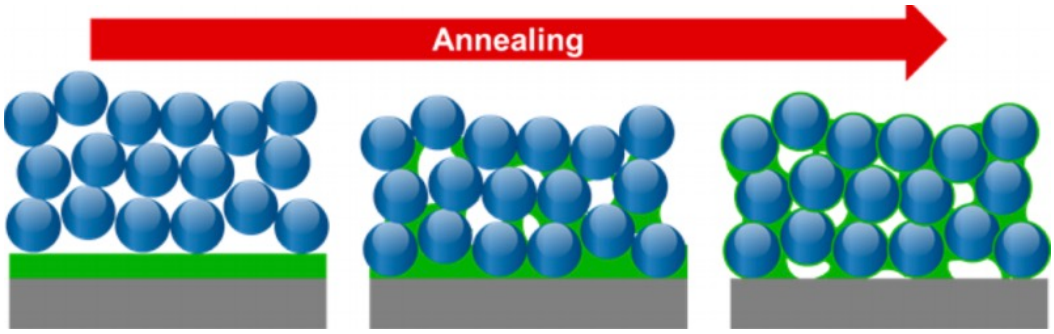

Figure 6. 3**:** Polymer infiltrated porous electrode [16]

For the cathode side, in order to avoid the usage of liquid electrolyte, the binder material should also be ionically conductive. For example, poly(ethylene oxide) (PEO) may serve as both an ionic conductor and a binder material, owing to its good mechanical properties and the high solvation power of the ethylene oxide units [17]. In combination with dispersed metal oxide nanoparticles such as TiO_2 and ZrO_2, PEO can possess meaningful ionic conductivity while effectively suppressing the polysulfide shuttling that is common for Li_2S cathode materials [18-20].

6.2.4. Cycling performance for Si/NiSn composite electrode

Although ultrahigh areal capacity has been achieved for the Si/NiSn composite anodes, their cycling performance still remains unsatisfactory. In order to improve the cycling performance, deposition conditions for the composite electrodes are modified. For example, instead of using 1M H_2SO_4, 2M H_2SO_4 is used in the deposition bath. As shown in Figure 6.4, the cycling performance is improved when 2M H_2SO_4 is used. This improvement may be attributed to the morphology change that results in more void volume to buffer the volume expansion/contraction issue of the Si/NiSn active material. This morphology may also facilitate the infiltration of PAA binder material which better integrates with the active material. Further investigations are needed to verify these hypotheses.

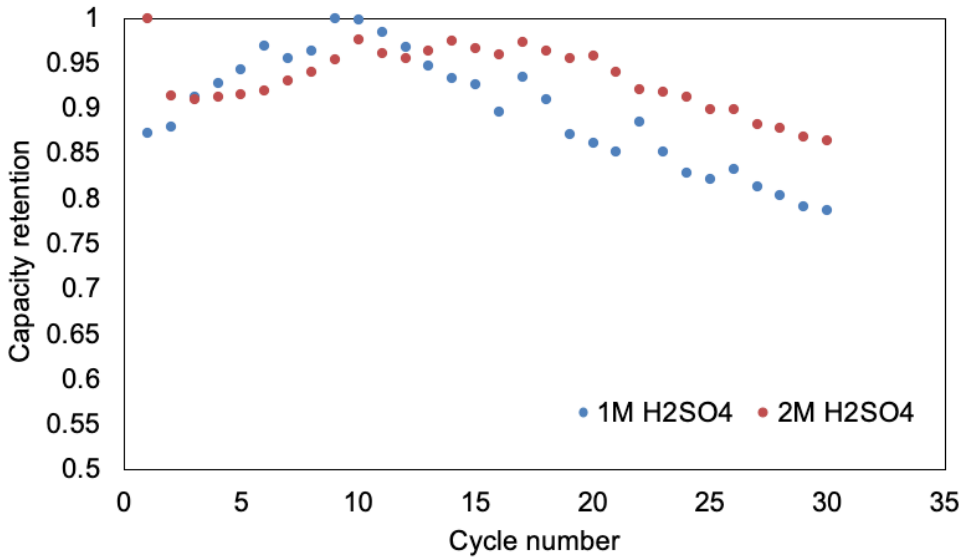

Figure 6. 4**:** Cycling performance comparison for Si/NiSn composite anodes deposited using containing different H_2SO_4 concentrations

6.2.5 Comprehensive modeling of the electrodes

In chapter 5, a mathematical model is developed based on a highly scalable and well-ordered microfabricated 3D $Ni(OH)_2$ electrodes to demonstrate its application to designing electrode architecture and optimizing energy/power density. The underlying mass transport and reaction kinetics principles from the model may also be extended to simulate the performance porous electrodes developed in Chapter 2 – 4. Specifically, the Newman model that are widely used by the battery community for modeling Li-ion based porous electrodes may serve as a good basis [21]. The model can be utilized to study the effect of porosity, tortuosity, and active material thickness on the performance of the electrodes and guide future experimental fabrications. In addition, battery degradation phenomena, such as Li ion inventory consumption through side reactions and active material loss associated with NiSn and S electrodes specific to the current study, which are not considered in the Newman model can be incorporated to better understand the aging mechanisms.

6.3. Reference:

1. Nathan, M., Golodnitsky, D., Yufit, V., Strauss, E., Ripenbein, T., Shechtman, I., ... & Peled, E. (2005). Three-dimensional thin-film Li-ion microbatteries for autonomous MEMS. *Journal of microelectromechanical systems*, *14*(5), 879-885.
2. Kotobuki, M., Suzuki, Y., Munakata, H., Kanamura, K., Sato, Y., Yamamoto, K., & Yoshida, T. (2011). Effect of sol composition on solid electrode/solid electrolyte interface for all-solid-state lithium ion battery. *Electrochimica Acta*, *56*(3), 1023-1029.
3. Hur, J. I., Smith, L. C., & Dunn, B. (2018). High areal energy density 3D lithium-ion microbatteries. *Joule*, *2*(6), 1187-1201.
4. Pearse, A., Schmitt, T., Sahadeo, E., Stewart, D. M., Kozen, A., Gerasopoulos, K., ... & Gregorczyk, K. E. (2018). Three-dimensional solid-state lithium-ion batteries fabricated by conformal vapor-phase chemistry. *ACS nano*, *12*(5), 4286-4294.
5. Talin, A. A., Ruzmetov, D., Kolmakov, A., McKelvey, K., Ware, N., El Gabaly, F., ... & White, H. S. (2016). Fabrication, testing, and simulation of all-solid-state three-dimensional Li-ion batteries. *ACS applied materials & interfaces*, *8*(47), 32385-32391.
6. Sun, K., Wei, T. S., Ahn, B. Y., Seo, J. Y., Dillon, S. J., & Lewis, J. A. (2013). 3D printing of interdigitated Li-Ion microbattery architectures. *Advanced materials*, *25*(33), 4539-4543.
7. Ergang, N. S., Fierke, M. A., Wang, Z., Smyrl, W. H., & Stein, A. (2007). Fabrication of a fully infiltrated three-dimensional solid-state interpenetrating electrochemical cell. *Journal of the Electrochemical Society*, *154*(12), A1135-1147.
8. Rhodes, C. P., Long, J. W., Pettigrew, K. A., Stroud, R. M., & Rolison, D. R. (2011). Architectural integration of the components necessary for electrical energy storage on the nanoscale and in 3D. *Nanoscale*, *3*(4), 1731-1740.
9. Werner, J. G., Rodríguez-Calero, G. G., Abruña, H. D., & Wiesner, U. (2018). Block copolymer derived 3-D interpenetrating multifunctional gyroidal nanohybrids for electrical energy storage. *Energy & Environmental Science*, *11*(5), 1261-1270.
10. Shin, H. C., Dong, J., & Liu, M. (2003). Nanoporous structures prepared by an electrochemical deposition process. *Advanced Materials*, *15*(19), 1610-1614.

11. Shin, H. C., & Liu, M. (2004). Copper foam structures with highly porous nanostructured walls. *Chemistry of materials*, *16*(25), 5460-5464.
12. Wood III, D. L., Li, J., & An, S. J. (2019). Formation challenges of lithium-ion battery manufacturing. *Joule*, *3*(12), 2884-2888.
13. An, S. J., Li, J., Du, Z., Daniel, C., & Wood III, D. L. (2017). Fast formation cycling for lithium ion batteries. *Journal of Power Sources*, *342*, 846-852.
14. Xiao, X., Lu, P., & Ahn, D. (2011). Ultrathin multifunctional oxide coatings for lithium ion batteries. *Advanced Materials*, *23*(34), 3911-3915.
15. Rhodes, C. P., Long, J. W., Pettigrew, K. A., Stroud, R. M., & Rolison, D. R. (2011). Architectural integration of the components necessary for electrical energy storage on the nanoscale and in 3D. *Nanoscale*, *3*(4), 1731-1740.
16. Hor, J. L., Jiang, Y., Ring, D. J., Riggleman, R. A., Turner, K. T., & Lee, D. (2017). Nanoporous polymer-infiltrated nanoparticle films with uniform or graded porosity via undersaturated capillary rise infiltration. *ACS nano*, *11*(3), 3229-3236.
17. Armand, M. (1994). The history of polymer electrolytes. *Solid State Ionics*, *69*(3-4), 309-319.
18. Lee, F., Tsai, M. C., Lin, M. H., Ni'mah, Y. L., Hy, S., Kuo, C. Y., ... & Hwang, B. J. (2017). Capacity retention of lithium sulfur batteries enhanced with nano-sized TiO 2-embedded polyethylene oxide. *Journal of Materials Chemistry A*, *5*(14), 6708-6715.
19. Hassoun, J., & Scrosati, B. (2010). Moving to a solid-state configuration: a valid approach to making lithium-sulfur batteries viable for practical applications. *Advanced Materials*, *22*(45), 5198-5201.
20. Shin, J. H., Kim, K. W., Ahn, H. J., & Ahn, J. H. (2002). Electrochemical properties and interfacial stability of (PEO) 10LiCF3SO3–TinO2n− 1 composite polymer electrolytes for lithium/sulfur battery. *Materials Science and Engineering: B*, *95*(2), 148-156.
21. Newman, J., & Thomas-Alyea, K. E. (2012). *Electrochemical systems*. New York: John Wiley & Sons.